UNIVERSITY OF CALIFORNIA SAN DIEGO

Bridging cognition and neurobiology with large-scale cortical dynamics and multimodal brain data

A dissertation submitted in partial satisfaction of the
requirements for the degree
Doctor of Philosophy

in

Cognitive Science

by

Richard Gao

Committee in charge:

Professor Bradley Voytek, Chair
Professor Andrea Chiba
Professor Eran Mukamel
Professor Alysson Muotri
Professor Brad Werner

2020

The dissertation of Richard Gao is approved, and it is acceptable in quality and form for publication on microfilm and electronically:

Chair

University of California San Diego

2020

DEDICATION

To Mom, Dad, and Grandma—without you, none of this would be possible.

EPIGRAPH

To see a World in a Grain of Sand

And a Heaven in a Wild Flower

Hold Infinity in the palm of your hand

And Eternity in an hour.

—William Blake

All science is the search for unity in hidden likenesses.

—Jacob Bronowski

The brain is a stadium.

—Arturs Semenuks

TABLE OF CONTENTS

LIST OF FIGURES

LIST OF TABLES

ACKNOWLEDGEMENTS

Over the last 6 years, I've had incredible luck in forging many relationships, new and old, with people who have helped me in science and in life, through the good and bad. This PhD would not have been possible, and definitely not as fun, if not for the people along the way.

First and foremost, I am extremely grateful for my advisor, Bradley Voytek: thank you for your mentorship, advice, and most importantly, your trust. You've never hovered over my shoulders, but you were always an email or Slack message away when I needed to talk. I am eternally thankful for this, because it challenged me to develop my own thoughts and ideas, to take ownership of them, and to prioritize for myself, even though it was often scary and that I wished my boss would just tell me what to do. I'm grateful for all the resources and opportunities you've provided for me to talk about my work, paying me over the summer, and sending me to conferences and summer schools, even back when the lab was basically broke. I truly felt that my advisor was a mentor who prioritized his mentees, who had my best interest at every turn, and you supported what I did even if you disagreed with how I did them. It was my good fortune to stumble into your lab as it began. I learned from you about how to be a kind human even more than how to be a good scientist, and I think you would prefer it to be that way as well.

Speaking of the lab, it's been very special to be able to share the journey with you all, especially in our early days. My labmates since day 1—Scott Cole, Tom Donoghue, and Tammy Tran: thank you for being fantastic friends and colleagues. You have influenced my work, my thinking, and who I am as a person for the better, and I will always think fondly of our random discussions over afternoon coffee, the ugly lab furniture, ignite talks, Cinco Dynamico, and Taylor Swift songs in Chicago. We did it! Erik Peterson, Roemer van der Meij, Torben Noto: thank you guys for setting the tone for the lab, for teaching me to have wild ideas, to be curious, and for making science less serious in the best ways possible while maintaining a high standard for our work. I am also grateful for Leo Waschke, Sydney Smith, Tunmise Olayinka, and Natalie Schaworonkow, for engaging with me in science and in life, and for pushing me to be better, especially through the final stretch of my PhD. I'd also like to thank the students whom I've had the privilege to work with: Lauren Liao, Stan Liu, Dylan Christiano, Adrianna Hohil, Lucas Henry, Christopher Caligiuri, and Brian Barry. It was fun to work with such a driven and intelligent group of young people, and I learned a lot from you about mentorship and science.

I am grateful for the support of my own mentors at UCSD: Alysson Muotri, thank you for treating me like your own student throughout our collaboration and for constantly inspiring me to think "why not?" Eran Mukamel, thank you for challenging me to think more deeply, beyond the superficial things and appreciating that the devil's in the details, as well as all your help when I taught COGS118C. Andrea Chiba, I am grateful for your incredible generosity with your time anytime I passed by your lab unannounced or in the parking lot, and similarly, for challenging me to do better in the kindest way possible. bt (Brad Werner), thank you for your unique perspectives, which imprinted on me the difficulties of understanding truly complex systems like the brain, and even more so, science as it is in our institutions and society. Finally, I'd like to thank Marta Kutas, Doug Nitz, and Rafael Núñez, who made me feel welcomed and cared for as a person in the department. You inspired and made me believe that, perhaps, I did end up becoming a cognitive scientist—and if so, I am proud to be one.

Over these 6 years, I've had the opportunity to work with, learn from, and share memories (and drinks) with a group of amazing peers from the myriad corners of the cognitive science hexagon. Through their own unique and passionate pursuits in understanding cognition, they have fundamentally changed the way I think about the brain and cognition as well, especially when taking into consideration complex human behaviors, language, and culture. In particular, I'd like to thank my PhD cohort (the greatest of all time)—Rachel Bristol, Carson Grant Miller Rigoli, Eric Leonardis, Tom Donoghue (again), Amanda Song—and especially my now roommates: Michael Allen, Arturs Semenuks, Joey Relaford-Doyle, and Adam Mekrut (in spirit), for not only being excellent scholars, educators, and starchitects in their own right, but for also being patient, respectful, and curious about one another's work and life. Thank you for your support—I'm going to miss our little family (last sentence on page 1 is dedicated to you), and I couldn't have done it without you :). Also, shoutout to Uncle Weasel and the Strenf, may our legends live on through the future Earth Pigs.

I am grateful for the opportunity to be a member of the scientific community, both here at UCSD and across the world. I'd like to thank all the collaborators: Jerome Karpiak, Pri Negraes, Cleber Trujillo, Jason Adams, the rest of the Muotri lab, as well as Thomas Pfeffer and Rudy van den Brink. The works included in this dissertation would not have been the same without your contributions. It's been a pleasure to work closely with you all and to become friends over the course of our collaborations. I am also grateful for the UCSD Writing Hub Graduate Consultant team and Engaged Teaching Center for making me a more well-rounded scientist, by providing me with invaluable training in writing and teaching in a professional capacity. More broadly, I would have never imagined that doing a PhD would let me meet people from all over the world: at summer schools (Redwood 2015, Cajal Computational Neuroscience 2019, and NMA 2020), conferences, and on Twitter. I am thankful for all the friends I've made through them, especially those of you who came to show your support at my defense, and those of you who I've had the good fortune of visiting abroad. Critically, this dissertation would not have been possible without the open science community—the people that share their code and data, as well as the infrastructures which enable that (MNI, CRCNS, Neurotycho, Allen Brain Institute, and Human Connectome Project)—and the generous funding from the Katzin family, UCSD FISP and Kavli Institute for Brain and Mind, and especially the Government of Canada and NSERC.

Science, at the end of the day, is still just a part of life, no matter how big, so I am thankful for everyone back home: the derpsquad, Beverley gang, and all y'all that came out to visit me in California or provided a place for me to crash (sometimes over quite a few days). Zimu, Kelvin, David, KLam, J$, Matt, DP, Kobe, Mei, and many, many others: thank you for loving and caring for me through the ups and downs of life, and especially through some very trying times in the last couple of years. Knowing that I can come home to a gang who loves me regardless of whether

I’m good at my job as a scientist makes life a lot easier.

Finally, mom, dad, and grandma: this is dedicated to you. Without you, I would simply not be here today. Thank you for your endless love, support, and inspiration.

Co-author acknowledgements:

Chapter 1, in full, is a reprint of the material as it appears in the following manuscript published in *Cell Stem Cell*: Trujillo*, C. A., Gao*, R., Negraes*, P. D., Gu, J., Buchanan, J., Preissl, S., Wang, A., Wu, W., Haddad, G. G., Chaim, I. A., Domissy, A., Vandenberghe, M., Devor, A., Yeo, G. W., Voytek, B., & Muotri, A. R. (2019). **Complex oscillatory waves emerging from cortical organoids model early human brain network development.** The dissertation author was one of the primary investigators and co-first authors of this paper.

Chapter 2, in full, is a reprint of the material as it appears in the following manuscript published in *NeuroImage*: Gao, R., Peterson, E. J., & Voytek, B. (2017). **Inferring synaptic excitation/inhibition balance from field potentials.** The dissertation author was the primary investigator and author of this paper.

Chapter 3, in full, is a reprint of the material as it appears in the following manuscript published in *eLife*: Gao, R., van den Brink, R. L., Pfeffer, T., & Voytek, B. (2020). **Neuronal timescales are functionally dynamic and shaped by cortical microarchitecture.** The dissertation author was the primary investigator and author of this paper.

VITA

2014	Bachelors of Applied Science in Engineering Science, University of Toronto, Toronto
2014 - 2019	Teaching Assistant, Dept. of Cognitive Science, University of California San Diego
2019	Instructor on Record: COGS118C—Neural Signal Processing (2019S1), Dept. of Cognitive Science, University of California San Diego
2020	Doctor of Philosophy in Cognitive Science, University of California San Diego

PUBLICATIONS

Gao, R., van den Brink, R. L., Pfeffer, T., & Voytek, B. (2020). Neuronal timescales are functionally dynamic and shaped by cortical microarchitecture. *eLife*, 9, e61277.

Donoghue, T., Haller, M., Peterson, E. J., Varma, P., Sebastian, P., **Gao, R.**, Noto, T., Lara, A. H., Wallis, J. D., Knight, R. T., Shestyuk, A., & Voytek, B. (2020). Parameterizing neural power spectra into periodic and aperiodic components. *Nature Neuroscience*, 23(12), 1655–1665.

Ghatak, S., Dolatabadi, N., **Gao, R.** et al. (2020). NitroSynapsin ameliorates hypersynchronous neural network activity in Alzheimer hiPSC models. *Mol Psychiatry*.

Trujillo, C. A.*, **Gao, R.***, Negraes, P. D.*, et al. (2019). Complex oscillatory waves emerging from cortical organoids model early human brain network development. *Cell Stem Cell*, 25(4) 558-69.

Cole, S, Donoghue, T., **Gao, R.**, Voytek, B. (2019). NeuroDSP: A package for neural digital signal processing. *Journal of Open Source Software*, 4(36), 1272.

Núñez, R., Allen, M., **Gao, R.**, Rigoli, C.M., Relaford-Doyle, J., Semenuks, A. (2019). What happened to cognitive science. *Nature Human Behavior*, 3(8), 782-91.

Moore, S. M., Seidman, J. S., Ellegood, J., **Gao, R.**, Savchenko, A., Troutman, T. D., et al. (2019). Setd5 haploinsufficiency alters neuronal network connectivity and leads to autistic-like behaviors in mice. *Translational Psychiatry*, 9(1), 24.

Gao, R., Peterson, E. J. & Voytek, B. (2017). Inferring synaptic excitation/inhibition balance from field potentials. *Neuroimage* 158, 70–78.

Gao, R. (2016). Interpreting the electrophysiological power spectrum. *Journal of Neurophysiology* 115, 628–630.

ABSTRACT OF THE DISSERTATION

Bridging cognition and neurobiology with large-scale cortical dynamics and multimodal brain data

by

Richard Gao

Doctor of Philosophy in Cognitive Science

University of California San Diego, 2020

Professor Bradley Voytek, Chair

Human cognition depends on complex and coordinated activity of neural populations, which are enabled by a rich diversity in cellular and network properties across the brain. To study the neural basis of cognition, cognitive neuroscience combines the analysis of large-scale electrophysiological signals—neural field potentials with contributions from millions of neurons—with behavioral tasks to observe brain dynamics during cognitive processes, such as attention, decision-making, and language understanding. This approach has been successful in discovering neural correlates of cognition, which can differentiate between behavioral states and tracking disease progression within and across individuals. However, we currently lack the

ability to analyze the physiological contributions underlying these brain signals, especially in humans, thus hindering advances towards a mechanistic understanding of how cognition is linked to neurobiology, as well as how cognitive functions deteriorate with pathological changes in the brain.

In this dissertation, I leverage multimodal brain data from humans, animals, and in-vitro models, as well as novel simulation and analysis techniques to investigate the biological variables underlying oscillatory and asynchronous neural dynamics, ultimately relating them to cognition. **Chapter 1** reports the emergence of complex oscillatory activity in human induced pluripotent stem cell-derived brain organoids, a model for early neurodevelopment, and the co-evolution of the cellular and synaptic properties that support it. **Chapter 2** presents a computational model that accounts for changes in the 1/f power law exponent of asynchronous (or scale-free) neural activity as a shift in the balance between synaptic excitation and inhibition, which is validated on rodent and non-human primate electrophysiological data. **Chapter 3** develops a novel computational technique to infer neuronal timescales across the human cortex, which follows a gradient along the sensorimotor-to-association cortical hierarchy, is shaped by variations in inhibitory synaptic and transmembrane ion channel proteins, and dynamically lengthens during working memory maintenance and shortens over aging in the long term. Together, these works present a framework for integrating open-source datasets and existing findings from cellular, systems, and cognitive neuroscience to decipher large-scale human brain recordings, thus linking brain structure and function with neural dynamics for mechanistic investigations of cognition and brain disorders.

Chapter 0

Introduction

A case for the human model of cognition

Modern neuroscience has granted us the ability to conduct detailed investigations into the neural basis of cognition in many model organisms, in an effort to understand the role the brain plays in shaping our own thoughts and actions. Linking knowledge of biological mechanisms we learned from animal brains to principles of human cognition, however, presents many challenges that relate to the theoretical, technical, and ethical limitations surrounding the study of human brains and behavior. Human cognition is complex, embodied, and situated in our environments and cultures (Hutchins, 1995; Rosch et al., 1992), and so is the cognition of rodents, apes, dolphins, and potentially robots endowed with artificial intelligence. They are not inherently better or worse than one another, but different. "Rats are not small humans" is a common criticism towards the use of rodent models in neuroscience, but it is not a pejorative—depending on which aspect of cognition one is interested in, rats may in fact be superior than humans: spatial navigation guided by odors in the dark subway tunnels of New York City is natural for a rodent, and walking above ground and finding your way using Google Maps is natural for humans of today. We intuitively understand that they are similar in some ways, but not in all ways: much of the differences arise from the brains, sensorimotor capabilities, and environmental affordances we and our rodent friends are endowed with, and the key similarities (fortunately for neuroscientists) reside in the fact that we can both get from point A to point B guided by our senses, memories, and goals, and that we both have a hippocampus.

Indeed, the discoveries of place cells and grid cells in the hippocampal and entorhinal system (Moser et al., 2008)—the neural mechanisms underlying rodent spatial navigation—were awarded the Nobel prize recently. Rightfully so, for their insights into the so-called "cognitive maps", but not because we desperately want to solve how rats find their way into our homes, rather that we believe cognitive maps are a part of the same principles underlying human navigation through physical space, time, and even mental concepts (Behrens et al., 2018; Stachenfeld et al., 2017). Because of our ability to invasively perturb and measure their brains and behaviors, animal models are indispensable for the progress of cognitive neuroscience, where we can look at the neural mechanisms underlying many animal behaviors that could represent a simplified version, a precondition, or a subset of the computations performed for human cognition (Cisek, 2019).

Nevertheless, although animals exhibit complex behaviors that are fascinating independent of how they could potentially model human cognition, chickens counting (Rugani et al., 2015) is not exactly humans counting (Núñez, 2017), songbirds vocalizing is not exactly humans arguing or singing opera (Hockett, 1960; Townsend et al., 2018; Engesser & Townsend, 2019), tool-use in apes is not exactly humans offloading working memory demands onto our smartphones (Seed & Byrne, 2010), and rats are not exactly small humans. Here, the differences are as interesting as the similarities, which can be just as well said about human cognition across cultures (Barrett, 2020; Bender, 2019). And while these animal models shed light on how neural circuits could implement parts of the analogous computations, they provide only preliminary clues to the neural basis of human cognition, not the full solution (if that's what one is interested in). Thus, these clues give us a valuable starting point for where and how to probe the human brain for follow-up investigations, but it is crucial to integrate the insights gained from animals, as well as in-vitro and computational models of the brain, to understand how similar molecular, synaptic, cellular, and network mechanisms support similar functions in the human brain, and where the similarities eventually breakdown. However, to pursue an investigation of the biological basis of human cognition, we are immediately faced with a difficult challenge: due to technical limitations and ethical considerations, we cannot directly perturb and record from the human brain with the resolution and level of control we desire—not now, and potentially not ever.

Cognitive neuroscience and neural correlates of cognition

One of the central questions in neuroscience asks how the human nervous system gives rise to intelligent and adaptive behaviors, and how cognitive functions deteriorate in conjunction with pathological changes in the brain. The field of cognitive neuroscience—combining neuroimaging, cognitive science, psychology, and clinical neuroscience—has been at the forefront of this research investigating complex human cognition. This is especially true in the last two decades, with the advent of non-invasive high spatial and temporal resolution neuroimaging tools such as functional magnetic resonance imaging (fMRI) and high-density magneto-/electroencephalogram (M/EEG), and more recently, electrocorticography (ECoG) and local field potentials (LFP) from focal invasive cortical recordings in patients undergoing neurosurgical monitoring. Aside from rare clinical circumstances where limited recordings from single neurons are accessible, most human brain signals come in the form of aggregate neural field potential (e.g., EEG, ECoG and LFP), which do not directly reflect neuronal action potentials, but the complex interaction and integration of ionic currents from millions of neurons across different neural circuits, and potentially over different brain regions (Buzsáki et al., 2012) (or, in the case of fMRI, neurovascularly coupled blood oxygenation). Nevertheless, combined with complex behavioral task paradigms, these tools give us the ability to observe the human brain during various cognitive processes, such as attention, working memory, decision-making, and language understanding—many of which are uniquely human—over multiple timescales.

This line of research has produced a large repertoire of neural correlates (or biomarkers) that reflect changes in behavior over the last few decades. However, these studies are often phenomenological, treating the brain as a “computational blackbox”. That is, neural correlates of cognition inform computational theories of the mind and consistently reflect changes in cognitive state or disease progression both within and across people, but do not advance a mechanistic understanding of the biological details that underlie neural population dynamics and computation. An example of such a biomarker is rhythmic neural activity, or “neural oscillations”: 10 Hz fluctuations in scalp EEG were first recorded using a simple voltmeter over a hundred years ago (coined alpha oscillations). Since then, it has been found to correlate with a wide range of cognitive and disease states, such as perceptual awareness, arousal, aging, and autism, to name just a few. However, to this day, we still have an incomplete picture of how alpha oscillations are generated in the human brain (Halgren et al., 2019), the precise cell-types, neuronal microcircuits, and brain regions that are involved, and why it is so intimately linked to many aspects of cognition.

The lack of mechanistic understanding of alpha oscillations is not the exception, but the norm for neural correlates in cognitive neuroscience. With more spatiotemporally resolved electrical recordings, we have now observed many types of oscillations—beta, theta, gamma, sleep spindles, etc.—that correlate with various behaviors. Furthermore, oscillations represent only a subset of signal features that can be extracted from these meso- and macroscale electrophysiological signals. Others range from simple measures like stimulus-locked signal deflections (event-related potential, ERP (Kutas & Hillyard, 1980)), to complex and nonlinear measures such as signal entropy and fractal exponent (Waschke et al., 2019). Finally, when taking into consideration other signal modalities, such as functional connectivity measures in fMRI, it’s clear that cognitive neuroscience now has an abundance of neural biomarkers that can predict task performance and discriminate between cognitive states, especially when combined with modern machine learning techniques. Although signal features (like neural oscillations) can motivate theories for how large-scale network dynamics can support cognition (Fries, 2005; Voytek & Knight, 2015; Breakspear, 2017), these analyses do not provide a mechanistic understanding of the link between cognition and the brain at a more detailed biological level, which would greatly benefit targeted clinical interventions for neurological and psychiatric disorders, as well as provide fundamental insight into the biological wetware that endows us with general intelligence beyond what's possible with artificial intelligence today.

Cognitive neuroscience does not by definition preclude mechanistic links to biological details. In fact, we are very interested in understanding, for example, "the circuit dynamics, network architectures, neuronal biophysics, synaptic rules, and molecular pathways that make cognition possible." Quoted is the mission statement of the Mechanistic Cognitive Neuroscience Unit at HHMI Janelia Research campus in the U.S. While many such systems neuroscience research programs from different labs across the world share this goal, most of them share another similarity: that these investigations are often conducted in model organisms with very different (and limited) cognitive and behavioral repertoires, like C. elegans, drosophila, zebrafish, and rodents. Indeed, while the unifying goal is clear, in practice, investigations of biological mechanisms and complex cognition—especially human cognition—occur in largely disparate fields. Cellular and systems neuroscience depend on the tools of proteomics, synaptic imaging, intracellular recordings, and genetic manipulations to precisely characterize the biological machineries that shape the diversity of form and function of cells in small networks, while cognitive neuroscience uses macroscale imaging modalities to probe neural correlates of complex cognition, with little overlap in between. This is due in large part to the technical and ethical limitations surrounding invasively recording large populations of single neurons, as well as their dendritic and molecular processes from the human brain. Therefore, a persisting challenge remains for neuroscience: can we integrate our detailed knowledge of smaller scale biological systems to understand how heterogeneous components across spatial scales—ion channels, synapses, neurons, circuits—mechanistically combine to shape neural dynamics, and in turn give rise to complex computation and cognition in humans?

Bridging biology and cognition with large-scale neural dynamics

In this dissertation, I propose that meso- and macroscale brain dynamics can be used to link neurobiology with human cognition. On one side, a large body of work from computational and systems neuroscience is dissecting the physiological mechanisms that enable neural population dynamics in animal models, typically measured in the form of spiking activity from many isolated single neurons, but in some cases, local field potentials as well. On the other side, we have an ever-increasing repertoire of EEG, ECoG, and LFP signal features—both manually engineered and machine-learned—that correlate with aspects of human behavior, cognition, and disease, but for which we do not understand the physiological mechanisms. Therefore, one productive line of research is to hone in on a narrower gap: drawing on data and findings from cellular, systems, and cognitive neuroscience and integrating them using computational simulation and analysis frameworks, we can combine the ingredients on the two ends of this spectrum to decipher large-scale neural signals in terms of their underlying biological processes. In other words, if we can make even partial inferences on smaller scale variables, such as spike train statistics or synaptic weights, using signals accessible from the human brain, it would enable a broad range of mechanistic investigations into human cognition and brain disorders.

This dissertation is by no means the first attempt at such a research program, and it is made possible by building on advances across many subfields of neuroscience. For example, earlier works in cognitive neurodynamics explicitly attempt to explain large-scale brain signals detectable in humans in terms of their biological mechanisms, while arguing that those signals may be at a more relevant scale than single-neuron spiking when considering the neural computations required for complex behavior (Freeman, 2000; Varela et al., 2001). More recent works have similarly recognized the utility of meso- and macroscale brain signals, such as LFP and ECoG, as a way to decode neural population activity, as well as biophysical contributions from synaptic and other transmembrane currents (Buzsáki et al., 2012; Einevoll et al., 2013; Panzeri et al., 2015; Pesaran et al., 2018; Sherman et al., 2016). There is also a long history of experimental (Buzsáki

& Draguhn, 2004; Buzsáki & Freeman, 2015) and computational research (Brunel & Wang, 2003; Kopell et al., 2000; Wang, 2010) specifically on neural oscillations in the animal literature, which have inspired analogous investigations in non-human primates and humans, such as gamma oscillations in sensory cortices (Bartoli et al., 2019; Hermes et al., 2015; Ray et al., 2008; Ray & Maunsell, 2011), as well as theta oscillations as they relate to the aforementioned place cells in the hippocampus (Buzsáki, 2002; Maidenbaum et al., 2018). Recent works investigating the non-rhythmic (or aperiodic, scale-free (He et al., 2010)) components of neural field potentials have also enabled novel opportunities for linking human cognition with lower-level physiology, such as the relationship between high-frequency (high-gamma, or broadband) activity with local neural population firing rate (Crone et al., 1998; Manning et al., 2009; Mukamel et al., 2005). Finally, it must be mentioned that computational frameworks that build models of neural circuits using empirical findings from animals are integral for making the link across levels (Einevoll et al., 2019), since the simulated model output can then be compared with real brain data from humans for inference of variables that are otherwise inaccessible, such as macroconnectivity structure (Kiebel et al., 2008) and more fine-grained cellular and synaptic properties (Gonçalves et al., 2020).

The above references represent an overview, and only a small subset of the works that this dissertation is directly built upon or is otherwise inspired by (more relevant references are found within the Chapters). The current work can be viewed as following the same philosophy while using more modern simulation and analysis frameworks (Cole et al., 2019; Donoghue et al., 2020), in conjunction with rich multimodal brain data, such as gene expression, brain imaging, and human electrophysiological data that were made possible owing to efforts from multi-site consortia and open-source collaborations (Frauscher et al., 2018; Hawrylycz et al., 2012; Jacobs & Kahana, 2010; Van Essen et al., 2013; Voytek, 2016, 2017).

Outline of dissertation

The dissertation is organized as follows: Chapter 1 uses a novel model of early neurodevelopment—human induced pluripotent stem cell-derived brain organoids—to investigate the origin of cortical oscillations, then compare those oscillations to features derived from premature infant EEG (Trujillo et al., 2019). Chapter 2 combines computational simulation and data from rodents and non-human primates to infer the ratio of local excitation and inhibition—two fundamental and balancing forces in the brain—from power law properties of LFP and ECoG power spectral density (Gao et al., 2017). Finally, Chapter 3 develops a novel method to infer neuronal timescales, a quantity that characterizes the ability to track rapidly changing sensory cues vs. slowly accumulating contextual information, and dissect the contributions from synaptic, cellular, and network properties across the cortex that shape these timescales, as well as how they change in behavior and aging (Gao et al., 2020).

Bibliography

Barrett, H. C. (2020). Towards a cognitive science of the human: Cross-Cultural approaches and their urgency. Trends Cogn. Sci., 24, 620–638.

Bartoli, E., Bosking, W., Chen, Y., Li, Y., Sheth, S. A., Beauchamp, M. S., Yoshor, D., & Foster, B. L. (2019). Functionally distinct gamma range activity revealed by stimulus tuning in human visual cortex. Curr. Biol., 29, 3345–3358.e7.

Behrens, T. E. J., Muller, T. H., Whittington, J. C. R., Mark, S., Baram, A. B., Stachenfeld, K. L., & Kurth-Nelson, Z. (2018). What is a cognitive map? organizing knowledge for flexible behavior. Neuron, 100, 490–509.

Bender, A. (2019). The role of culture and evolution for human cognition. Top. Cogn. Sci.

Breakspear, M. (2017). Dynamic models of large-scale brain activity. Nat. Neurosci., 20, 340–352.

Brunel, N. & Wang, X.-J. (2003). What determines the frequency of fast network oscillations with irregular neural discharges? i. synaptic dynamics and excitation-inhibition balance. J. Neurophysiol., 90, 415–430.

Buzsáki, G. (2002). Theta oscillations in the hippocampus. Neuron, 33, 325–340.

Buzsáki, G., Anastassiou, C. A., & Koch, C. (2012). The origin of extracellular fields and currents–EEG, ECoG, LFP and spikes. Nat. Rev. Neurosci., 13, 407–420.

Buzsáki, G. & Draguhn, A. (2004). Neuronal oscillations in cortical networks. Science, 304, 1926–1929.

Buzsáki, G. & Freeman, W. (2015). Editorial overview: brain rhythms and dynamic coordination. Curr. Opin. Neurobiol., 31, v–ix.

Cisek, P. (2019). Resynthesizing behavior through phylogenetic refinement. Atten. Percept. Psychophys., 81, 2265–2287.

Cole, S., Donoghue, T., Gao, R., & Voytek, B. (2019). NeuroDSP: a package for neural digital signal processing. Journal of Open Source.

Crone, N. E., Miglioretti, D. L., Gordon, B., & Lesser, R. P. (1998). Functional mapping of human sensorimotor cortex with electrocorticographic spectral analysis. II. event-related synchronization in the gamma band. Brain, 121 (Pt 12), 2301–2315.

Donoghue, T., Haller, M., Peterson, E. J., Varma, P., Sebastian, P., Gao, R., Noto, T., Lara, A. H., Wallis, J. D., Knight, R. T., Shestyuk, A., & Voytek, B. (2020). Parameterizing neural power spectra into periodic and aperiodic components. Nat. Neurosci., 23, 1655–1665.

Einevoll, G. T., Destexhe, A., Diesmann, M., Grün, S., Jirsa, V., de Kamps, M., Migliore, M., Ness, T. V., Plesser, H. E., & Schürmann, F. (2019). The scientific case for brain simulations. Neuron, 102, 735–744.

Einevoll, G. T., Kayser, C., Logothetis, N. K., & Panzeri, S. (2013). Modelling and analysis of local field potentials for studying the function of cortical circuits. Nat. Rev. Neurosci., 14, 770–785.

Engesser, S. & Townsend, S. W. (2019). Combinatoriality in the vocal systems of nonhuman animals. Wiley Interdiscip. Rev. Cogn. Sci., 10, e1493.

Frauscher, B., von Ellenrieder, N., Zelmann, R., Doležalová, I., Minotti, L., Olivier, A., Hall, J., Hoffmann, D., Nguyen, D. K., Kahane, P., Dubeau, F., & Gotman, J. (2018). Atlas of the normal intracranial electroencephalogram: neurophysiological awake activity in different cortical areas. Brain, 141, 1130–1144.

Freeman, W. J. (2000). Mesoscopic neurodynamics: from neuron to brain. J. Physiol. Paris, 94, 303–322.

Fries, P. (2005). A mechanism for cognitive dynamics: neuronal communication through neuronal coherence. Trends Cogn. Sci., 9, 474–480.

Gao, R., Peterson, E. J., & Voytek, B. (2017). Inferring synaptic excitation/inhibition balance from field potentials. Neuroimage, 158, 70–78.

Gao, R., van den Brink, R. L., Pfeffer, T., & Voytek, B. (2020). Neuronal timescales are functionally dynamic and shaped by cortical microarchitecture. Elife, 9, e61277.

Gonçalves, P. J., Lueckmann, J.-M., Deistler, M., Nonnenmacher, M., Öcal, K., Bassetto, G., Chintaluri, C., Podlaski, W. F., Haddad, S. A., Vogels, T., Greenberg, D. S., & Macke, J. H. (2020). Training deep neural density estimators to identify mechanistic models of neural dynamics. Elife, 9.

Halgren, M., Ulbert, I., Bastuji, H., Fabó, D., Erőss, L., Rey, M., Devinsky, O., Doyle, W. K., Mak-McCully, R., Halgren, E., Wittner, L., Chauvel, P., Heit, G., Eskandar, E., Mandell, A., & Cash, S. S. (2019). The generation and propagation of the human alpha rhythm. Proc. Natl. Acad. Sci. U. S. A., 116, 23772–23782.

Hawrylycz, M. J., Lein, E. S., Guillozet-Bongaarts, A. L., Shen, E. H., Ng, L., Miller, J. A., van de Lagemaat, L. N., Smith, K. A., Ebbert, A., Riley, Z. L., Abajian, C., Beckmann, C. F., Bernard, A., Bertagnolli, D., Boe, A. F., Cartagena, P. M., Chakravarty, M. M., Chapin, M., Chong, J., Dalley, R. A., David Daly, B., Dang, C., Datta, S., Dee, N., Dolbeare, T. A., Faber, V., Feng, D., Fowler, D. R., Goldy, J., Gregor, B. W., Haradon, Z., Haynor, D. R., Hohmann, J. G., Horvath, S., Howard, R. E., Jeromin, A., Jochim, J. M., Kinnunen, M., Lau, C., Lazarz, E. T., Lee, C., Lemon, T. A., Li, L., Li, Y., Morris, J. A., Overly, C. C., Parker, P. D., Parry, S. E., Reding, M., Royall, J. J., Schulkin, J., Sequeira, P. A., Slaughterbeck, C. R., Smith, S. C., Sodt, A. J., Sunkin, S. M., Swanson, B. E., Vawter, M. P., Williams, D., Wohnoutka, P., Zielke, H. R., Geschwind, D. H., Hof, P. R., Smith, S. M., Koch, C., Grant, S. G. N., & Jones, A. R. (2012). An anatomically comprehensive atlas of the adult human brain transcriptome. Nature, 489, 391–399.

He, B. J., Zempel, J. M., Snyder, A. Z., & Raichle, M. E. (2010). The temporal structures and functional significance of scale-free brain activity. Neuron, 66, 353–369.

Hermes, D., Miller, K. J., Wandell, B. A., & Winawer, J. (2015). Stimulus dependence of gamma oscillations in human visual cortex. Cereb. Cortex, 25, 2951–2959.

Hockett, C. F. (1960). The origin of speech. Sci. Am., 203, 89–96.

Hutchins, E. (1995). Cognition in the Wild. (MIT Press).

Jacobs, J. & Kahana, M. J. (2010). Direct brain recordings fuel advances in cognitive electrophysiology. Trends Cogn. Sci., 14, 162–171.

Kiebel, S. J., Garrido, M. I., Moran, R. J., & Friston, K. J. (2008). Dynamic causal modelling for EEG and MEG. Cogn. Neurodyn., 2, 121–136.

Kopell, N., Ermentrout, G. B., Whittington, M. A., & Traub, R. D. (2000). Gamma rhythms and beta rhythms have different synchronization properties. Proc. Natl. Acad. Sci. U. S. A., 97, 1867–1872.

Kutas, M. & Hillyard, S. A. (1980). Reading senseless sentences: brain potentials reflect semantic incongruity. Science, 207, 203–205.

Maidenbaum, S., Miller, J., Stein, J. M., & Jacobs, J. (2018). Grid-like hexadirectional modulation of human entorhinal theta oscillations. Proc. Natl. Acad. Sci. U. S. A., 115, 10798–10803.

Manning, J. R., Jacobs, J., Fried, I., & Kahana, M. J. (2009). Broadband shifts in local field potential power spectra are correlated with single-neuron spiking in humans. J. Neurosci., 29, 13613–13620.

Moser, E. I., Kropff, E., & Moser, M.-B. (2008). Place cells, grid cells, and the brain's spatial representation system. Annu. Rev. Neurosci., 31, 69–89.

Mukamel, R., Gelbard, H., Arieli, A., Hasson, U., Fried, I., & Malach, R. (2005). Coupling between neuronal firing, field potentials, and FMRI in human auditory cortex. Science, 309, 951–954.

Núñez, R. E. (2017). Is there really an evolved capacity for number? Trends Cogn. Sci., 21, 409–424.

Panzeri, S., Macke, J. H., Gross, J., & Kayser, C. (2015). Neural population coding: combining insights from microscopic and mass signals. Trends Cogn. Sci., 19, 162–172.

Pesaran, B., Vinck, M., Einevoll, G. T., Sirota, A., Fries, P., Siegel, M., Truccolo, W., Schroeder, C. E., & Srinivasan, R. (2018). Investigating large-scale brain dynamics using field potential recordings: analysis and interpretation. Nat. Neurosci., 21, 903–919.

Ray, S., Crone, N. E., Niebur, E., Franaszczuk, P. J., & Hsiao, S. S. (2008). Neural correlates of high-gamma oscillations (60-200 hz) in macaque local field potentials and their potential implications in electrocorticography. Journal of Neuroscience, 28, 11526–11536.

Ray, S. & Maunsell, J. H. R. (2011). Different origins of gamma rhythm and High-Gamma activity in macaque visual cortex. PLoS Biol., 9, e1000610.

Rosch, E., Thompson, E., & Varela, F. J. (1992). The Embodied Mind. Cognitive Science and Human Experience. (MIT Press).

Rugani, R., Vallortigara, G., Priftis, K., & Regolin, L. (2015). Animal cognition. number-space mapping in the newborn chick resembles humans' mental number line. Science, 347, 534–536.

Seed, A. & Byrne, R. (2010). Animal tool-use. Curr. Biol., 20, R1032–9.

Sherman, M. A., Lee, S., Law, R., Haegens, S., Thorn, C. A., Hämäläinen, M. S., Moore, C. I., & Jones, S. R. (2016). Neural mechanisms of transient neocortical beta rhythms: Converging evidence from humans, computational modeling, monkeys, and mice. Proc. Natl. Acad. Sci. U. S. A., 113, E4885–94.

Stachenfeld, K. L., Botvinick, M. M., & Gershman, S. J. (2017). The hippocampus as a predictive map. Nat. Neurosci., 20, 1643–1653.

Townsend, S. W., Engesser, S., Stoll, S., Zuberbühler, K., & Bickel, B. (2018). Compositionality in animals and humans. PLoS Biol., 16, e2006425.

Trujillo, C. A., Gao, R., Negraes, P. D., Gu, J., Buchanan, J., Preissl, S., Wang, A., Wu, W., Haddad, G. G., Chaim, I. A., Domissy, A., Vandenberghe, M., Devor, A., Yeo, G. W., Voytek, B., & Muotri, A. R. (2019). Complex oscillatory waves emerging from cortical organoids model early human brain network development. Cell Stem Cell, 0.

Van Essen, D. C., Smith, S. M., Barch, D. M., Behrens, T. E. J., Yacoub, E., Ugurbil, K., & WU-Minn HCP Consortium (2013). The WU-Minn human connectome project: an overview. Neuroimage, 80, 62–79.

Varela, F., Lachaux, J. P., Rodriguez, E., & Martinerie, J. (2001). The brainweb: phase synchronization and large-scale integration. Nat. Rev. Neurosci., 2, 229–239.

Voytek, B. (2016). The virtuous cycle of a data ecosystem. PLoS Comput. Biol., 12, e1005037.

Voytek, B. (2017). Social media, open science, and data science are inextricably linked. Neuron, 96, 1219–1222.

Voytek, B. & Knight, R. T. (2015). Dynamic network communication as a unifying neural basis for cognition, development, aging, and disease. Biol. Psychiatry, 77, 1089–1097.

Wang, X.-J. (2010). Neurophysiological and computational principles of cortical rhythms in cognition. Physiol. Rev., 90, 1195–1268.

Waschke, L., Tune, S., & Obleser, J. (2019). Local cortical desynchronization and pupil-linked arousal differentially shape brain states for optimal sensory performance. Elife, 8.

Chapter 1

Nested oscillatory dynamics in cortical organoids model early human brain network development

Abstract

Structural and transcriptional changes during early brain maturation follow fixed developmental programs defined by genetics. However, whether this is true for functional network activity remains unknown, primarily due to experimental inaccessibility of the initial stages of the living human brain. Here, we developed human cortical organoids that dynamically change cellular populations during maturation, and exhibited consistent increases in electrical activity over the span of several months. The spontaneous network formation displayed periodic and regular oscillatory events that were dependent on glutamatergic and GABAergic signaling. The oscillatory activity transitioned to more spatiotemporally irregular patterns, while synchronous network events resembled features similar to those observed in preterm human electroencephalography. These results show that the development of structured network activity in a human neocortex model

may follow stable genetic programming. Our approach provides opportunities for investigating and manipulating the role of network activity in the developing human cortex.

1.1 Introduction

Diverse and hierarchical cellular networks develop into circuits with patterns of functional spatiotemporal activity to form the human brain. Neural oscillations, a prominent, rhythmic brain signal found across species, robustly track behavioral and disease states, and have long been leveraged in systems neuroscience due to their ubiquity and accessibility (Buzsáki & Draguhn, 2004; De Hemptinne et al., 2015; Fries, 2005; Henriques & Davidson, 1991; Khan et al., 2013; Uhlhaas & Singer, 2010). These complex network dynamics emerge early in development, and is unclear if shaped exclusively by biological programming prenatally (Blankenship & Feller, 2010; Johnson, 2001; Power et al., 2010). In vitro and in vivo rodent studies have shown that a conserved repertoire of organized network activity, such as traveling waves, giant depolarizing potentials, and early network oscillations, develops according to a consistent timeline prior to and immediately after birth (Allene et al., 2008; Khazipov & Luhmann, 2006; Uhlhaas et al., 2010). However, due to an inability to interrogate the electrophysiology of intact embryonic brains, it remains unknown whether the same happens in humans. As a result, our knowledge about human brain functional development rests upon observations from nonhuman model systems.

Organoids generated from induced pluripotent stem cells (iPSC) have emerged as a scaled-down and three-dimensional model of the human brain, mimicking various developmental features at the cellular and molecular levels (Camp et al., 2015; Cederquist et al., 2019; Giandomenico et al., 2019; Lancaster & Knoblich, 2014; Lancaster et al., 2013; Luo et al., 2016; Mariani et al., 2012; Paşca et al., 2015; Qian et al., 2016; Renner et al., 2017; van de Leemput et al., 2014; Xiang et al., 2017, 2019). Despite recent advances in the understanding of their cellular diversity, there is no evidence that these organoids develop complex and functional neural network activity that resembles early human brain formation (Birey et al., 2017; Giandomenico et al., 2019; Quadrato et al., 2017). Therefore, researchers have not yet clearly determined whether brain organoids are a suitable model for neural network dynamics (Kelava & Lancaster, 2016; Paşca, 2018).

Here, we use human iPSCs to generate cortical organoids that exhibit evolving cellular transcriptional profile and nested oscillatory network dynamics over the span of several months. We subsequently investigated the molecular basis of human oscillatory activity formation, maintenance, and temporal control. Finally, we applied supervised machine learning with cross-validation to evaluate the similarity between electrophysiological network activity patterns of the in vitro model and human preterm neonatal electroencephalogram (EEG). Our findings suggest that organoid models are suitable for the investigation of the physiological basis of network formation at early and late stages of the human brain development. This prolonged evaluation of cortical organoid activity expands our understanding of the emergence of network-level neurodynamics in humans.

1.2 Results

Generation of functional cortical organoids

Despite the structural and transcriptional similarities between brain organoids and the developing nervous system, the emergence of higher-level complex network activity comparable to the living human brain remains largely untested (Figure 1.1A). To investigate the formation of a functional network, we promoted cortical specification by previously described protocols (Paşca et al., 2015; Thomas et al., 2017; Yoon et al., 2019) (Figure 1.1B, see Methods for details). At the beginning of differentiation, an abundance of proliferative neural progenitor cells (NPCs) (expressing Ki67, SOX2 and Nestin) that self-organized into a polarized neuroepithelium-like structure was observed. Similar to human cortical development in vivo, the proliferative zone around a lumen delimited by β-catenin+ cells was surrounded by progenitor cells. Progressively, the organoids increased in size and in the proportion of mature neurons (expressing NeuN and MAP2) to ultimately develop into concentric multilayer structures composed of NPCs, intermediate progenitors (TBR2, also known as EOMES), and lower (CTIP2, also known as BCL11B) and upper (SATB2) cortical layer neurons (Figure 1.1C-E and 1.5). The neurons exhibit dendritic protrusions and synaptic ultrastructure (Figure 1.1F and 1.1G). After 6 months, inhibitory neurons can also be observed (calretinin CR, also known as CALB2; GABAB; NKX2.1, also known as TTF1; GABA; LHX6; somatostatin SST and parvalbumin PV) (Figure 1.1D and 1.5). Although the initial fraction of GFAP-positive cells was less than 5%, this population increased to about 30-40% after 6 months of differentiation (Figure 1.1D and 1.1E).

To characterize the cellular diversity of cortical organoids during development, we performed single-cell RNA-seq on 1-, 3-, 6-, and 10-month organoids (Figure 1.1H-M, Figure 1.5 and Table 1.1). We used unsupervised clustering on the combined dataset of 15,990 cells to identify clusters and their relative abundance at distinct time points. Based on the expression gene markers, we combined smaller subclusters into five major cell classes: progenitors, intermediate progenitors, glial cells, glutamatergic neurons and GABAergic neurons. Based on this annotation, 1-month organoids consisted of > 70% progenitor cells (expressing SOX2 and PAX6) (Figure 1.1J and 1.1M). At the 3- and 6-month stage, cortical organoids comprised mainly glia (SLC1A3) and glutamatergic neurons (GRIA2 and SNAP25) (Figure 1.1J and 1.1M). The glial cells started with a small population, and increased to around 40% of cells present in the cortical organoids. Remaining populations of progenitors (around 5%) and intermediate progenitors (around 10%) were present throughout the maturation. A fraction of glutamatergic neurons at the 3- and 6-month time point expressed subunits of GABAergic receptors such as GABRB3 (Figure 1.5C). This expression of GABAergic receptors predates the appearance of interneurons.

Figure 1.1: Cellular and molecular development of human cortical organoids. (A) Overview of human neural network formation and dynamics evaluation using cortical organoids. (B) Schematic of the protocol used to generate cortical organoids. Scale bar, 200 μm. (C) Organoid growth during different developmental stages. (D) Representative immunostainings showing proliferating NPCs (Ki67 and Nestin), lower (TBR1 and CTIP2) and upper (SATB2) cortical layer neurons, glial cells (GFAP) and GABAergic (CR) neurons overtime. Scale bar, 50 μm. (E) Population analysis of specific markers indicating stages of maturation and multiple neuronal subtypes. The data are shown as mean ± s.e.m. (n = 8). (F) Representative image of a pyramidal neuron; dendritic structures are observed in cells transduced with the SYN:EGFP reporter (scale bar, 5 μm). (G) Electron microscopy of synaptic ultrastructure in 4-month cortical organoids (blue). Scale bar, 200 nm. (H) Uniform manifold approximation and projection (UMAP) plot of 15,990 cells from integrating datasets on 1-, 3-, 6-, and 10-month cortical organoids. Colors denote cells sampled from four different time points. (I) UMAP plot of the integrated datasets colored by seven main cell clusters. Red as GABAergic neurons, orange as glutamatergic neurons, blue as glia cells, green as intermediate progenitors, purple as progenitors, green blue as mitotic cells, and grey as others. (J) Separate UMAP plots of integrated data by different time points. Same color scheme used for main cell clusters. (K) Dot plots showing cluster specific gene expression across main cell clusters. (L) UMAP plots showing expression levels of cell-type specific markers (see Figure 1.5 for additional markers). (M) Barplots of proportion of cell types at individual time points.

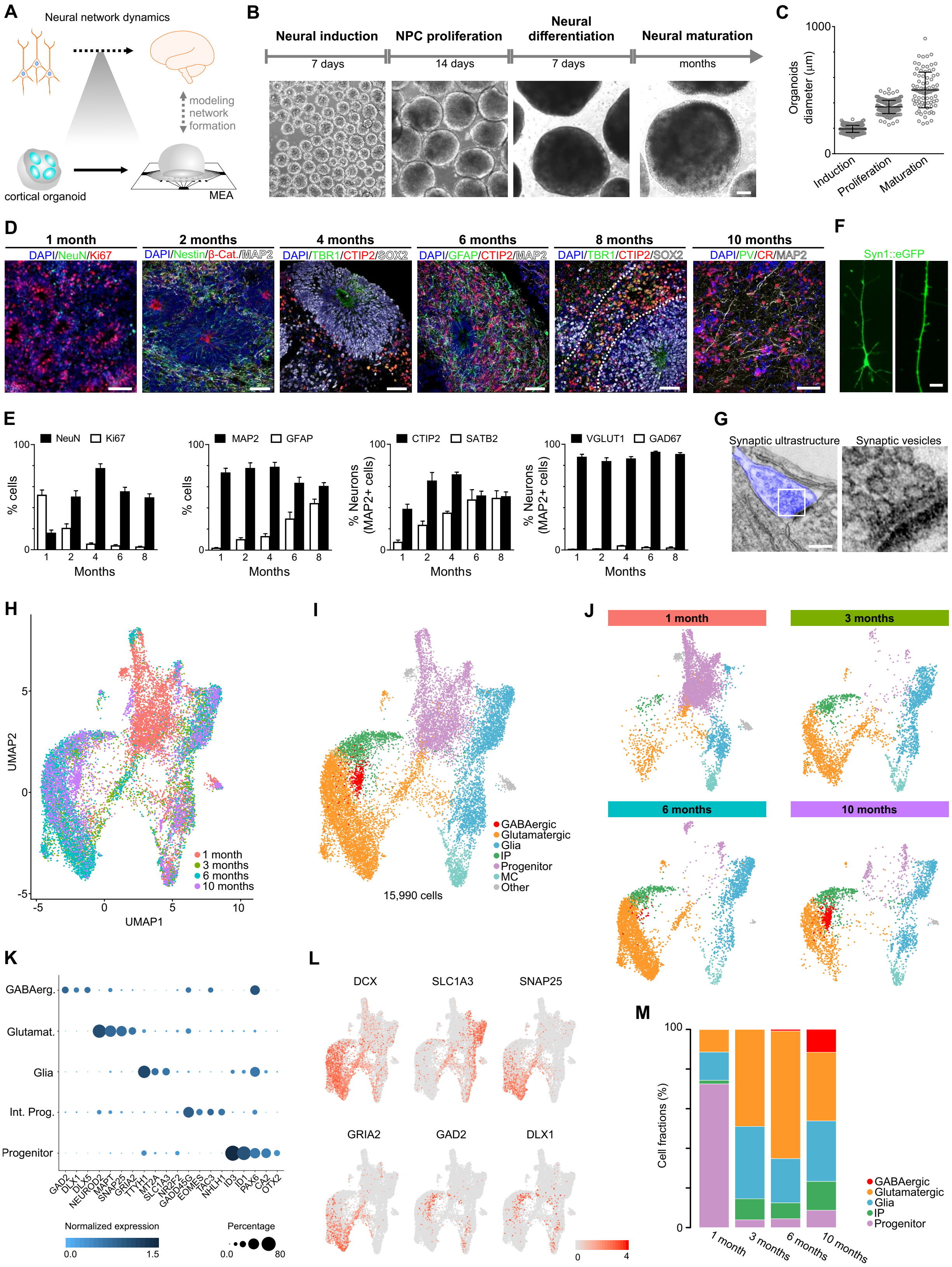
A
Neural network dynamics
modeling network formation
cortical organoid
MEA
B
Neural induction
NPC proliferation
Neural differentiation
Neural maturation
7 days
14 days
7 days
months
C
1000
0
Organoids diameter (µm)
Induction
Proliferation
Maturation
D
1 month
DAPI/NeuN/Ki67
2 months
DAPI/Nestin/β-Cat./MAP2
4 months
DAPI/TBR1/CTIP2/SOX2
6 months
DAPI/GFAP/CTIP2/MAP2
8 months
DAPI/TBR1/CTIP2/SOX2
10 months
DAPI/PV/CR/MAP2
F
Syn1::eGFP
E
NeuN
Ki67
% cells
Months
MAP2
GFAP
% cells
Months
CTIP2
SATB2
% Neurons (MAP2+ cells)
Months
VGLUT1
GAD67
% Neurons (MAP2+ cells)
Months
100
0
1
2
4
6
8
G
Synaptic ultrastructure
Synaptic vesicles
H
UMAP2
UMAP1
5
0
-5
10
1 month
3 months
6 months
10 months
I
GABAergic
Glutamatergic
Glia
IP
Progenitor
MC
Other
15,990 cells
J
1 month
3 months
6 months
10 months
K
GABAerg.
Glutamat.
Glia
Int. Prog.
Progenitor
GAD2
DLX1
DLX5
NEUROD2
MAPT
SNAP25
GRIA2
TTYH1
MT2A
SLC1A3
NR2F2
GADD45G
EOMES
TAC3
NHLH1
ID3
ID1
PAX6
CA2
OTX2
Normalized expression
0.0
1.5
Percentage
0.0
80
L
DCX
SLC1A3
SNAP25
GRIA2
GAD2
DLX1
0
4
M
100
0
Cell fractions (%)
1 month
3 months
6 months
10 months
GABAergic
Glutamatergic
Glia
IP
Progenitor

GABAergic neurons were mainly restricted to 6- to 10-month organoids as indicated by expression of GAD2 (also known as GAD65), DLX1 and DLX5 (Figure 1.1J-M, Figure 1.5C and D), reaching around 15% of the total neuronal population after 10 months of maturation, consistent with its presence later in the in vivo development (Uylings et al., 2002). The molecular profile of GABAergic neurons was further evaluated by single-cell transcriptomics (Figure 1.5E) and by the presence of protein markers (Figure 1.5F). To further demonstrate the biosynthesis of GABA during the maturation process, we employed metabolomics liquid chromatography coupled to mass spectrometry (Gertsman et al., 2014). The neurotransmitter GABA was detected in the culture media of cortical organoids after 6 months of maturation (Figure 1.5G), in a physiological relevant concentration (Van Hove & Thomas, 2014). These results suggest the presence of the basic components for the generation of a neural network in a developing human cortical in vitro model.

Emergence of nested oscillatory network activity

In addition to the observed cellular diversity and expression of synaptic markers, we interrogated the presence of functional network activity. Starting at a single cellular level, we used whole-cell patch-clamp recording from 6-month cortical organoids (Figure 1.6 A-E). The action potential firing activity and the voltage-dependent Na+ current were tetrodotoxin (TTX) sensitive. Application of glutamate receptor antagonists (NBQX and AP5) fully inhibited the spontaneous excitatory postsynaptic currents recorded at -60 mV, confirming the presence of functional excitatory neurons.

Figure 1.2: Oscillatory network dynamics in long-term cortical organoids. (A) Schematic of the organoid signal processing pipeline. Raw MEA data is analyzed as population spiking and LFP separately. Synchronous network events are highlighted in yellow. (B) Raster plot of network spiking activity after 1.5 and 6 months of maturation. A 3-s interval of activity over 5 channels is shown in the upper right corners. (C) Cortical organoids show elevated and continuously increasing mean firing rate compared to 2D monolayer neurons (n = 8 for organoid cultures, and n = 12 for 2D neurons). Inset, correlation of the firing rate vector over 12 weeks of differentiation (from 8 to 20) between pairs of cultures showing reduced variability among organoid replicates. (D) Temporal evolution of cortical organoid network activity. Detailed definitions and further parameters are presented in Figure 1.6. (E) Time series of population spiking and LFP during network events in cortical organoid development. Each overlaid trace represents a single event during the same recording session. The number of subpeaks during an event (F) is maximized and stereotypical at 6-months, developing nonlinearly and following an inverted-U trajectory. (G) Network variability, measured as the coefficient of variation of the inter-event interval, increases monotonically throughout development. (H) 1-4 Hz oscillatory power in the LFP increases up to the 25th week in culture and plateaus at 30 weeks. Inset, oscillatory power is calculated by fitting a straight line (dashed) over the aperiodic portion of the PSD and taken as the height of narrow peaks rising above the linear fit. (I) Pairwise correlation of LFP across all electrodes (coherence) within a well during network events initially increase, then decreases after 30 weeks. (J) An example of sequential frames during a network event show the spatial propagation of wave spreading, then disappearing again after 100ms. The data shown in C, D, F, G, H, and I are presented as mean ± s.e.m. $^{*}P < 0.05$, $^{**}P < 0.01$, $^{***}P < 0.001$, unpaired Student’s t-test (C), quadratic (F, H and I) and linear (G) regression.

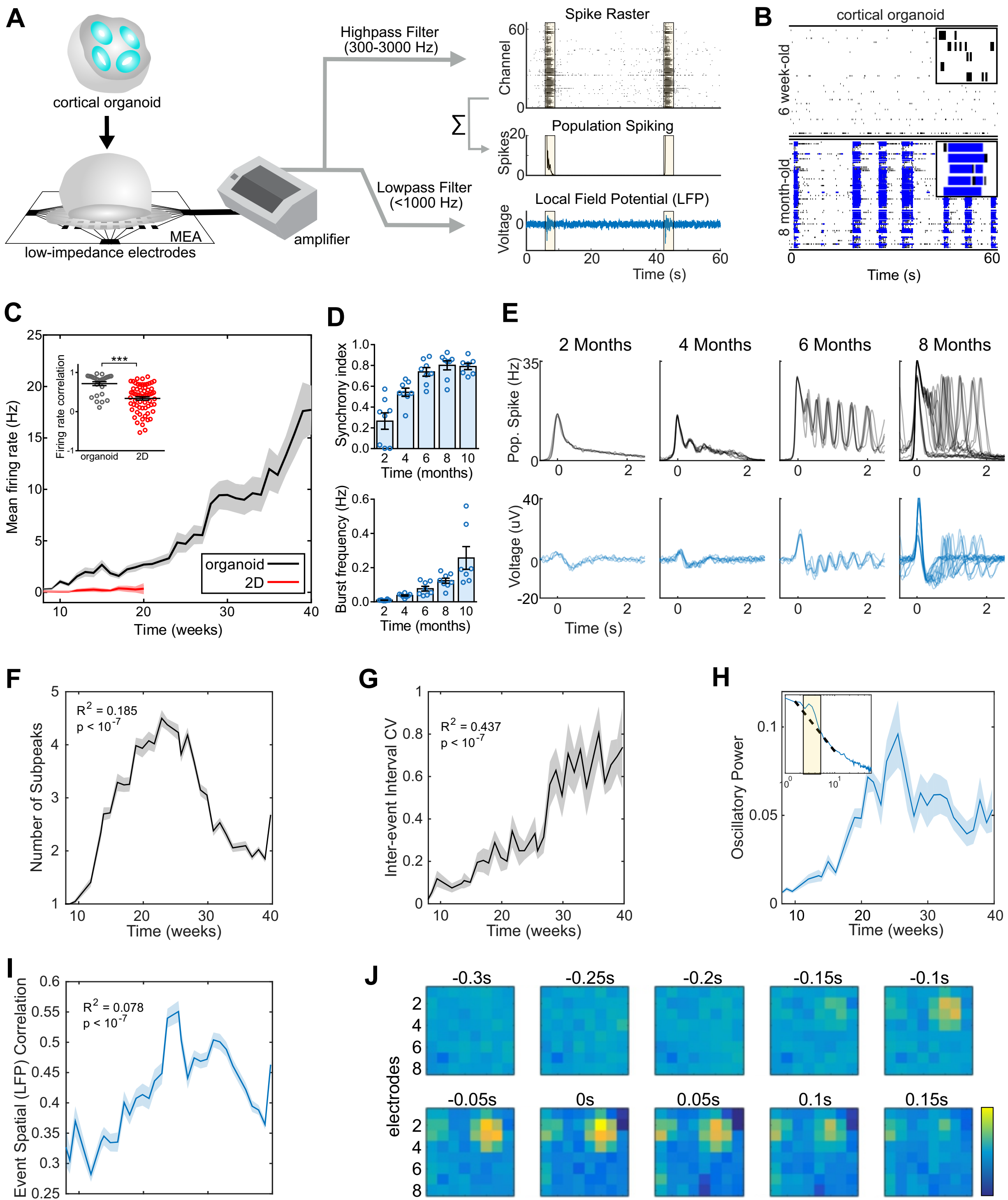
A
cortical organoid
MEA
low-impedance electrodes
amplifier
Highpass Filter
(300-3000 Hz)
Lowpass Filter
(<1000 Hz)
Spike Raster
Channel
60
0
∑
Population Spiking
Spikes
20
0
Local Field Potential (LFP)
Voltage
0
0
20
40
60
Time (s)
B
cortical organoid
6 week-old
8 month-old
0
60
Time (s)
C
Mean firing rate (Hz)
25
20
15
10
5
0
10
20
30
40
Time (weeks)
Firing rate correlation
1
0
-1
***
organoid
2D
organoid
2D
D
Synchrony index
1.0
0.8
0.6
0.4
0.2
0.0
2
4
6
8
10
Time (months)
Burst frequency (Hz)
0.6
0.4
0.2
0.0
2
4
6
8
10
Time (months)
E
2 Months
4 Months
6 Months
8 Months
Pop. Spike (Hz)
35
0
0
2
Voltage (uV)
40
0
-20
Time (s)
F
Number of Subpeaks
5
4
3
2
1
$R^2 = 0.185$
$p < 10^{-7}$
10
20
30
40
Time (weeks)
G
Inter-event Interval CV
1
0.8
0.6
0.4
0.2
0
$R^2 = 0.437$
$p < 10^{-7}$
10
20
30
40
Time (weeks)
H
Oscillatory Power
0.1
0.05
0
10^0
10^1
10
20
30
40
Time (weeks)
I
Event Spatial (LFP) Correlation
0.6
0.55
0.5
0.45
0.4
0.35
0.3
0.25
$R^2 = 0.078$
$p < 10^{-7}$
10
20
30
40
Time (weeks)
J
-0.3s
-0.25s
-0.2s
-0.15s
-0.1s
-0.05s
0s
0.05s
0.1s
0.15s
electrodes
2
4
6
8

To further evaluate the cortical organoid functionality in a mesoscopic level, we performed weekly extracellular recordings of spontaneous electrical activity using multi-electrode arrays (MEA). Cortical organoids were plated per well in 8 wells of a MEA plate containing 64 low-impedance (0.04 MΩ) platinum microelectrodes with 30 μm of diameter spaced by 200 μm, yielding a total of 512 channels. We separately analyzed single-channel and population firing characteristics derived from channel-wise spike times and the local field potential (LFP), a measure of aggregate synaptic currents and other slow ionic exchanges (Buzsáki et al., 2012) (Figure 1.2A). The spikes, also refer here as events, were defined by the event unit waveforms standard structure with typical refractory periods and by pharmacological intervention. These spikes or events from each channel do not represent putative single-unit action potentials, but represent multi-unit activity (MUA). Since both the spatial and temporal resolution of MEA sampling is sparse, single-unit spike trains were not isolated, instead submitting channel-wise and whole-well activity for further analysis, rather than individual event trains. Over the course of 10 months, cortical organoids exhibited consistent increases in electrical activity, as parametrized by channel-wise firing rate, burst frequency, and synchrony (Figure 1.2B-D and Figure 1.6F-I), which indicates a continually-evolving neural network. Additionally, the variability between replicates over 40 weeks of differentiation was significantly lower compared to iPSC-derived neurons in monolayer cultures (Figure 1.2C inset and Figure 1.6J).

During individual recordings, cultures displayed a robust pattern of activity, switching between long periods of quiescence and short bursts of spontaneous network-synchronized spiking (hereafter referred to as “network events”). These network events were periodic (0.05 Hz) but infrequent early in development (2 months), occurring roughly every 20 seconds and decayed monotonically after the initial onset (Figure 1.2E). From 4-months onwards, a secondary peak emerged 300-500 ms after the initial network activation, leading to the presence of a nested faster oscillatory (2-3 Hz) pattern up to 6-months in culture (Figure 1.2F and Figure 1.7A-F). Notably, this robust fast timescale nested oscillation was not observed in 3D neurospheres, suggesting that the spherical arrangement of neurons is insufficient for the emergence of nested oscillations (Figure 1.7G-J). The regular oscillatory activity during network events transitioned to stronger, yet more variable, oscillations over time. To quantify this network complexity, we tracked the regularity (coefficient of variation of inter-event intervals, CV) and the spatial and temporal correlation between spontaneous network events. The inter-event interval CV consistently increased over 10 months of differentiation (Figure 1.2G), from extremely regular latencies (CV ≈ 0) at 2 months to irregular, Poisson-like (CV ≈ 1) at 10 months. This indicates increased variability between consecutive network events initiation. Additionally, spatial and temporal irregularity on a shorter time-scale (within-event) also increased with development, suggesting a breakdown of deterministic population dynamics from the onset of network events.

Periodic oscillatory activity is often defined as a "bump" over the characteristic 1/f background in the power spectral density (PSD) of extracellular signals above-and-beyond the aperiodic 1/f signal (Buzsáki et al., 2013; Gao et al., 2017). In organoid LFPs, we observed both prominent oscillatory peaks in the low-frequency range (1-4 Hz) and in the aperiodic signal characteristic of neural recordings (Ben-Ari, 2001; Voytek et al., 2015). The development of oscillatory activity in cortical organoids over time was quantified by computing the PSD for each LFP recording (Figure 1.2H, inset). Oscillatory power in the delta range (1-4 Hz) increased for up to 24 weeks in culture, tapering off slightly in subsequent recordings and plateauing during the last 10 weeks. This inverted-U trajectory reflects the network's initial acquisition of oscillatory modes at steady frequencies and the dispersion of this regularity at later time points. The LFP results reveal the development of the cortical organoid cultures across different network states: from sparse activity with extreme rigidity and regularity, to one that acquires repetitive and regular oscillatory patterns (Voytek & Knight, 2015), until it finally reaches a stage of higher spatiotemporal complexity and variability that is reminiscent of self-organized networks (Tetzlaff et al., 2010) (Figure 1.2I,J and Figure 1.7C-F).

Oscillatory coordination of neural ensembles and its synaptic mechanisms

Oscillatory dynamics have been postulated to coordinate spiking across neural ensembles. In the LFP and other mesoscopic brain signals, this manifests as a phenomenon known as cross-frequency phase-amplitude coupling (PAC) (Voytek & Knight, 2015), wherein the high-frequency content of the LFP is entrained to the phase of slow oscillations (Manning et al., 2009; Miller et al., 2007; Mukamel et al., 2005). In the cortical organoids, we observed greater PAC between oscillatory delta (1-4 Hz) and broadband gamma activity (100-400 Hz, see Methods) during network events compared to quiescent periods (Figure 1.3A-C). This broadband gamma is non-oscillatory, but has been shown to be an LFP surrogate of population spiking (Manning et al., 2009; Miller et al., 2007).

We further evaluated the role of glutamatergic and GABAergic synaptic transmission in forming oscillations by pharmacological intervention. Organoid neural networks were susceptible to both glutamate receptor antagonists (AP5 and CNQX; NMDA and AMPA/kainate, respectively) and GABA receptor agonists (muscimol, GABAA; baclofen, GABAB) by significantly reducing the number of spikes events and bursts, with a subsequent extinction of synchronous activity. The electrical activity was abolished in the presence of TTX (Figure 1.3D and 1.3E). Blockade of GABAergic transmission by bicuculline increased the number of network-synchronized events and did not affect peak population firing rates, but abolished nested 2 Hz oscillatory activity by erasing subsequent reverberant peaks (Figure 1.3F).

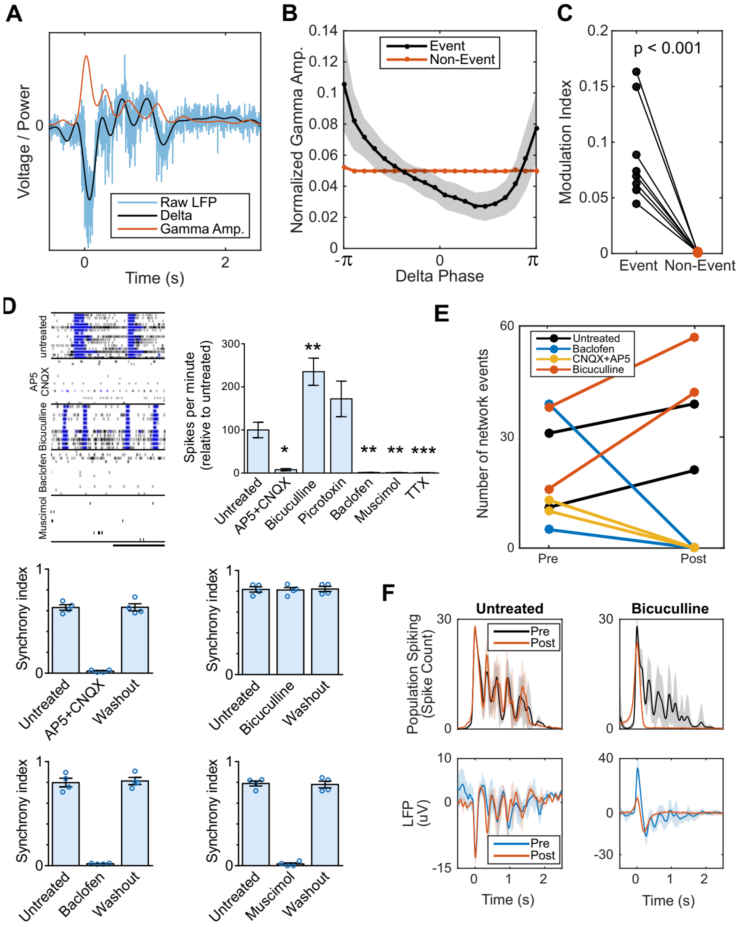

Figure 1.3: Cortical organoid serves as a model of functional oscillations and their synaptic mechanisms. (A-C) Phase-amplitude coupling is observed in organoid LFP during network events. (A) Example of raw LFP during a network event decomposed into its low-frequency component (1-4 Hz delta) and the amplitude envelope of the high-frequency, broadband gamma component (200-400 Hz). Analysis was repeated for 100-200 Hz with near identical effect size and significance. (B) Normalized gamma amplitude binned by delta phase during network events (black) shows greater modulation depth by low frequency delta than during non-event periods (red). (C) Phase-amplitude coupling during network events is significantly greater than non-event periods in all batches. (D) Effect of selective drug treatments on neuronal electrical activity in 6-month organoids. Representative raster plots and burst measurements of untreated and treated organoids. The pharmacological manipulation was performed using cortical organoid plated on 4 MEA wells (n = 4, cortical organoid culture for each treatment). Scale bar, 20 s. Exposure to AP5 + CNQX, baclofen and muscimol reversibly extinguish the network bursts (synchrony), while no changes were promoted by bicuculline. (E-F) Pharmacological perturbation of oscillatory activity during network events in 6-month organoids. Pre and post refer to before treatment administration and after administration, respectively. Application of bicuculline and picrotoxin increases the number of network events, while CNQX + AP5 and baclofen completely abolish synchronized network events. Bicuculline blocks oscillatory network activity but not the network event itself. Data are shown as mean ± s.e.m.; unpaired Student's t-test.

Cortical organoid network development resembles some preterm EEG features

Despite emergence of complex oscillatory network activity in organoids, it is unclear whether the spontaneous developmental trajectory observed is representative of programmed early neurodevelopment. While network activity from cortical organoids does not exhibit the full temporal complexity seen in adults, the pattern of alternating periods of quiescence and network-synchronized events resembles electrophysiological signatures present in preterm human infant EEG. During trace discontinu (Tolonen et al., 2007), quiescent periods are punctuated by high-amplitude oscillations (spontaneous activity transients, SATs) lasting a few seconds. Intervals of complete quiescence disappear as infants become of term, and the EEG is dominated by continuous and low-amplitude desynchronized activity in adult brains (Figure 1.4A, Figure 1.8A and B).

Due of the inability to interrogate the electrophysiology of intact human embryonic brains, we attempted to quantitatively compare network activity in cortical organoids to preterm human EEG. We analyzed a publicly available dataset of 101 serial EEG recordings from 39 preterm infants ranging from 24 to 38 weeks post-menstrual age (PMA); 567 data points total (Stevenson et al., 2017). The dataset contains 23 precomputed features for each EEG record, ranging from timing, rate, and variability of SATs (or bursts), as well as spectral power in canonical oscillatory bands (delta, theta, etc., see Table 1.2 for full list of features). We computed analogous features from each organoid LFP recording when appropriate. It is important to note that the biophysics of scalp EEG is drastically different from extracellular field potential in the organoid, due to factors such as spatial filtering by the scalp and orientation of neuronal populations in relation to the recording electrode. Therefore, we selected a subset of 12 features to compare in the organoid LFP (highlighted in Table 1.2), the majority of those correspond to duration and timing of SATs. While features like EEG standard deviation (or root mean square, RMS) and interhemispheric synchrony are likely altered by skull thickening during early development, the large amplitude network synchronous events are reliably detected in both EEG and LFP. Timing features derived from SAT times (duration, inter-SAT interval, etc.) were compared between cortical organoid and preterm neonates.

By comparing specific timing features between cortical organoids and preterm infants, we found a range of correlations in the developmental trajectory of features with age, as well as similarities in development between the two datasets (Figure 1.4B and C). For instance, “SATs per hour” (“events per hour” in organoids, Figure 1.4B) and 95-percentile of inter-SAT duration distribution showed high similarity both in absolute value and their developmental trajectory (correlation with age), while “root-mean-square SAT duration” and median (50%) SAT duration show different trends and absolute value, from 25 to 38 weeks in both datasets (all features presented in Figure 1.8C and D). To compare the similarity of developmental trajectory quantitatively, we computed the average resampled correlation between each feature and developmental time in both datasets (Figure 1.4C and Figure 1.8D, see Methods for details). These results summarize what is shown in Figure 1.4B: SATs per hour consistently increase during development in both organoids and preterm infants, while the variability of SAT duration (TSAT RMS) consistently decrease. Other features show inconsistent developmental trajectories over time between organoid LFPs and preterm EEGs.

Figure 1.4: Cortical organoid network dynamics mimic premature neonates after 28 weeks of maturation. (A) Representative LFP trace from cortical organoid, highlighting instances of network events (yellow). Comparable events between periods of quiescence (discontinuous network dynamics) are shown in human preterm neonate EEG at 35 weeks gestational age, while a different pattern of continuous activity is observed in adult EEG. SAT: spontaneous activity transient. (B) Examples of analogous features in preterm neonate EEG and organoid LFP show various levels of similarity throughout development. RMS: root mean square; 50%/95% refer to 50th and 95th percentile of feature distribution within a recording. (C) Pearson's correlation coefficients between age and electrophysiological features (mean ± std of bootstrapped distribution) for both organoid and premature neonates show different degrees of developmental similarity for individual features (12 total selected). For example, SATs (events) per hour shows remarkable similarity over time between organoid and neonates. (D) Schematic of machine learning procedure for age prediction: EEG features from 39 premature neonates (n = 567 recordings) between 25- and 38-weeks PMA (post-menstrual age) were used to train and cross-validate a regularized regression model (ElasticNet), optimizing for preterm neonate age prediction based on their EEG features only (top). The model was clamped after training, and applied directly on organoid LFP features and control datasets, including held-out preterm neonate data, mouse primary culture, 2D iPSC culture, and human fetal brain culture. (E) Model-predicted developmental time (y-axis, age in weeks) follows actual weeks-in-culture (x-axis) for organoids (orange and blue), as well as true age of held-out preterm neonate data points (black). Dashed line represents unity, signifying perfect prediction. Large circles on solid lines and shaded regions denote mean ± std of prediction, respectively, while dots indicate per-sample prediction (n = 8 for organoids at all time points). (F) Pearson's correlation coefficient between predicted and actual developmental time for organoid, and control datasets. Significant positive correlations indicate the model's ability to capture developmental trajectory in a particular dataset.

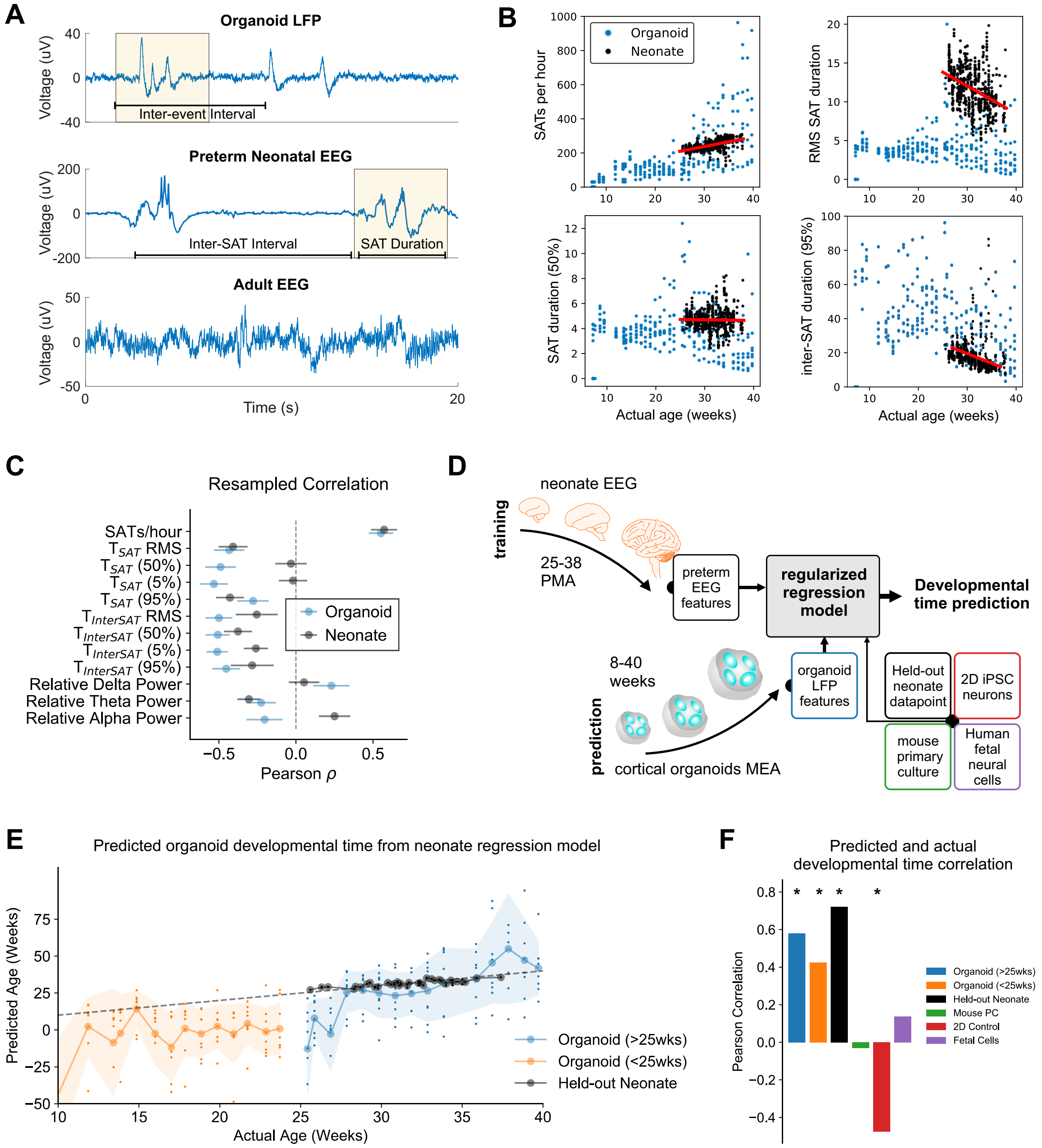
A
Organoid LFP
Voltage (uV)
40
0
-40
Inter-event Interval
Preterm Neonatal EEG
200
0
-200
Inter-SAT Interval
SAT Duration
Adult EEG
50
0
-50
0
20
Time (s)
B
Organoid
Neonate
SATs per hour
RMS SAT duration
SAT duration (50%)
inter-SAT duration (95%)
Actual age (weeks)
C
Resampled Correlation
SATs/hour
T_{SAT} RMS
T_{SAT} (50%)
T_{SAT} (5%)
T_{SAT} (95%)
$T_{InterSAT}$ RMS
$T_{InterSAT}$ (50%)
$T_{InterSAT}$ (5%)
$T_{InterSAT}$ (95%)
Relative Delta Power
Relative Theta Power
Relative Alpha Power
Organoid
Neonate
−0.5
0.0
0.5
Pearson ρ
D
neonate EEG
training
25-38
PMA
preterm EEG features
regularized regression model
Developmental time prediction
8-40
weeks
prediction
cortical organoids MEA
organoid LFP features
Held-out neonate datapoint
2D iPSC neurons
mouse primary culture
Human fetal neural cells
E
Predicted organoid developmental time from neonate regression model
Predicted Age (Weeks)
Actual Age (Weeks)
Organoid (>25wks)
Organoid (<25wks)
Held-out Neonate
F
Predicted and actual developmental time correlation
Pearson Correlation
*
*
*
*
Organoid (>25wks)
Organoid (<25wks)
Held-out Neonate
Mouse PC
2D Control
Fetal Cells

Taking in consideration the wide range of similarities observed across the two datasets, we asked which features' developmental trajectory were most informative of the developmental time, and whether those were conserved between organoids and preterm infants. To accomplish this in an objective fashion, we trained a regularized regression model with cross-validation (ElasticNet, L1 and L2 regularized), to predict preterm infant age from their EEG features. In other words, the regression model was only optimized to predict preterm infant age based on their EEG, and was blind to the organoid data. Following training and hyperparameter selection, the regression model was "locked" while we directly applied it on the organoid LFP dataset and various control datasets to obtain their predicted developmental time (Figure 1.4D). Although the regression model predicted organoid developmental time poorly before 25 weeks (Figure 1.4E, orange), and with high variability, mean predicted developmental time followed true age with much higher fidelity after 25 weeks (blue). A subset of the preterm EEG data held out during training was used to further validate the performance of the model (black), in addition to other control datasets, including mouse primary culture, iPSC monolayer culture, and human fetal brain culture (Figure 1.8E, details in Methods). To quantify how well developmental trend over time was captured by the regression model, we compute the Pearson correlation coefficient between the model-predicted age and the true age of the various datasets. Note that a significant positive correlation was only observed for organoid and held-out EEG datasets (Figure 1.4F). While the developmental trajectory of cortical organoids is not identical to, and more variable than, that of the fetal human brain, the two populations share similarities in how their network electrophysiological properties change over time, suggesting genetically programmed developmental timelines that can be detected by a simple machine learning algorithm.

1.3 Discussion

While brain organoids have been shown to mimic early human neurodevelopment at the cellular and molecular levels, evidence of network activity maturation and the corresponding cellular basis have not been previously explored. Here, we report the formation of small-scale functional electrophysiological networks in human cortical organoids while tracking their gene expression profile and cellular composition over time. Single cell RNA-seq at multiple time points spanning 10 months show development of various cellular subclusters, transitioning from progenitor cells to neuronal and glial populations. Cortical organoids begin to exhibit highly synchronous and stereotypical network activity (events) at 2 months, which transition into 2-3 Hz rhythmic activity by 4 to 6 months. Subsequently, network activity becomes more variable spatiotemporally, coinciding with the development of inhibitory populations. Oscillatory activity at 6 months exhibits cross-frequency coupling, a potential signature of functional neuronal network communication; pharmacological intervention demonstrates the causal involvement of glutamate and GABA in generating and sustaining oscillations. Finally, we observe similarities in the developmental trajectory of some electrophysiological features between organoids and human preterm infants, where a machine learning model trained to predict neonatal age from their EEG features can predict organoid developmental timeline. Taken altogether, these results demonstrate the utility of human stem cell-derived brain organoids as a viable neuroscience research model, not only for the shifting landscape of molecular and cellular composition, but also for the maturation of functional activity in brain networks during early neurodevelopment.

Diversity of excitatory and inhibitory populations

We used longitudinal single-cell transcriptional profiling followed by immunostaining and functional validation to demonstrate the cellular dynamics of cortical organoids during long-term development, revealing an unprecedented diversity of cell types. Notably, GABAergic neurons were mainly restricted to 6- to 10-month organoids, reaching around 10-15% of the total neuronal population after 10 months, consistent with its presence later in the in vivo development (Uylings et al., 2002). A metabolomic identification of GABA released in the culture media was further used to validate the presence and functionality of the GABAergic system. While our aim was not to investigate the origin of GABAergic neurons in the human neocortex, we cannot exclude the possibility of aberrant cellular differentiation, warranting further dissection of the cortical organoid model for novel neurodevelopmental pathways. The dynamic cell population and the presence of neurotransmitter systems suggest the activity of the basic components for the emergence of a neural network in a developing in vitro model.

Synchronous oscillations as a signature of functional network activity

The presence and changes of oscillations at fast timescales (>1 Hz) is a hallmark of the in vivo brain, while coupling across different frequencies has been proposed to coordinate the flow of information across regions (Buzsáki & Draguhn, 2004; Fries, 2005; Voytek et al., 2015). With the cellular components for the generation of a functional neural network in place, we tested if the cortical organoids display activity typically found in organized cortical networks. Robust extracellular electrical activity was observed at earlier stages and progressively developed into an organized oscillatory network. Cortical organoids initially exhibited periodic and highly regular nested oscillatory network events that were dependent on glutamatergic and GABAergic signaling. Our data suggest that GABA transmission is crucial for the maintenance, but not the initiation of faster oscillatory activity. This is consistent with accounts of inhibition rhythmically coordinating pyramidal populations' activity during early development (Opitz et al., 2002). Additionally, during periods of high network activity, the power of high-frequency (>100 Hz) activity is coupled to the phase of the 3 Hz oscillation in the local field potential. Without positing its functional role, this observation suggests that more complex oscillatory activity can indeed manifest and be studied in this in vitro system.

It is also unclear the biological basis of the increased variability in the number of spontaneous events in organoid cultures, especially after 28 weeks in culture. We believe that different factors could increasingly introduce variability or diversity into the neural population during maturation. In this context, since we started with single cells that aggregate to form organoids, small population differences at early stages of organoid formation could lead to changes in activity. Differences in the organoid positioning on the MEA and manipulation could also affect the signal acquisition. Additionally, we do not exclude the possibility of the formation of independent network profiles based on intrinsic activity and retro-feedback properties.

Comparing to the early developing brain: insights and limitations

Some features of early network dynamics in humans (e.g., spontaneous activity transients, SATs) can be recapitulated by the in vitro model, with no additional constraints other than structural and genetic similarities. The regularized regression model presented here was built on preterm EEG data only, following an internal cross-validation procedure to estimate the hyperparameters. It was then directly applied to organoid LFP data – previously unseen by the classifier – to produce a "predicted developmental time", in addition to data from several other cellular models for validation. Simultaneous MEA and EEG seizure recordings, in human subjects, share common features in the EEG frequency range (Schevon et al., 2012). However, when comparing the in vitro MEA and neonatal EEG features, it is crucial to remove any comparison of features affected by the spatial filtering properties of the skull. Moreover, there are a few factors that might challenge the interpretation of the regression model results. First, it is difficult to control external variation in infant EEG due to differences that may arise from the EEG acquisition system and electrodes positioning. Second, clinical confounds due to potential neurological condition and medications may also impact the dataset. Lastly, it is important to highlight that the regression model cannot be extended to neurotypical adult, as adult EEGs do not display the observed bursting patterns under normal conditions, thus the relevant features (e.g., SAT timing features) cannot be computed. Nonetheless, while we do not claim functional equivalence between the organoids and a full cortex – neonatal or adult – the current results represent the first step towards an in vitro model that captures some of the complex and oscillatory spatiotemporal dynamics of the human brain.

Conclusion

Given the potential roles of synchronized and oscillatory network dynamics in coordinating information flow between developed brain regions (Uhlhaas et al., 2010), these results highlight the potential for cortical organoids to advance our understanding of functional electrophysiology. Additionally, by applying spiking and LFP analysis that is traditional to animal models, our findings offer a link between microscale organoid physiology and systems neuroscience. Finally, considering the diversity and maturation of cell types generated, the robustness of the neuronal networks, the presence of structural traits of mature neurons and the possibility of using sensory experience to modulate neuronal activity collectively, cortical organoids may be used to model cellular interactions and neural circuit dysfunctions related to neurodevelopmental and neuropsychiatric pathologies. Importantly, this organoid model is small, approximately one million times smaller than the human brain, but ethical implications cannot be ignored about the future possibility of larger and more complex organoids (Farahany et al., 2018). Nevertheless, our findings illuminate a link between microscale organoid physiology and systems neuroscience. This offers a promising, small-scale experimental model of human neocortex to help address neurodevelopmental pathologies that affect millions of people, but otherwise lack an existing animal model.

1.4 Methods

Lead contact and materials availability

This study did not generate new unique reagents. Further information and requests should be addressed to and will be fulfilled by the Lead Contact, Alysson R. Muotri (muotri@ucsd.edu).

Experimental models

Human cell source. iPSC lines derived from control individuals have been previously characterized elsewhere (Nageshappa et al., 2016; Tang et al., 2016). iPSC colonies were expanded on Matrigel-coated dishes (BD Biosciences, San Jose, CA, USA) with mTeSR1 medium (StemCell Technologies, Vancouver, Canada). The cells were routinely checked by karyotype and CNV arrays to avoid genomic alterations in the culture. Embryonic samples were obtained from fetus brains and cultured in Neurobasal (Life Technologies, Carlsbad, CA, USA) supplemented with GlutaMAX (Life Technologies), 1% Gem21 NeuroPlex (Gemini Bio-Products, West Sacramento, CA, USA), 1% MEM nonessential amino acids (NEAA; Life Technologies), 1% penicillin/streptomycin (PS; Life Technologies). The study was approved by the University of California San Diego IRB/ESCRO committee (protocol 141223ZF).

Rodent cell source. Newborn mouse primary culture was performed as described elsewhere (Moore et al., 2019). The cells were maintained in Neurobasal medium with GlutaMAX, 1% Gem21 NeuroPlex, 1% NEAA and 1% PS. The study was approved by the University of California San Diego IACUC committee (protocol S09005).

Methods details

Generation of cortical organoids. Feeder-free iPSCs were fed daily with mTeSR1 for 7 days. Colonies were dissociated using Accutase (Life Technologies) in PBS (1:1) for 10 minutes at 37 °C and centrifuged for 3 minutes at 150 x g. The cell pellet was resuspended in mTeSR1 supplemented with 10 μM SB431542 (SB; Stemgent, Cambridge, MA, USA) and 1 μM Dorsomorphin (Dorso; R&D Systems, Minneapolis, MN, USA). Approximately 4 x 10^6 cells were transferred to one well of a 6-well plate and kept in suspension under rotation (95 rpm) in the presence of 5 μM ROCK inhibitor (Y-27632; Calbiochem, Sigma-Aldrich, St. Louis, MO, USA) for 24 hours to form free-floating spheres. After 3 days, mTeSR1 was substituted by Media1 [Neurobasal (Life Technologies) supplemented with GlutaMAX, 1% Gem21 NeuroPlex (Gemini Bio-Products), 1% N2 NeuroPlex (Gemini Bio-Products), 1% NEAA (Life Technologies), 1% PS (Life Technologies), 10 μM SB and 1 μM Dorso] for 7 days. Then, the cells were maintained in Media2 [Neurobasal with GlutaMAX, 1% Gem21 NeuroPlex, 1% NEAA and 1% PS] supplemented with 20 ng/mL FGF2 (Life Technologies) for 7 days, followed by 7 additional days in Media2 supplemented with 20 ng/mL of FGF2 and 20 ng/mL EGF (PeproTech, Rocky Hill, NJ, USA). Next, cells were transferred to Media3 [Media2 supplemented with 10 ng/mL of BDNF, 10 ng/mL of GDNF, 10 ng/mL of NT-3 (all from PeproTech), 200 μM L-ascorbic acid and 1 mM dibutyryl-cAMP (Sigma-Aldrich) to promote maturation, gliogenesis and activity]. After 7 days, cortical organoids were maintained in Media2 for as long as needed, with media changes every 3-4 days.

Neurosphere generation. The neurosphere generation protocol was published elsewhere (Nageshappa et al., 2016). Briefly, iPSC were dissociated using Accutase (Life Technologies), centrifuged and resuspended in medium (IMDM medium, 15% fetal bovine serum, 2 mM L-glutamine, 1% NEAA, 1 mM sodium pyruvate, 100 U PS, 200 μg/mL iron-saturated transferrin, 10 μM β-mercaptoethanol, 50 μg/mL ascorbic acid; supplemented with 10 μM SB (Stemgent) and 1 μM Dorso (R&D Systems) on a “low-attachment” plate for embryoid body (EB) formation. After 8 days, the EBs were plated for rosette formation and expansion of neural progenitors in the presence of defined medium DMEM/F-12 supplemented with Gem21 NeuroPlex (Gemini Bio-Products) and 20 ng/mL of FGF2. For neurosphere generation, 4,000 neural progenitors were seeded on “low-attachment” plate under rotation with no FGF2. The neurospheres were developed for around 8 weeks prior MEA plating.

Mycoplasma testing. All cellular cultures were routinely tested for mycoplasma by PCR. Media supernatants (with no antibiotics) were collected, centrifuged, and resuspended in saline buffer. Ten microliters of each sample were used for a PCR with the following primers: Forward: GGCGAATGGGTGAGTAAC; Reverse: CGGATAACGCTTGCGACCT. Only negative samples were used in the study.

Immunofluorescence staining. Cortical organoids were fixed with 4% paraformaldehyde overnight at 4 °C and then transferred to 30% sucrose. After the 3D structures sink, they were embedded in O.C.T. (Sakura, Tokyo, Japan) and sliced in a cryostat (20 µm slices). Following air dry, the slides containing the sliced samples were permeabilized/blocked with 0.1% triton X-100 and 3% FBS in PBS for 2 hours at room temperature, and incubated with primary antibodies overnight at 4 °C. Primary antibodies used in this study were: mouse anti-Nestin, Abcam (Cambridge, UK) ab22035, 1:250; rat anti-CTIP2, Abcam ab18465, 1:500; rabbit anti-SATB2, Abcam ab34735, 1:200; chicken anti-MAP2, Abcam ab5392, 1:2000; rabbit anti-Synapsin1, EMD-Millipore AB1543P, 1:500; mouse anti-NeuN, EMD-Millipore MAB377, 1:500; rabbit anti-Ki67, Abcam ab15580, 1:1000; rabbit anti-SOX2, Cell Signaling Technology 2748, 1:500; rabbit anti-GFAP, DAKO Z033429, 1:1000; rabbit anti-TBR1, Abcam ab31940, 1:500; rabbit anti-TBR2, Abcam ab23345, 1:500; rabbit anti-beta-catenin, Abcam E247, 1:200; mouse anti-GABA, Abcam ab86186, 1:200; mouse anti-GABA B Receptor 1, Abcam ab55051, 1:100; mouse anti-Parvalbumin, Millipore MAB1572, 1:500; rabbit anti-Calretinin, Abcam ab92341, 1:200; rat anti-Somatostatin, Millipore MAB354, 1:100; rabbit anti-TTF1 (NKX2.1), Abcam ab76013, 1:200. Next, the slices were washed with PBS and incubated with secondary antibodies (Alexa Fluor 488-, 555- and 647-conjugated antibodies, Life Technologies, 1:1000) for 2 hours at room temperature. The nuclei were stained using DAPI solution (1 μg/mL). The slides were mounted using ProLong Gold antifade reagent and analyzed under a fluorescence microscope

(Axio Observer Apotome, Zeiss).

Electron microscopy (EM). EM was performed at the CMM Electron Microscopy Facility at University of California San Diego. Four-month organoids were immersed in modified Karnovsky's fixative (2.5% glutaraldehyde and 2% paraformaldehyde in 0.15 M sodium cacodylate buffer, pH 7.4) for at least 4 hours, post fixed in 1% osmium tetroxide in 0.15 M cacodylate buffer for 1 hour and stained in 2% uranyl acetate for 1 hour. Samples were dehydrated in ethanol, embedded in Durcupan epoxy resin (Sigma-Aldrich), sectioned at 50 to 60 nm on a Leica Ultracut UCT (Leica, Bannockburn, IL), and transfer onto Formvar and carbon-coated copper grids. Sections were stained with 2% uranyl acetate for 5 minutes and Sato's lead stain for 1 minute. Grids were analyzed using a JEOL 1200EX II (JEOL, Peabody, MA) transmission electron microscope equipped with a Gatan digital camera (Gatan, Pleasanton, CA).

10X genomics single-cell and analysis. Cortical organoids were manually dissociated and sorted for single-cell RNA-seq analysis on the same day. Dissociated cells were first placed on ice, diluted in 2-5 ml of cell media and then treated with flavopiridol (5 μM, Sigma-Aldrich) to arrest transcriptional activity. Cells were then stained with the DNA-dyes DAPI (300 nM, Invitrogen) and DRAQ5 (2.5 μM, Thermo-Fischer) and incubated on ice for 10 minutes prior to sorting. Cells were sorted using a SH800 sorter (Sony) into 50 μL of cell media using a gating strategy that first isolated large, cell-sized particles and then sorted based on viability. Sorted cells were pelleted (3 min, 100 x g, 4 °C) and resuspended in 40 μL of fresh cell media. Cell concentration was determined and the minimum population viability threshold for downstream single cell RNA-seq processing was set at 80%.

Single cell RNA-seq libraries were constructed using the Chromium Single Cell 3' v2 Library kit (10x Genomics, (Zheng et al., 2017)) according to manufacturer descriptions; approximately 12,000 cells were loaded per sample. Reverse transcription and other amplification steps were carried out on a T100 thermal cycler (Bio-Rad). After reverse transcription, GEMs (Gel beads in emulsion) were lysed and cDNA was cleaned up with MyOne Silane Beads (Thermo

Fisher Scientific). Single stranded cDNA was PCR-amplified for 12 cycles and purified using SPRIselect Reagent Kit (Beckman Coulter). Next, cDNA was enzymatically fragmented followed by double size selection with SPRIselect Reagent Kit (B23317, Beckman Coulter). Subsequently, adaptors were ligated and libraries were constructed by PCR. Another round of double size selection was performed using SPRIselect Reagent Kit to generate final libraries with a size of 200-700bp. Final libraries were quantified using Qubit dsDNA HS Assay Kit (Thermo Fisher Scientific) and size distribution was measured using Tapestation (High Sensitivity D1000, Agilent). Average fragment size of successful libraries was 500 bp. The libraries were loaded at a concentration of 13 pM and sequenced on a Hiseq 4000 sequencer (Illumina) with the following parameters (Read1 26 cycles; Index 1 8 cycles; Read 2 98 cycles).

Raw sequencing data from 1, 3, 6, 10-month organoids were preprocessed with Cell Ranger software (version 2.1.1, 10X Genomics, Pleasanton). Reads were aligned to hg38 human reference genome (Zerbino et al., 2018) and the feature-barcode matrix was generated. The secondary analysis performed on the feature-barcode matrix was processed via the Seurat v2.0 package (Butler et al., 2018). For the analysis of individual time points, all genes that were not detected in at least 5 cells and cells with less than 200 genes detected were discarded. The additional filtering was based on gene-UMI distribution and percentage of mitochondrial reads. The filtered matrix was log-normalized and scaled to 10,000 transcripts per cell. Variable genes across the single cells were identified with the FindVariableGenes function and unwanted sources of variation, such as UMI counts per cell, percent of mitochondrial reads, were regressed out with the ScaleData function. Dimension reduction of the pre-processed matrix was performed by principal component analysis (PCA). The number of principal components was identified based on a strong enrichment of genes with low p-values, which were computed by a resampling test. This procedure was implemented with the JackStraw function in Seurat. With the selected dimensions, cellular distance matrix was first organized into a K-nearest neighbor (KNN) graph and then partitioned into clusters with Louvain algorithm via the FindClusters function. Finally, cells within the graph-based clusters were co-localized on the UMAP plot (McInnes L, 2018) of two dimensions by the RunUMAP function. Identifying top differentially expressed genes for each cluster was performed using the FindAllMarkers function.

Datasets from the four time points were merged with the MergeSeurat function and then the merged matrix was used as an input to the Seurat v3 anchoring procedure, which assembles datasets into an integrated reference by identifying cell pairwise correspondences for single cells across different datasets. Further analysis was processed with Seurat v3.0 package (Stuart et al., ????). Default parameters including a dimensionality of 30 were set to run the FindIntegrationAnchors and IntegrateData function. On the integrated datasets, clustering was performed with a resolution parameter set to be 1.0 and a dimensionality of 30 by FindNeighbors and FindClusters. With the graph-based clustering, a total of 14 clusters were generated, which were further merged into seven main clusters based on expression of marker genes. UMAP plots displayed by the DimPlot function were used to visualize and explore the integrated datasets. Dot plots and UMAP plots for transcript abundance of marker genes were made using ggplot2 package (Wickham, 2016), while the barplot was created with graphics v3.5.3 package (Murrell, 2005). The dot plots show the percentage of cells that express more than one transcript for each gene and its log-normalized expression level across main cell clusters. Violin plots for marker gene expression across all clusters were produced with the VlnPlot function.

Mass spectrometry. Samples were assayed using an adaptation of published protocol (Gertsman et al., 2014). Cortical organoid media (100 μL) was mixed with 2 μM 13C4-4-aminobutyric acid, as internal standard. Metabolites were extracted using 80% ice-cold methanol. After incubation for 30 min at -20 °C, samples were deproteinized at 4 °C by centrifugation at 17,136 x g for 10 minutes. Supernatants were evaporated to dryness in a centrifugal evaporator at 36 °C (Savant SPD121P Speed-Vac concentrator. Thermo Fisher, Asheville, NC) and reconstituted in 100 μL of 10% methanol in water + 0.1% formic acid, by means of consecutive vortexing, orbital shaking and sonication. 5 μL of which were injected into a Sciex 4500 triple quadrupole mass spectrometer (Sciex, Foster City, California, USA) to determine 4-aminobutyric acid (GABA) concentration. Chromatographic separations were conducted a 3 μm ACE C18-PFP reversed-phase HPLC column (Mac-mod analytical, Chadds Ford, PA, USA) using an Acquity binary pump (Waters, Milford, MA, USA) equipped with an in-line degasser at 0.3 mL/min flow-rate and at 13 °C, to enhance the retention of the low-retained compounds, by means of a simple binary gradient of acetonitrile partitioning in 3% acetonitrile in water, both containing 0.1% formic acid. Compounds were eluted during the first 3 minutes, then it ramped to 100%. Total run time was 45 minutes. Positive electrospray ionization multiple reaction monitoring transitions were optimized for GABA (and 13C4-GABA), m/z 104.2>87 (108.2>90.9) and m/z 104.2>68.9 (108.2>73), using collision energies of 15 and 23, respectively, and unit mass resolution. GABA concentrations were calculated by interpolation using an 8-point calibration curve, spanning 0.01 to 0.2 μM, constructed by supplementing medium with the appropriate amounts of GABA. Quantification was conducted using MultiQuant 2.1 software (Sciex, Foster City, CA, USA).

Whole-cell patch-clamp. Whole-cell patch-clamp recordings were performed from cells of cortical organoids in a similar condition as for MEA recordings: 6- to 8-week cortical organoids were plated on 35 mm dishes that were previously coated with 100 μg/mL poly-L-ornithine and 10 μg/ml laminin. Cells were fed twice a week and have been maintained for 24 weeks. The extracellular solution for patch-clamp experiments contained (in mM) the following: 130 NaCl, 3 KCl, 1 CaCl2, 1 MgCl2, 10 HEPES, and 10 glucose; pH 7.4 with 1 M NaOH ($\sim$4 mM Na+ added). The internal solution for patch electrodes contained (in mM) the following: 138 K-gluconate, 4 KCl, 10 Na2-phosphocreatine, 0.2 CaCl2, 10 HEPES (Na+ salt), 1 EGTA, 4Mg-ATP, 0.3 Na-GTP; pH 7.4 with 1 M KOH ($\sim$3 mM K+ added). The osmolarity of all solutions was adjusted to 290mOsm. Electrodes for electrophysiological recording were pulled on a Flaming/Brown micropipette puller (Model P-87, Sutter Instrument, CA, USA) from filamented borosilicate capillary glass (1.2 mm OD, 0.69 mm ID, World Precision Instruments, FL, USA). The electrode resistances were 3–8 MΩ. Patch-clamp experiments were performed with an

Axon CV-4 headstage and Axopatch 200A amplifier (Molecular Devices, CA, USA) at room temperature. Liquid junction potential correction ($\sim$10 mV) was not applied. Electrophysiology data were analyzed offline using pCLAMP 10 software (Molecular Devices, CA, USA).

Multi-electrode array (MEA) recording. Two to three 6-week cortical organoids were plated per well in 12-well MEA plates (Axion Biosystems, Atlanta, GA, USA). Each well contains 64 low-impedance (0.04 MΩ) platinum microelectrodes with 30 μm of diameter spaced by 200 μm, yielding a total of 512 channels (8 wells containing organoids and 4 internal control). The plate was previously coated with 100 μg/mL poly-L-ornithine and 10 μg/mL laminin, and we performed four independent experiments in duplicates. Cells were fed twice a week and measurements were collected 24 hours after the medium was changed, once a week, starting at two weeks after plating (8 weeks of organoid differentiation). Recordings were performed using a Maestro MEA system and AxIS Software Spontaneous Neural Configuration (Axion Biosystems) with a customized script for band-pass filter (0.1-Hz and 5-kHz cutoff frequencies). Spikes were detected with AxIS software using an adaptive threshold crossing set to 5.5 times the standard deviation of the estimated noise for each electrode (channel). The plate was first allowed to rest for three minutes in the Maestro device, and then four minutes of data were recorded. For the MEA analysis, the electrodes that detected at least 5 spikes/min were classified as active electrodes using Axion Biosystems' Neural Metrics Tool. Bursts were identified in the data recorded from each individual electrode using an inter-spike interval (ISI) threshold requiring a minimum number of 5 spikes with a maximum ISI of 100 ms. A minimum of 10 spikes under the same ISI with a minimum of 25% active electrodes were required for network bursts in the well. The synchrony index was calculated using a cross-correlogram synchrony window of 20 ms. Bright-field images were captured to assess for cell density and electrode coverage.

Custom MEA analysis. Custom MEA analysis and developmental time regression model can be found in: https://github.com/voytekresearch/OscillatoryOrganoids. Raw MEA recordings were converted to .mat files using Axion-provided functions and analyzed offline using custom

MATLAB functions and scripts. Local field potential signals (LFP) from each of the 64 electrodes were generated by low-pass filtering (FIR filter) and downsampling raw signals from 12,500 Hz to 1,000 Hz (resample.m). Multi-unit spikes were detected as follows: each channel was first referenced to the well median for every time point, similar to a common average reference (64 channels). The median was used instead of the mean to avoid biasing the reference during high firing rate periods. Next, the re-referenced signal was bandpass filtered for 300-3,000 Hz with a 3rd-order Butterworth filter (butter.m). The adaptative spike threshold was set to be 5.5 standard deviations, where the standard deviation was estimated from the median as previously described (Quiroga et al., 2005) to avoid biasing the threshold for channels with high firing rates (thus an artificially high threshold). Spike timestamps were taken as the peak time after the absolute value of the signal crossed the threshold, but at least 1 ms from another spike (findpeaks.m). Spike timestamps were then converted into binary vectors (1 ms bin size), summed across 64 channels, and smoothed (conv.m) with a normalized 100-point (0.1 s) Gaussian window (gausswin.m) to create a population spiking vector for each MEA well. Note that spikes from each channel do not represent putative single-unit action potentials, as the spatial resolution of MEA electrodes were too sparse. Multi-unit spiking was not sorted since total population spiking (of well) was submitted for further analysis, rather than individual spike trains.

Network event analysis. A network event was detected when population spiking was i) greater than 80% of the maximum spiking value over the length of the recording; ii) at least 1 spike/s; and iii) 1 second away from any other network events. The first peak after all 3 criteria was satisfied was marked as t = 0, and the window of data from 0.5 s before to 2.5 s after the peak was collected as the network event, as events almost always subsided 2.5 seconds after onset by both algorithmic detection and visual inspection. Nearly all spiking channels experienced a significant firing rate increase during network events. LFP data from all 64 channels from the same timeframe were also collected for analysis. All events from different MEA wells obtained on the same recording day were aggregated for statistical analysis and plotting. Subpeaks within an event were identified using findpeaks.m, where a subpeak must satisfy the following: i) peak height of at least 25% of the first peak; ii) peak width of at least 50 ms; iii) at least 200 ms away from the previous peak; and iv) peak prominence of 1 over Peak 1 height. Subpeak time and the height relative to the initial peak were recorded. The inter-event interval coefficient of variation (IEI CV) was calculated as the standard deviation of the inter-event interval divided by its mean, where IEI is the time between consecutive network events within the same MEA well. Event temporal correlation was calculated as the mean Pearson correlation coefficient of population spiking vector between each pair of network event in the same MEA well across a single recording session. Event spatial correlation was calculated as the mean Pearson correlation coefficient between all pairs of 64 LFP channels during each 3-s network event.

Oscillatory spectral power analysis. Power spectral density (PSD) estimates were computed using Welch's method (pwelch.m), with a window length of 2 s and overlap of 1 s. Oscillatory power was defined as peaks in the PSD above the aperiodic 1/f power law decay. Thus, for each channel, a straight line was fit over the PSD in double-log space between 0.5-20 Hz using robust fit (robustfit.m), and oscillatory power was computed as the difference between the mean log PSD power and the mean log fitted power (baseline), over 2.5-4.5 Hz. This method accounts for non-oscillatory changes, such as slow transients or the aperiodic 1/f background component, whereas standard wavelet filtering methods will confound the two (Donoghue et al., 2020).

Phase Amplitude Coupling (PAC). LFP data from all 64 channels of each well was first lowpass/bandpass filtered (eegfilt.m, EEGLAB) for delta (0-4 Hz) and high-frequency, broadband (100-400 Hz) activity, sometimes referred to as high gamma. Delta phase was extracted by taking the phase angle of the bandpassed delta signal Hilbert transform (hilbert.m, angle.m), while gamma power was extracted by taking the squared magnitude of the filtered gamma. Gamma power was smoothed with the same delta-band filter for display purposes, but not for subsequent analysis. Note that analysis was performed for 100-200 Hz and 200-400 Hz separately, as LFP spectrum follows an inverse power law (1/f), and grouping a wide frequency band (100-400 Hz) together would bias power estimates towards lower frequency limits (100 Hz). To compute PAC, instantaneous delta phase was binned into 20 equidistant bins between -π and π, and gamma power was sorted based on the corresponding delta phase at the same sample time and averaged across the same phase bin. This procedure was performed separately for event and non-event indices, where event indices are the same 3-second windows as described above in Network Event Analysis, while all other times are considered as non-event time points. Modulation Index was computed as the Kullback-Leibler divergence between the sum-normalized distribution of gamma power across phase bins and a uniform distribution (Tort et al., 2010). Figure 1.3C presents well-averaged MI across all 64 channels. For visualization in Figure 1.3B, the binned gamma power vector for each channel was circularly shifted such that the phase of maximum gamma power was -π.

Pharmacology. The pharmacological manipulation was performed using cortical organoid plated on 4 MEA wells (n = 4, cortical organoid culture) the following drugs: 10 μM bicuculline, 100 μM picrotoxin, 50 μM muscimol, 20 μM CNQX, 20 μM AP5, 25 μM baclofen and 1 μM TTX. In this assessment, baseline recordings were obtained immediately before and 15 minutes after the addition of the compound. Three washes with PBS for total removal of the drug were performed in washout experiments; fresh media was added and another recording was conducted after 2 hours.

Preterm neonatal EEG. A preterm neonatal EEG dataset was obtained from a publicly available dataset (Stevenson et al., 2017). Raw recordings were not available due to patient confidentiality concerns. The dataset includes 567 recordings from 39 preterm neonates (24-38 weeks PMA), consisting of 23 EEG features computed from the entirety of each recording (Table 1.2). See cited publication for details of features. Briefly, we chose to include features derived from duration and timing of (interval between subsequent) network events in neonates and organoids, as these are least affected by anatomical differences between the two model systems (i.e., skull filtering), as well as spectral features (delta, theta, and alpha power). 5%/50%/95% refer to percentile of the feature distribution from a recording.

Resampled feature-age correlation. We computed Pearson's correlation coefficient between neonate age and each of the 12 EEG features, after a leave-K-groups-out resampling procedure N times, where K is the number of neonates from whom all recordings were left out in computing the correlation (50% of all neonates, resampling N = 100). An identical procedure was performed to compute the correlation between organoid culture development time and LFP features (K = 4 out of 8, 50%, N = 100). Mean and standard deviation were then computed over all resampled draws in order to compare between organoid LFP and neonatal EEG to produce Figure 1.4C and Figure 1.8D.

Neonate-organoid development time regression model. To compare the similarity of developmental trajectory of cortical organoids and the preterm human brain, we trained an Elastic Net (L1- and L2- regularized) regression model on only the preterm neonatal EEG features and used that model (with all parameters held the same) to predict an equivalent organoid development time for each recording time point over 40 weeks in culture. Specifically, the training dataset consisted of a subset of the preterm EEG data; we discarded all "low-activity-period" features (Lisman, 1997) since there was no equivalent period for organoid recordings, as well as features for which we could not sensibly compute from organoid LFPs, such as interhemispheric synchrony. This selection was done a priori, and 12 features remained, including 3 features for relative spectral power in distinct frequency bands. The features corresponding to aspects of spontaneous activity transient (SAT) timing, such as SATs per hour and SAT duration, were similarly computed on organoid LFPs after network event detection described earlier (see Table 1.2 for a full list of included and rejected features). This latter organoid LFP test dataset was never seen by the regression model until prediction time. Training was performed using scikit-learn linear model module [ElasticNetCV (Pedregosa et al., 2011)], with K-Group shuffle split cross-validation on regularization hyperparameters, where K = 25% of groups, N = 200 shuffles. In other words, we found the best regularized linear model possible for predicting the age of preterm neonates using those precomputed EEG features. This model was directly applied on organoid LFP features to determine the corresponding development time of the organoids during 40 weeks in culture. Control datasets were also submitted for prediction, including held-out preterm EEG (positive control), and mouse primary culture, 2D iPSC culture, and human fetal culture (negative controls). To quantify the model's ability to predict the developmental trend of the out of sample datasets, we compute the Pearson correlation coefficient between the predicted and actual age of each dataset. To eliminate the potential confound of a difference in frequency-dependent filtering properties of the skull and difference in spatial integration of currents in macroscopic EEG electrodes compared to microscopic planar MEA electrodes, the same analysis was performed after discarding the spectral features (leaving 9 features total). This result is presented in Figure 1.8E, in addition to the prediction for the control datasets.

Quantification and statistical analysis

Statistical analysis. Data are presented as mean ± s.e.m., unless otherwise indicated, and it was obtained from different samples. No statistical method was used to predetermine the sample size. The statistical analyses were performed using Prism software (GraphPad, San Diego, CA, USA). Student's t-test, Mann–Whitney-test, or ANOVA with post hoc tests were used as indicated. Significance was defined as $P < 0.05$(*), $P < 0.01$(**), or $P < 0.001$(***).

Statistics and Regression for custom MEA analysis. To fit linear or quadratic models in Figure 1.2F, G, I, we used organoid developmental time (in days) as input and electrophysiological features as output (LinearModel.fit, MATLAB). Reported R2 and p values are model statistics over the entire dataset. All events from different MEA wells on the same recording day were aggregated as samples drawn from the same distribution.

Data and code availability

Single-cell RNA sequencing data. All datasets and/or analyses generated during the current study are available from the corresponding author upon reasonable request. Single-cell RNA sequencing data that support the findings of this study have been deposited at NCBI GEO: GSE130238.

Acknowledgements

Chapter 1, in full, is a reprint of the material as it appears in the following manuscript published in *Cell Stem Cell*: Trujillo*, C. A., Gao*, R., Negraes*, P. D., Gu, J., Buchanan, J., Preissl, S., Wang, A., Wu, W., Haddad, G. G., Chaim, I. A., Domissy, A., Vandenberghe, M., Devor, A., Yeo, G. W., Voytek, B., & Muotri, A. R. (2019). **Complex oscillatory waves emerging from cortical organoids model early human brain network development.** The dissertation author was one of the primary investigators and co-first authors of this paper.

1.5 Supplemental Figures & Tables

Figure 1.5: Figure S1. Cellular and molecular characterization of human cortical organoids. Related to Figure 1.1. (A) Organoids are composed of a proliferative region surrounded by intermediate progenitor cells, cortical neurons. Scale bar, 50 μm. (B) UMAP plots highlighting time point specific cells. (C) UMAP plots for individual time point showing cell-type specific marker expression levels (D) Violin plots of marker gene expression across all clusters. (E) Sub-cluster analysis of GAD2 population from 10-month cortical organoids. (F) GABAergic neuronal markers expression of 10-month cortical organoids. (G) Detection of GABA neurotransmitter in the culture media using mass spectrometry. The average GABA concentration in the media was 0.028 ± 0.014 μM.

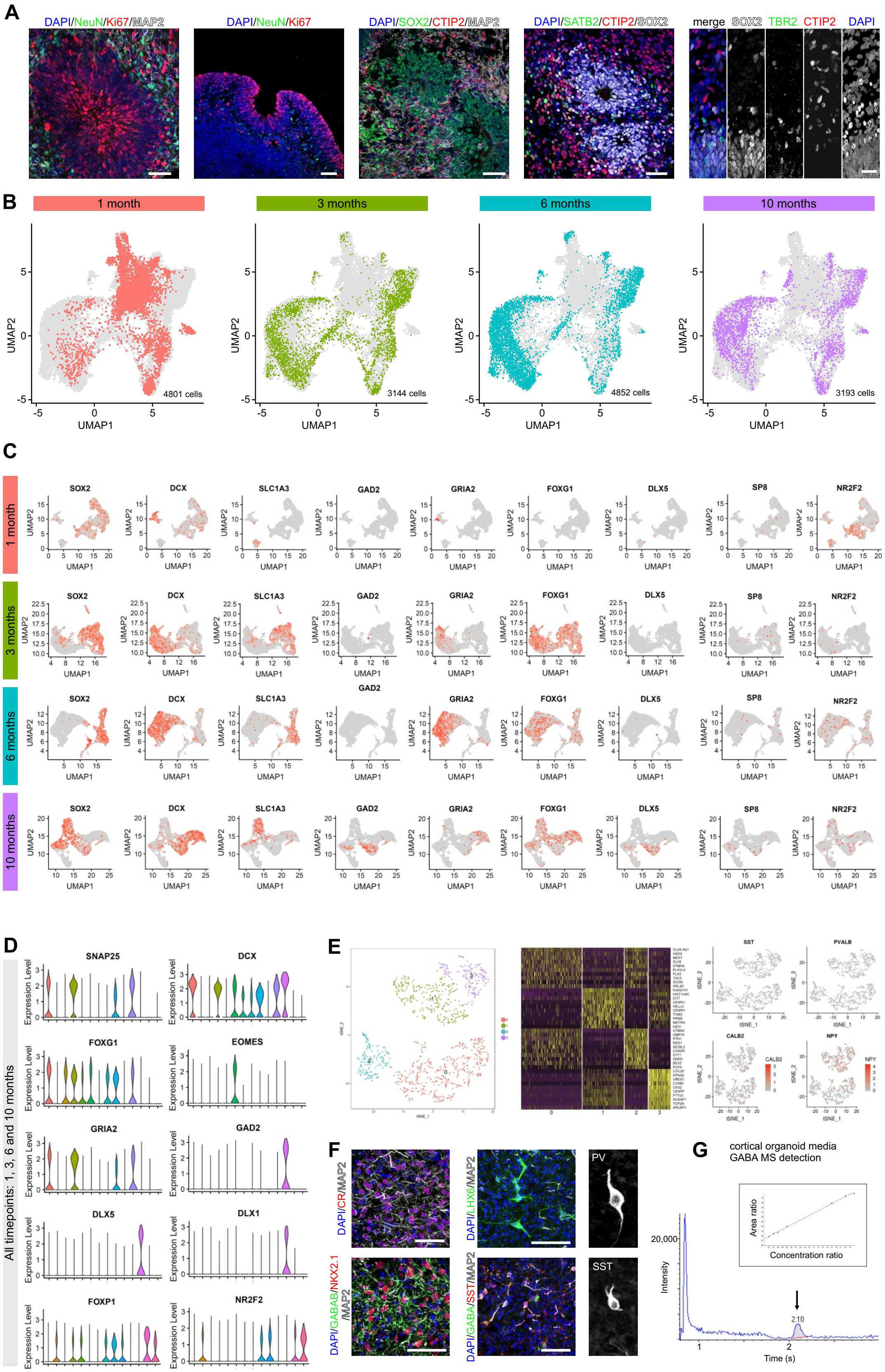
A
DAPI/NeuN/Ki67/MAP2
DAPI/NeuN/Ki67
DAPI/SOX2/CTIP2/MAP2
DAPI/SATB2/CTIP2/SOX2
merge SOX2 TBR2 CTIP2 DAPI
B
1 month
3 months
6 months
10 months
UMAP2
UMAP1
4801 cells
3144 cells
4852 cells
3193 cells
C
SOX2
DCX
SLC1A3
GAD2
GRIA2
FOXG1
DLX5
SP8
NR2F2
D
All timepoints: 1, 3, 6 and 10 months
SNAP25
DCX
FOXG1
EOMES
GRIA2
GAD2
DLX5
DLX1
FOXP1
NR2F2
Expression Level
E
tSNE_1
tSNE_2
SST
PVALB
CALB2
NPY
F
DAPI/CR/MAP2
DAPI/LHX6/MAP2
PV
DAPI/GABAB/NKX2.1/MAP2
DAPI/GABA/SST/MAP2
SST
G
cortical organoid media
GABA MS detection
Area ratio
Concentration ratio
Intensity
20,000
2.10
Time (s)
1
2

Figure 1.6: Figure S2. Long-term cortical organoid network activity. Related to Figure 1.2. (A) Electrophysiological characteristics of 6-month human iPSC-derived cortical organoids. Whole-cell current-clamp recording of a representative neuron from 6-month cortical organoids showing repetitive action potential firing in response to 50 pA current injection from a resting membrane potential of -63 mV. Application of 1 μM TTX abolished the firing (lower panel). (B) Whole-cell voltage-clamp recording in the same neuron showing voltage-gated K+ current and TTX-sensitive Na+ current, elicited from a holding potential of -80mV to the indicated voltages. (C) Plot of the peak current sizes of K+ channels and Na+ channels as a function of voltage determined from neurons of 6-month cortical organoids (peak INa size = -1466.86 ± 575.18 pA. Peak IK size = 3031.79 ± 1405.19 pA. n = 6 neurons). (D) Voltage-clamp recording at -60 mV exhibiting spontaneous excitatory postsynaptic currents (sEPSCs) in another representative neuron (frequency of sEPSCs = 0.25 ± 0.10 Hz; n = 5 neurons. Amplitude of sEPSCs = -19.92 ± 5.90 pA; n = 5 neurons; we observed sEPSCs in 84% of the tested neurons). Application of NBQX and AP5 fully inhibited the sEPCS. (E) Representative traces showing that a human iPSC-derived neuron displays spontaneous AP firing (AP firing frequency = 13.67 ± 1.11 Hz; n = 6 neurons). The data are shown as mean ± s.e.m. (F) Representative activity heatmap and bright-field image of cortical organoids on the MEA plate. (G) Schematic representation of the electrical activity features analyzed from the MEA recordings. Each bar represents a spike; and a spike cluster (in blue) represents a burst. Bursts occurring at the same time in different channels characterize a network burst. The synchrony index is based on the cross-correlogram and represents a measure of similarity between two spike trains. (H) Temporal evolution of network activity characterized by different parameters. (I) Raster plots illustrating the development of network activity. (J) Consistent and reproducible development of electrical activity in cortical organoids over time. The data are shown as mean ± s.e.m (n = 8, independent experiments performed in duplicates using two clones of an iPSC line).

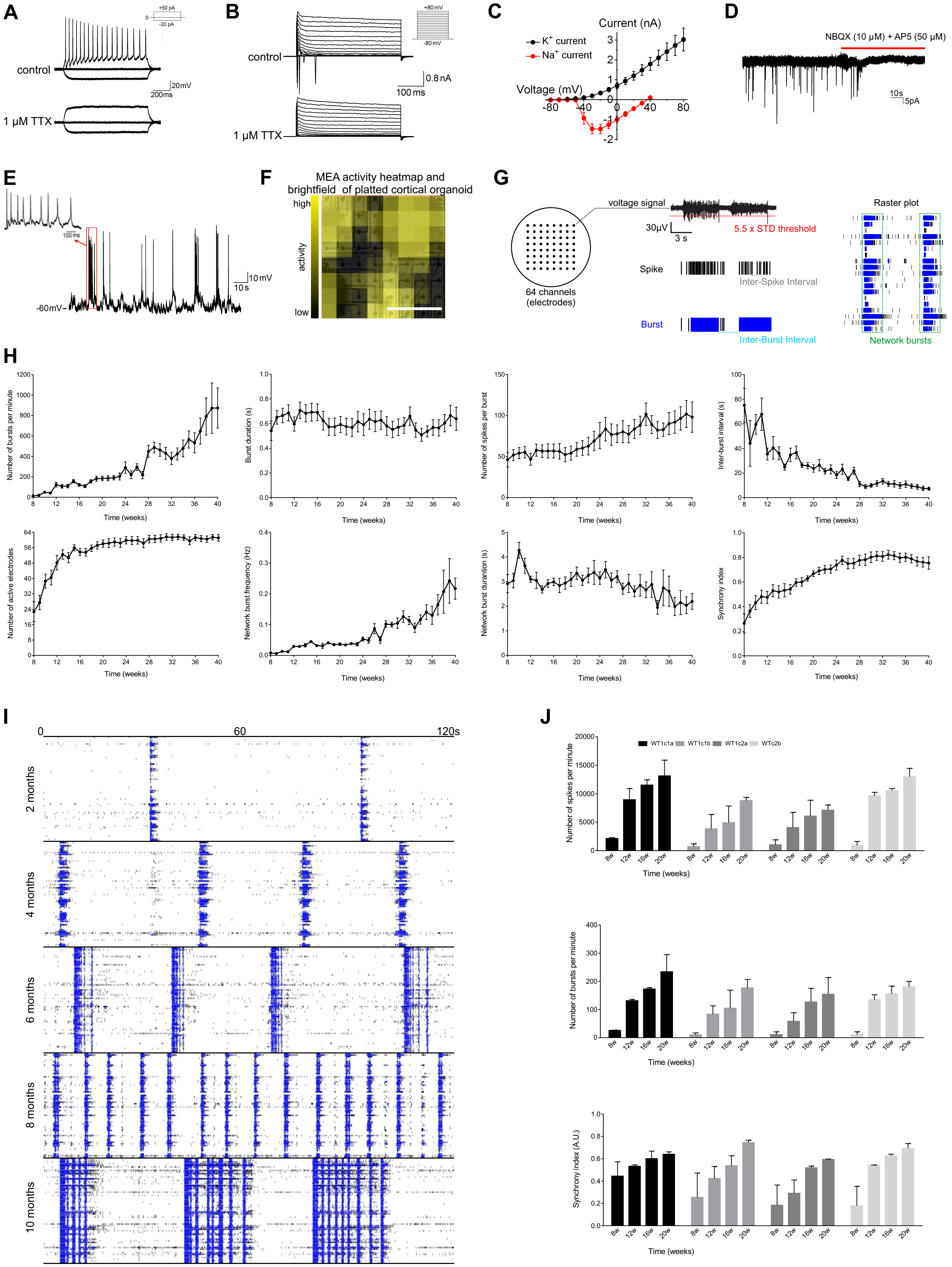
A
+50 pA
0
-20 pA
control
20mV
200ms
1 µM TTX
B
+80 mV
-80 mV
control
0.8 nA
100 ms
1 µM TTX
C
Current (nA)
K+ current
Na+ current
Voltage (mV)
-80
-40
0
40
80
3
2
1
0
-1
-2
D
NBQX (10 µM) + AP5 (50 µM)
10s
5pA
E
100 ms
10 mV
10 s
-60mV
F
MEA activity heatmap and brightfield of platted cortical organoid
high
activity
low
G
voltage signal
30µV
3 s
5.5 x STD threshold
64 channels (electrodes)
Spike
Inter-Spike Interval
Burst
Inter-Burst Interval
Raster plot
Network bursts
H
Number of bursts per minute
Burst duration (s)
Number of spikes per burst
Inter-burst interval (s)
Number of active electrodes
Network burst frequency (Hz)
Network burst duration (s)
Synchrony index
Time (weeks)
8
12
16
20
24
28
32
36
40
I
0
60
120s
2 months
4 months
6 months
8 months
10 months
J
WT1c1a
WT1c1b
WT1c2a
WTc2b
Number of spikes per minute
Number of bursts per minute
Synchrony index (A.U.)
8w
12w
16w
20w
Time (weeks)

Figure 1.7: Figure S3. Extended characterization of cortical organoid network electrophysiology. Related to Figure 1.2. (A) Spikes detected on 9 channels. Black traces represent single spikes, blue and red traces represent the average of positive and negative spikes, respectively. Spike trains are not sorted for their polarity in the subsequent analyses, as total population spiking is the main feature of interest. (B) Representative oscillatory network events. Each overlapping trace represents a single occurrence of an event recorded on the same channel. LFP polarity of events differs between channels due to the spatial configuration of cells around the electrode. (C) Event onset peak (Peak 1) increases in amplitude until 30 weeks, while (D) subpeak amplitude continues to increase (for the 2nd-4th peak) throughout development. (E) Subsequent peaks occur with a consistent latency of 400 ms after the previous peak, particularly for Peak 3 and 4. (F) Temporal similarity of network events during the 3-s window is high at early time points, but decreases with development, acquiring more variable dynamics within an event. The data showed in C and F are presented as mean ± s.e.m., linear (C, F) model regression. (G) Comparison of the protocol for neurosphere and cortical organoid generation. (H) Network-wide giant depolarizing potentials occur in neurosphere at a similar rate to those found in organoids recordings, and visible perturbations are observed in the LFP trace. However, the network recruitment in neurospheres is lower with significantly shorter events. Coherent low-frequency depolarizations are observed in filtered LFP events, but with much lower amplitude when scaled to the same range as those recorded from organoids (I, J).

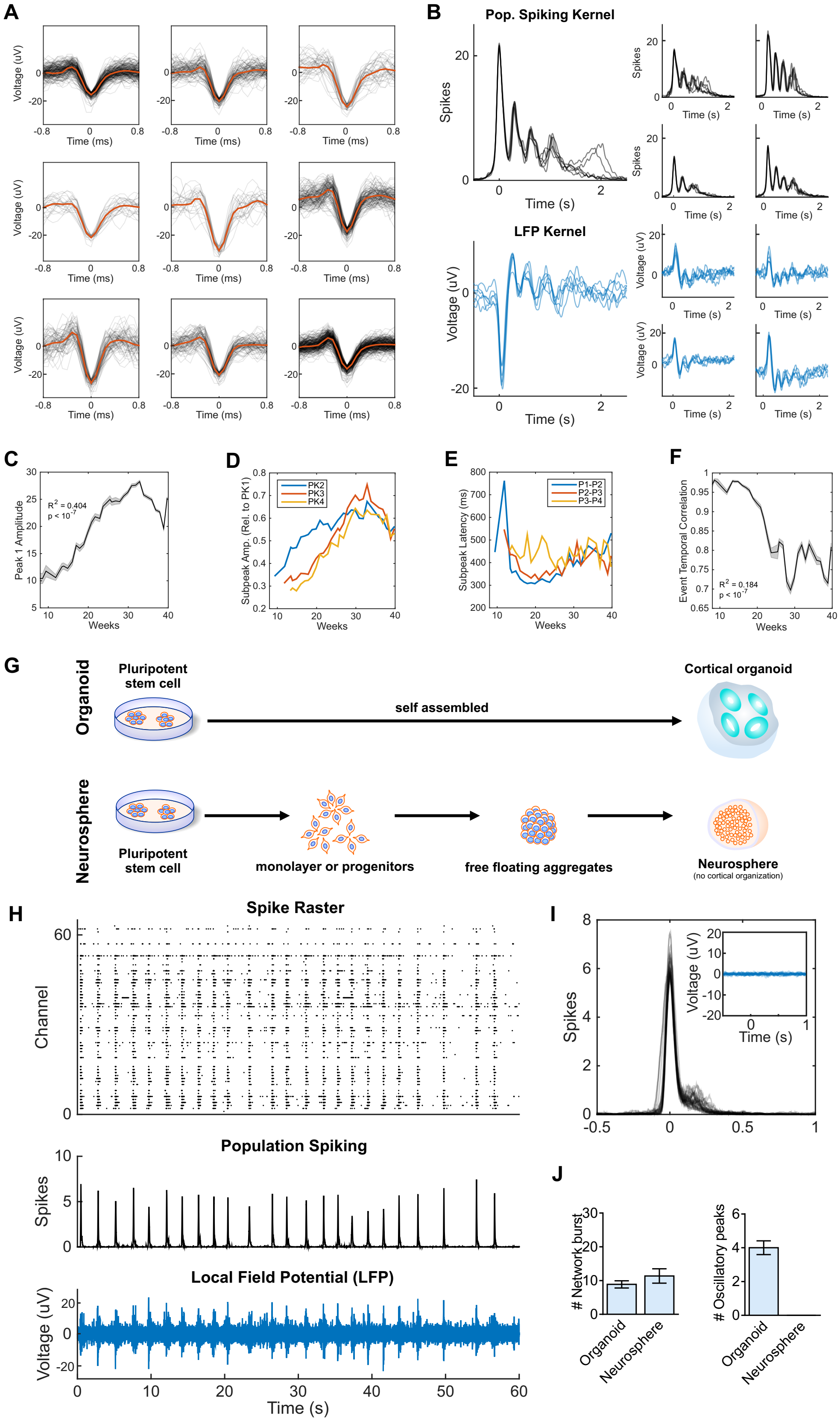
A
Voltage (uV)
Time (ms)
-0.8
0
0.8
0
-20
B
Pop. Spiking Kernel
Spikes
Time (s)
20
LFP Kernel
Voltage (uV)
-20
2
C
Peak 1 Amplitude
$R^2 = 0.404$
$p < 10^{-7}$
Weeks
D
Subpeak Amp. (Rel. to PK1)
PK2
PK3
PK4
E
Subpeak Latency (ms)
P1-P2
P2-P3
P3-P4
F
Event Temporal Correlation
$R^2 = 0.184$
$p < 10^{-7}$
G
Organoid
Pluripotent stem cell
self assembled
Cortical organoid
Neurosphere
Pluripotent stem cell
monolayer or progenitors
free floating aggregates
Neurosphere
(no cortical organization)
H
Spike Raster
Channel
60
Population Spiking
Spikes
Local Field Potential (LFP)
Voltage (uV)
Time (s)
I
Spikes
Voltage (uV)
Time (s)
J
Network burst
Oscillatory peaks
Organoid
Neurosphere

Figure 1.8: Figure S4. Network activity in cortical organoids and oscillatory features in the developing human brain. Related to Figure 1.4. (A, B) Time-frequency and spectral representation of time series data from a 6-month cortical organoid, demonstrating oscillatory phenomenon. Spectrogram (A) of organoid LFP shows bursts of activity localized at low frequencies, as well as 100Hz and beyond, while power spectral density (PSD, B) displays canonical 1/f power law decay and a narrow oscillatory peak at 3 Hz. (C) Comparison of preterm neonate EEG and cortical organoid features over time. For included EEG features, see Table 1.2. (D) Distributions of resampled Pearson correlation coefficients between feature and age for preterm neonate and organoid. (E) Model-predicted developmental time (y-axis, age in weeks) follows actual weeks-in-culture (x-axis) for organoids (orange and blue), as well as true age of held-out preterm neonate data points (black), excluding spectral features. Dashed line represents unity, signifying perfect prediction. Large circles on solid lines and shaded regions denote mean ± std of prediction, respectively, while dots indicate per-sample prediction (n = 8 for organoids at all time points). The unnormalized feature weights are: Constant: 53.93093; SATs per hour: 0.05791; RMS SAT duration: 0.17439; SAT duration (50%): 0.46857; SAT duration (5%): -1.59115; SAT duration (95%): -0.17140; RMS Inter-SAT Duration: 1.01745; Inter-SAT duration (50%): -1.67926; Inter-SAT duration (5%): 0.00000; Inter-SAT duration (95%): -0.24631; Relative Delta Power: -31.94628; Relative Theta Power: -39.72896; and Relative Alpha Power: 30.92235.

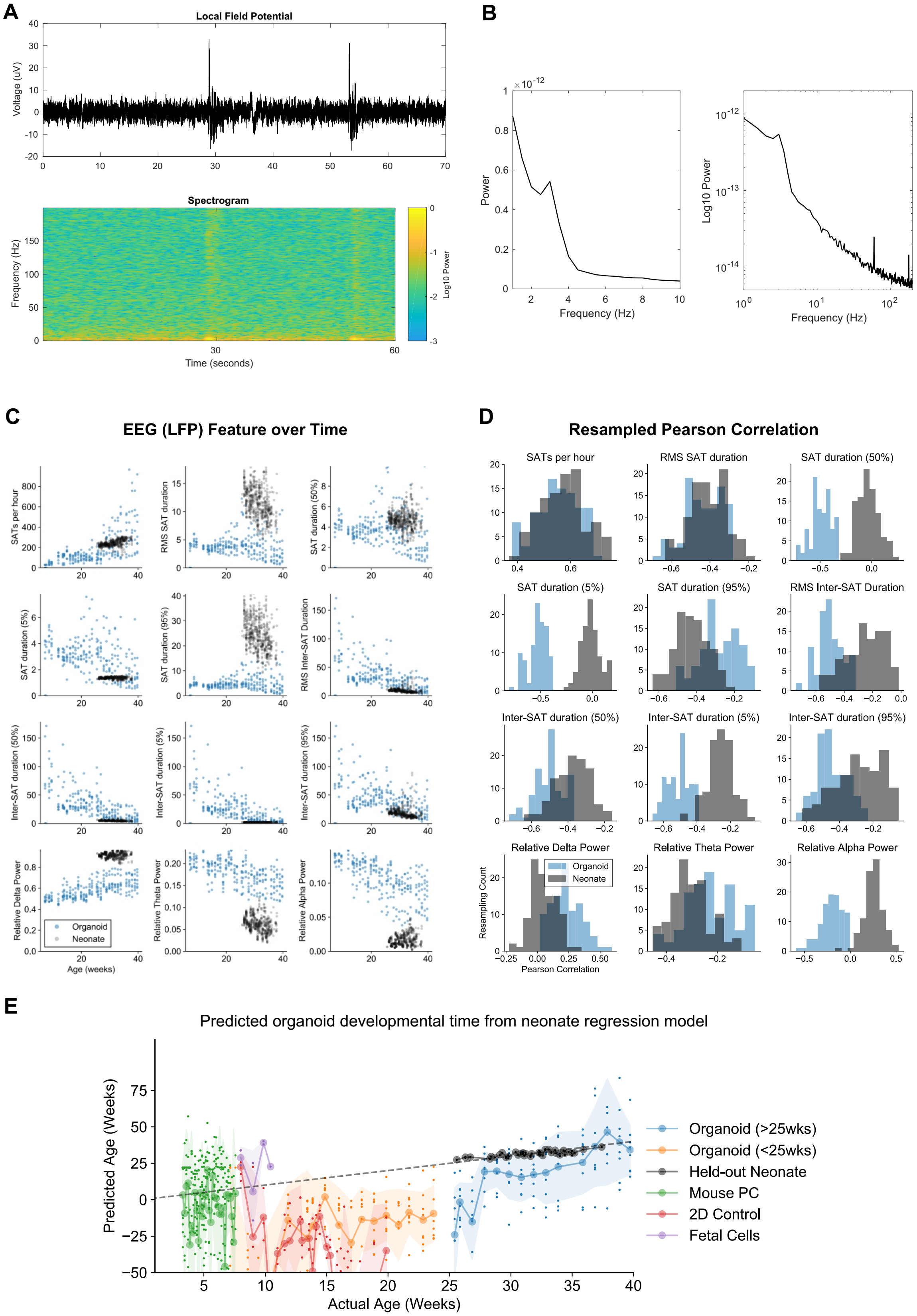
A
Local Field Potential
Voltage (uV)
Spectrogram
Frequency (Hz)
Time (seconds)
Log10 Power
B
Power
Frequency (Hz)
Log10 Power
Frequency (Hz)
C
EEG (LFP) Feature over Time
SATs per hour
RMS SAT duration
SAT duration (50%)
SAT duration (5%)
SAT duration (95%)
RMS Inter-SAT Duration
Inter-SAT duration (50%)
Inter-SAT duration (5%)
Inter-SAT duration (95%)
Relative Delta Power
Relative Theta Power
Relative Alpha Power
Organoid
Neonate
Age (weeks)
D
Resampled Pearson Correlation
SATs per hour
RMS SAT duration
SAT duration (50%)
SAT duration (5%)
SAT duration (95%)
RMS Inter-SAT Duration
Inter-SAT duration (50%)
Inter-SAT duration (5%)
Inter-SAT duration (95%)
Relative Delta Power
Relative Theta Power
Relative Alpha Power
Organoid
Neonate
Resampling Count
Pearson Correlation
E
Predicted organoid developmental time from neonate regression model
Predicted Age (Weeks)
Actual Age (Weeks)
Organoid (>25wks)
Organoid (<25wks)
Held-out Neonate
Mouse PC
2D Control
Fetal Cells

Table 1.1: Supplemental Table 1. Top expressed genes of each cell cluster. Related to Figure 1.1.

cluster	**gene**	**avg_logFC**	**pct.1**	**pct.2**	**p_val_adj**
GABAergic Neurons	DLX5	1.17944	0.403	0.362	0.47966
GABAergic Neurons	DLX6-AS1	0.97634	0.75	0.396	5.59E-81
GABAergic Neurons	SEZ6L2	0.96254	0.945	0.713	2.58E-22
GABAergic Neurons	SYT1	0.91593	0.947	0.814	2.55E-20
GABAergic Neurons	CHCHD2	0.84772	0.468	0.45	0.01172
GABAergic Neurons	HMP19	0.84097	0.734	0.755	0.17341
GABAergic Neurons	ARL4D	0.82671	0.413	0.485	1
GABAergic Neurons	INSM1	0.82003	0.813	0.444	2.87E-57
GABAergic Neurons	DLX2	0.81130	0.361	0.336	2.48E-06
GABAergic Neurons	SCG3	0.78232	0.761	0.732	0.03532
GABAergic Neurons	RTN3	0.78167	0.958	0.907	1.17E-12
GABAergic Neurons	NSG1	0.76102	0.876	0.742	3.63E-08
GABAergic Neurons	DCX	0.75629	0.782	0.736	1.97E-27
GABAergic Neurons	TERF2IP	0.74991	0.95	0.851	4.66E-28
GABAergic Neurons	PAFAH1B3	0.74128	0.937	0.853	9.39E-21
GABAergic Neurons	YWHAQ	0.74116	0.971	0.921	2.55E-53
GABAergic Neurons	DAAM1	0.73920	0.913	0.765	5.32E-10
GABAergic Neurons	TAGLN3	0.72672	0.905	0.774	6.58E-05
GABAergic Neurons	TTC3	0.71927	0.976	0.909	8.55E-16
GABAergic Neurons	STMN2	0.69866	0.905	0.892	8.26E-52
GABAergic Neurons	TAC3	0.69627	0.342	0.404	1.99E-12
GABAergic Neurons	CD24	0.67659	0.95	0.808	6.11E-12
GABAergic Neurons	TXNIP	0.67286	0.939	0.832	1.04E-05
GABAergic Neurons	STMN4	0.66186	0.934	0.885	0.04858
GABAergic Neurons	NREP	0.64996	0.918	0.802	0.00264
GABAergic Neurons	RAB3A	0.63717	0.937	0.771	1.01E-12
GABAergic Neurons	SCGN	0.63426	0.216	0.15	1.62E-28
GABAergic Neurons	SVBP	0.63364	0.932	0.717	1.74E-06
GABAergic Neurons	BEX1	0.62955	0.821	0.835	1.69E-37
GABAergic Neurons	DSTN	0.62593	0.955	0.894	2.21E-24
GABAergic Neurons	GAD1	0.61455	0.679	0.33	1.30E-41
GABAergic Neurons	PROX1	0.61165	0.121	0.332	4.76E-93
GABAergic Neurons	HN1	0.60568	0.963	0.936	6.77E-94
GABAergic Neurons	DCLK1	0.60078	0.368	0.657	2.00E-22
Glutamatergic Neurons	NEUROD6	1.49931	0.9	0.771	0
Glutamatergic Neurons	BHLHE22	1.46368	0.905	0.793	0
Glutamatergic Neurons	STMN2	1.43649	0.99	0.834	0
Glutamatergic Neurons	GRIA2	1.39439	0.829	0.782	0
Glutamatergic Neurons	NEUROD2	1.35791	0.893	0.827	0

. . . Table 1.1 continued.

cluster	**gene**	**avg_logFC**	**pct.1**	**pct.2**	**p_val_adj**
Glutamatergic Neurons	SNAP25	1.24934	0.803	0.764	0
Glutamatergic Neurons	TTC9B	1.20497	0.811	0.771	0
Glutamatergic Neurons	SYT4	1.11807	0.762	0.803	0
Glutamatergic Neurons	SNCA	1.10911	0.829	0.643	0
Glutamatergic Neurons	HMP19	1.10021	0.757	0.753	0
Glutamatergic Neurons	LY6H	1.09133	0.778	0.548	0
Glutamatergic Neurons	RAB3A	1.08320	0.857	0.726	0
Glutamatergic Neurons	INA	1.08214	0.777	0.777	0
Glutamatergic Neurons	GAP43	1.06736	0.943	0.731	0
Glutamatergic Neurons	HPCA	1.03546	0.73	0.624	0
Glutamatergic Neurons	CXADR	1.03219	0.862	0.651	0
Glutamatergic Neurons	TSPAN13	1.02606	0.809	0.57	0
Glutamatergic Neurons	CD24	1.01863	0.91	0.752	0
Glutamatergic Neurons	SYT1	1.00629	0.891	0.773	0
Glutamatergic Neurons	MAPT	1.00501	0.737	0.688	0
Glutamatergic Neurons	DCX	1.00326	0.865	0.661	0
Glutamatergic Neurons	RTN1	0.98969	0.935	0.718	0
Glutamatergic Neurons	NSG1	0.96682	0.796	0.716	0
Glutamatergic Neurons	SCG3	0.95190	0.726	0.736	0
Glutamatergic Neurons	CELF4	0.94679	0.671	0.721	1.75E-274
Glutamatergic Neurons	CRMP1	0.91715	0.878	0.727	0
Glutamatergic Neurons	LMO3	0.90245	0.712	0.805	1.51E-267
Glutamatergic Neurons	NELL2	0.90035	0.749	0.643	0
Glia	KIAA0101	1.09206	0.638	0.486	2.16E-187
Glia	TTYH1	1.07238	0.948	0.689	0.00E+00
Glia	SLC1A3	1.04241	0.855	0.621	0.00E+00
Glia	MT2A	1.00780	0.89	0.624	0.00E+00
Glia	SFRP1	1.00450	0.938	0.684	0.00E+00
Glia	SOX2	1.00279	0.946	0.643	0.00E+00
Glia	HES1	0.99522	0.832	0.59	0.00E+00
Glia	ID4	0.92316	0.912	0.687	0.00E+00
Glia	CLU	0.91605	0.978	0.732	0.00E+00
Glia	PEA15	0.89375	0.917	0.62	0.00E+00
Glia	HOPX	0.86840	0.818	0.622	0.00E+00
Glia	PMP2	0.78593	0.775	0.572	5.97E-304
Glia	METRN	0.76712	0.798	0.583	0.00E+00
Glia	ZFP36L1	0.74666	0.73	0.539	3.48E-258
Glia	PTN	0.74622	0.996	0.894	0.00E+00
Glia	IFI44L	0.74479	0.79	0.595	0.00E+00

. . . Table 1.1 continued.

cluster	gene	avg_logFC	pct.1	pct.2	p_val_adj
Glia	CDO1	0.74388	0.869	0.631	0.00E+00
Glia	VIM	0.73690	0.993	0.858	0.00E+00
Glia	CENPH	0.71893	0.588	0.58	8.18E-45
Glia	HSPB1	0.71396	0.904	0.624	0.00E+00
Glia	PDLIM3	0.71318	0.807	0.62	0.00E+00
Glia	FGFBP3	0.68433	0.797	0.632	0.00E+00
Glia	FAM107A	0.68371	0.748	0.593	1.17E-226
Glia	C8orf4	0.68118	0.668	0.564	2.34E-135
Glia	B2M	0.67571	0.897	0.569	0.00E+00
Glia	PON2	0.67504	0.671	0.426	2.30E-204
Glia	STXBP6	0.66039	0.732	0.638	1.59E-177
Glia	SOX3	0.65821	0.76	0.435	0.00E+00
Glia	HMGB2	0.65603	0.824	0.572	0.00E+00
Glia	QKI	0.64190	0.775	0.611	1.01E-217
Glia	SRI	0.64014	0.899	0.654	0.00E+00
Glia	PHGDH	0.63803	0.766	0.615	1.70E-216
Glia	APOE	0.61466	0.78	0.575	6.86E-190
Glia	FOS	0.60483	0.777	0.642	7.93E-168
Glia	PSAT1	0.60446	0.788	0.598	1.05E-253
Glia	C1orf61	0.60285	0.976	0.863	0.00E+00
Glia	DBI	0.60169	0.932	0.781	0.00E+00
Intermediate Progenitors	EOMES	1.14946	0.697	0.545	1.50E-123
Intermediate Progenitors	TAC3	1.12454	0.535	0.392	3.21E-41
Intermediate Progenitors	NHLH1	1.08712	0.766	0.53	4.67E-254
Intermediate Progenitors	GADD45G	1.00439	0.794	0.619	5.82E-155
Intermediate Progenitors	ELAVL2	0.88637	0.828	0.724	1.16E-130
Intermediate Progenitors	NNAT	0.88553	0.911	0.841	8.74E-188
Intermediate Progenitors	RND3	0.64990	0.54	0.47	3.81E-21
Intermediate Progenitors	NEUROG1	0.62298	0.59	0.585	1.87E-10
Intermediate Progenitors	GDAP1L1	0.62253	0.757	0.671	1.08E-57
Intermediate Progenitors	TAGLN3	0.60150	0.856	0.77	1.68E-98
Early Progenitors	IGFBP7	0.89242	0.559	0.394	1.49E-30
Early Progenitors	TTR	0.84753	0.844	0.49	0
Early Progenitors	S100B	0.74367	0.833	0.481	0
Early Progenitors	SPARCL1	0.61008	0.928	0.434	0
Early Progenitors	TPPP3	0.60842	0.539	0.293	5.00E-23
Early Progenitors	CA2	0.58266289	0.614	0.403	4.70E-69
Early Progenitors	RBP1	0.56764771	0.879	0.438	0
Early Progenitors	TRPM3	0.56440266	0.768	0.324	0

. . . Table 1.1 continued.

cluster	**gene**	**avg_logFC**	**pct.1**	**pct.2**	**p_val_adj**
Early Progenitors	CD9	0.54907859	0.743	0.263	0
Early Progenitors	ID3	0.54768285	0.889	0.558	0
Early Progenitors	CXCL14	0.53064106	0.567	0.402	1.01E-10
Early Progenitors	ID1	0.51512222	0.809	0.495	0
Mitotic Cells	UBE2C	2.08768	0.999	0.38	0
Mitotic Cells	TOP2A	1.92072	0.988	0.456	0
Mitotic Cells	CDC20	1.88666	0.969	0.294	0
Mitotic Cells	CENPF	1.83910	0.993	0.513	0
Mitotic Cells	NUSAP1	1.79161	0.985	0.531	0
Mitotic Cells	PTTG1	1.77245	1	0.532	0
Mitotic Cells	CCNB2	1.73661	0.956	0.298	0
Mitotic Cells	CCNB1	1.71891	0.939	0.362	0
Mitotic Cells	CDK1	1.68391	0.981	0.507	0
Mitotic Cells	ASPM	1.59134	0.939	0.436	0
Mitotic Cells	BIRC5	1.58211	0.963	0.37	0
Mitotic Cells	TPX2	1.55923	0.94	0.524	0
Mitotic Cells	PLK1	1.51556	0.88	0.386	2.04E-293
Mitotic Cells	MAD2L1	1.51083	0.967	0.555	0
Mitotic Cells	FAM64A	1.51073	0.91	0.313	0
Mitotic Cells	CKS2	1.50084	0.997	0.645	0
Mitotic Cells	PBK	1.47827	0.917	0.414	0
Mitotic Cells	CCNA2	1.46832	0.92	0.536	0
Mitotic Cells	GTSE1	1.44523	0.899	0.306	0
Mitotic Cells	AURKA	1.43015	0.876	0.399	1.86E-293
Mitotic Cells	CDKN3	1.40121	0.859	0.321	1.75E-264
Mitotic Cells	AURKB	1.39178	0.901	0.299	0
Mitotic Cells	NUF2	1.38631	0.898	0.478	0
Mitotic Cells	KPNA2	1.38186	0.982	0.578	0
Mitotic Cells	SMC4	1.37867	0.955	0.493	0
Mitotic Cells	HMGB2	1.36699	1	0.612	0
Mitotic Cells	CDCA3	1.36522	0.854	0.425	5.74E-253
Mitotic Cells	PSRC1	1.34100	0.914	0.501	2.10E-296
Mitotic Cells	CENPA	1.32905	0.869	0.291	0
Mitotic Cells	CKS1B	1.32614	0.971	0.525	0
Other	LGALS1	1.34401	0.97	0.479	1.62E-80
Other	IGF2	1.26378	0.955	0.402	7.22E-142
Other	COL3A1	1.25618	0.973	0.439	1.48E-136
Other	RBP1	1.14081	0.967	0.531	1.32E-123
Other	MGP	1.00395	0.602	0.45	5.94E-05

…Table 1.1 continued.

cluster	**gene**	**avg_logFC**	**pct.1**	**pct.2**	**p_val_adj**
Other	DCN	0.95928	0.554	0.484	0.56345
Other	IFITM3	0.91015	0.708	0.362	5.14E-36
Other	COL1A1	0.89389	0.545	0.363	1
Other	SPARC	0.83734	0.916	0.663	2.93E-66
Other	APOE	0.81812	0.88	0.617	7.53E-38
Other	ANXA1	0.80045	0.867	0.335	6.95E-109

Table 1.2: Supplemental Table 2. Electrophysiological features in preterm neonatal EEG dataset and analogous features computed in organoid LFP. Related to Figure 1.4.

Neonatal EEG features	**Computed organoid LFP features**
Envelope (50%)	None
Envelope (5%)	None
Envelope (95%)	None
rEEG (50%)	None
rEEG (5%)	None
rEEG (95%)	None
SATs per hour	***Network Events per hour***
RMS SAT duration	***RMS network event duration***
SAT duration (50%)	***Network event duration (50%)***
SAT duration (5%)	***Network event duration (5%)***
SAT duration (95%)	***Network event duration (95%)***
RMS Inter-SAT Duration	***RMS Inter-event Duration***
Inter-SAT duration (50%)	***Inter-event duration (50%)***
Inter-SAT duration (5%)	***Inter-event duration (5%)***
Inter-SAT duration (95%)	***Inter-event duration (95%)***
Temporal Theta Power	None
Activation Synchrony Index	None
Interhemispheric Correlation	None
Total Spectral Power	None
Relative Delta Power	***Relative Delta Power***
Relative Theta Power	***Relative Theta Power***
Relative Alpha Power	***Relative Alpha Power***
Relative Beta Power	Relative Beta Power

Bolded and italic cells indicate features used in the development time prediction model.

Bibliography

Allene, C., Cattani, A., Ackman, J. B., Bonifazi, P., Aniksztejn, L., Ben-Ari, Y., & Cossart, R. (2008). Sequential generation of two distinct Synapse-Driven network patterns in developing neocortex. Journal of Neuroscience, 28, 12851–12863.

Ben-Ari, Y. (2001). Developing networks play a similar melody. Trends Neurosci., 24, 353–360.

Birey, F., Andersen, J., Makinson, C. D., Islam, S., Wei, W., Huber, N., Fan, H. C., Metzler, K. R. C., Panagiotakos, G., Thom, N., O'Rourke, N. A., Steinmetz, L. M., Bernstein, J. A., Hallmayer, J., Huguenard, J. R., & Paşca, S. P. (2017). Assembly of functionally integrated human forebrain spheroids. Nature, 545, 54–59.

Blankenship, A. G. & Feller, M. B. (2010). Mechanisms underlying spontaneous patterned activity in developing neural circuits. Nat. Rev. Neurosci., 11, 18–29.

Butler, A., Hoffman, P., Smibert, P., Papalexi, E., & Satija, R. (2018). Integrating single-cell transcriptomic data across different conditions, technologies, and species. Nat. Biotechnol., 36, 411–420.

Buzsáki, G., Anastassiou, C. A., & Koch, C. (2012). The origin of extracellular fields and currents–EEG, ECoG, LFP and spikes. Nat. Rev. Neurosci., 13, 407–420.

Buzsáki, G. & Draguhn, A. (2004). Neuronal oscillations in cortical networks. Science, 304, 1926–1929.

Buzsáki, G., Logothetis, N., & Singer, W. (2013). Scaling brain size, keeping timing: evolutionary preservation of brain rhythms. Neuron, 80, 751–764.

Camp, J. G., Badsha, F., Florio, M., Kanton, S., Gerber, T., Wilsch-Bräuninger, M., Lewitus, E., Sykes, A., Hevers, W., Lancaster, M., Knoblich, J. A., Lachmann, R., Pääbo, S., Huttner, W. B., & Treutlein, B. (2015). Human cerebral organoids recapitulate gene expression programs of fetal neocortex development. Proc. Natl. Acad. Sci. U. S. A., 112, 15672–15677.

Cederquist, G. Y., Asciolla, J. J., Tchieu, J., Walsh, R. M., Cornacchia, D., Resh, M. D., & Studer, L. (2019). Specification of positional identity in forebrain organoids. Nat. Biotechnol., 37, 436–444.

De Hemptinne, C., Swann, N. C., Ostrem, J. L., Ryapolova-Webb, E. S., San Luciano, M., Galifianakis, N. B., & Starr, P. A. (2015). Therapeutic deep brain stimulation reduces cortical phase-amplitude coupling in parkinson's disease. Nat. Neurosci., 18, 779–786.

Donoghue, T., Haller, M., Peterson, E. J., Varma, P., Sebastian, P., Gao, R., Noto, T., Lara, A. H., Wallis, J. D., Knight, R. T., Shestyuk, A., & Voytek, B. (2020). Parameterizing neural power spectra into periodic and aperiodic components. Nat. Neurosci., 23, 1655–1665.

Farahany, N. A., Greely, H. T., Hyman, S., Koch, C., Grady, C., Pașca, S. P., Sestan, N., Arlotta, P., Bernat, J. L., Ting, J., Lunshof, J. E., Iyer, E. P. R., Hyun, I., Capestany, B. H., Church, G. M., Huang, H., & Song, H. (2018). The ethics of experimenting with human brain tissue. Nature, 556, 429–432.

Fries, P. (2005). A mechanism for cognitive dynamics: neuronal communication through neuronal coherence. Trends Cogn. Sci., 9, 474–480.

Gao, R., Peterson, E. J., & Voytek, B. (2017). Inferring synaptic excitation/inhibition balance from field potentials. Neuroimage, 158, 70–78.

Gertsman, I., Gangoiti, J. A., & Barshop, B. A. (2014). Validation of a dual LC–HRMS platform for clinical metabolic diagnosis in serum, bridging quantitative analysis and untargeted metabolomics. Metabolomics, 10, 312–323.

Giandomenico, S. L., Mierau, S. B., Gibbons, G. M., Wenger, L. M. D., Masullo, L., Sit, T., Sutcliffe, M., Boulanger, J., Tripodi, M., Derivery, E., Paulsen, O., Lakatos, A., & Lancaster, M. A. (2019). Cerebral organoids at the air-liquid interface generate diverse nerve tracts with functional output. Nat. Neurosci., 22, 669–679.

Henriques, J. B. & Davidson, R. J. (1991). Left frontal hypoactivation in depression. J. Abnorm. Psychol., 100, 535–545.

Johnson, M. H. (2001). Functional brain development in humans. Nat. Rev. Neurosci., 2, 475–483.

Kelava, I. & Lancaster, M. A. (2016). Stem cell models of human brain development. Cell Stem Cell, 18, 736–748.

Khan, S., Gramfort, A., Shetty, N. R., Kitzbichler, M. G., Ganesan, S., Moran, J. M., Lee, S. M., Gabrieli, J. D. E., Tager-Flusberg, H. B., Joseph, R. M., Herbert, M. R., Hämäläinen, M. S., & Kenet, T. (2013). Local and long-range functional connectivity is reduced in concert in autism spectrum disorders. Proc. Natl. Acad. Sci. U. S. A., 110, 3107–3112.

Khazipov, R. & Luhmann, H. J. (2006). Early patterns of electrical activity in the developing cerebral cortex of humans and rodents. Trends Neurosci., 29, 414–418.

Lancaster, M. A. & Knoblich, J. A. (2014). Generation of cerebral organoids from human pluripotent stem cells. Nat. Protoc., 9, 2329–2340.

Lancaster, M. A., Renner, M., Martin, C.-A., Wenzel, D., Bicknell, L. S., Hurles, M. E., Homfray, T., Penninger, J. M., Jackson, A. P., & Knoblich, J. A. (2013). Cerebral organoids model human brain development and microcephaly. Nature, 501, 373–379.

Luo, C., Lancaster, M. A., Castanon, R., Nery, J. R., Knoblich, J. A., & Ecker, J. R. (2016). Cerebral organoids recapitulate epigenomic signatures of the human fetal brain. Cell Rep., 17, 3369–3384.

Manning, J. R., Jacobs, J., Fried, I., & Kahana, M. J. (2009). Broadband shifts in local field potential power spectra are correlated with single-neuron spiking in humans. J. Neurosci., 29, 13613–13620.

Mariani, J., Simonini, M. V., Palejev, D., Tomasini, L., Coppola, G., Szekely, A. M., Horvath, T. L., & Vaccarino, F. M. (2012). Modeling human cortical development in vitro using induced pluripotent stem cells. Proc. Natl. Acad. Sci. U. S. A., 109, 12770–12775.

Miller, K. J., Leuthardt, E. C., Schalk, G., Rao, R. P. N., Anderson, N. R., Moran, D. W., Miller, J. W., & Ojemann, J. G. (2007). Spectral changes in cortical surface potentials during motor movement. Journal of Neuroscience, 27, 2424–2432.

Moore, S. M., Seidman, J. S., Ellegood, J., Gao, R., Savchenko, A., Troutman, T. D., Abe, Y., Stender, J., Lee, D., Wang, S., Voytek, B., Lerch, J. P., Suh, H., Glass, C. K., & Muotri, A. R. (2019). Setd5 haploinsufficiency alters neuronal network connectivity and leads to autistic-like behaviors in mice. Transl. Psychiatry, 9, 24.

Mukamel, R., Gelbard, H., Arieli, A., Hasson, U., Fried, I., & Malach, R. (2005). Coupling between neuronal firing, field potentials, and FMRI in human auditory cortex. Science, 309, 951–954.

Nageshappa, S., Carromeu, C., Trujillo, C. A., Mesci, P., Espuny-Camacho, I., Pasciuto, E., Vanderhaeghen, P., Verfaillie, C. M., Raitano, S., Kumar, A., Carvalho, C. M. B., Bagni, C., Ramocki, M. B., Araujo, B. H. S., Torres, L. B., Lupski, J. R., Van Esch, H., & Muotri, A. R. (2016). Altered neuronal network and rescue in a human MECP2 duplication model. Mol. Psychiatry, 21, 178–188.

Opitz, T., De Lima, A. D., & Voigt, T. (2002). Spontaneous development of synchronous oscillatory activity during maturation of cortical networks in vitro. J. Neurophysiol., 88, 2196–2206.

Paşca, A. M., Sloan, S. A., Clarke, L. E., Tian, Y., Makinson, C. D., Huber, N., Kim, C. H., Park, J.-Y., O'Rourke, N. A., Nguyen, K. D., Smith, S. J., Huguenard, J. R., Geschwind, D. H., Ben A Barres, & Paşca, S. P. (2015). Functional cortical neurons and astrocytes from human pluripotent stem cells in 3D culture. Nat. Methods, 12, 671–678.

Paşca, S. P. (2018). The rise of three-dimensional human brain cultures. Nature, 553, 437–445.

Pedregosa, F., Varoquaux, G., Gramfort, A., Michel, V., Thirion, B., Grisel, O., Blondel, M., Prettenhofer, P., Weiss, R., Dubourg, V., & Others (2011). Scikit-learn: Machine learning in python. the Journal of machine Learning research, 12, 2825–2830.

Power, J. D., Fair, D. A., Schlaggar, B. L., & Petersen, S. E. (2010). The development of human functional brain networks. Neuron, 67, 735–748.

Qian, X., Nguyen, H. N., Song, M. M., Hadiono, C., Ogden, S. C., Hammack, C., Yao, B., Hamersky, G. R., Jacob, F., Zhong, C., Yoon, K.-J., Jeang, W., Lin, L., Li, Y., Thakor, J., Berg, D. A., Zhang, C., Kang, E., Chickering, M., Nauen, D., Ho, C.-Y., Wen, Z., Christian, K. M., Shi, P.-Y., Maher, B. J., Wu, H., Jin, P., Tang, H., Song, H., & Ming, G.-L. (2016). Brain-Region-Specific organoids using mini- bioreactors for modeling ZIKV exposure. Cell, 165, 1238–1254.

Quadrato, G., Nguyen, T., Macosko, E. Z., Sherwood, J. L., Min Yang, S., Berger, D. R., Maria, N., Scholvin, J., Goldman, M., Kinney, J. P., Boyden, E. S., Lichtman, J. W., Williams, Z. M., McCarroll, S. A., & Arlotta, P. (2017). Cell diversity and network dynamics in photosensitive human brain organoids. Nature, 545, 48–53.

Quiroga, R. Q., Reddy, L., Kreiman, G., Koch, C., & Fried, I. (2005). Invariant visual representation by single neurons in the human brain. Nature, 435, 1102–1107.

Renner, M., Lancaster, M. A., Bian, S., Choi, H., Ku, T., Peer, A., Chung, K., & Knoblich, J. A. (2017). Self-organized developmental patterning and differentiation in cerebral organoids. EMBO J., 36, 1316–1329.

Schevon, C. A., Weiss, S. A., McKhann, Jr, G., Goodman, R. R., Yuste, R., Emerson, R. G., & Trevelyan, A. J. (2012). Evidence of an inhibitory restraint of seizure activity in humans. Nat. Commun., 3, 1060.

Stevenson, N. J., Oberdorfer, L., Koolen, N., Toole, J. M. O. X., Werther, T., Klebermass-Schrehof, K., & Vanhatalo, S. (2017). Functional maturation in preterm infants measured by serial recording of cortical activity. Sci. Rep., 7, 1–7.

Stuart, T., Butler, A., Hoffman, P., Hafemeister, C., Papalexi, E., Mauck, W. M., Stoeckius, M., Smibert, P., & Satija, R. (????). Comprehensive integration of single cell data.

Tang, X., Kim, J., Zhou, L., Wengert, E., Zhang, L., Wu, Z., Carromeu, C., Muotri, A. R., Marchetto, M. C. N., Gage, F. H., & Chen, G. (2016). KCC2 rescues functional deficits in human neurons derived from patients with rett syndrome. Proc. Natl. Acad. Sci. U. S. A., 113, 751–756.

Tetzlaff, C., Okujeni, S., Egert, U., Wörgötter, F., & Butz, M. (2010). Self-organized criticality in developing neuronal networks. PLoS Comput. Biol., 6, e1001013.

Thomas, C. A., Tejwani, L., Trujillo, C. A., Negraes, P. D., Herai, R. H., Mesci, P., Macia, A., Crow, Y. J., & Muotri, A. R. (2017). Modeling of TREX1-Dependent autoimmune disease using human stem cells highlights L1 accumulation as a source of neuroinflammation. Cell Stem Cell, 21, 319–331.e8.

Tolonen, M., Palva, J. M., Andersson, S., & Vanhatalo, S. (2007). Development of the spontaneous activity transients and ongoing cortical activity in human preterm babies. Neuroscience, 145, 997–1006.

Tort, A. B. L., Komorowski, R., Eichenbaum, H., & Kopell, N. (2010). Measuring Phase-Amplitude coupling between neuronal oscillations of different frequencies.

Uhlhaas, P. J., Roux, F., Rodriguez, E., Rotarska-Jagiela, A., & Singer, W. (2010). Neural synchrony and the development of cortical networks. Trends Cogn. Sci., 14, 72–80.

Uhlhaas, P. J. & Singer, W. (2010). Abnormal neural oscillations and synchrony in schizophrenia. Nat. Rev. Neurosci., 11, 100–113.

Uylings, H. B. M., Delalle, I., Petanjek, Z., & Koenderink, M. J. T. (2002). Structural and immunocytochemical differentiation of neurons in prenatal and postnatal human prefrontal cortex. Neuroembryology Aging, 1, 176–186.

van de Leemput, J., Boles, N. C., Kiehl, T. R., Corneo, B., Lederman, P., Menon, V., Lee, C., Martinez, R. A., Levi, B. P., Thompson, C. L., Yao, S., Kaykas, A., Temple, S., & Fasano, C. A. (2014). CORTECON: a temporal transcriptome analysis of in vitro human cerebral cortex development from human embryonic stem cells. Neuron, 83, 51–68.

Van Hove, J. L. K. & Thomas, J. A. (2014). Disorders of glycine, serine, GABA, and proline metabolism. In Physician's Guide to the Diagnosis, Treatment, and Follow-Up of Inherited Metabolic Diseases, N. Blau, M. Duran, K. M. Gibson, & C. Dionisi Vici, eds. (Berlin, Heidelberg: Springer Berlin Heidelberg), pp. 63–83.

Voytek, B., Kayser, A. S., Badre, D., Fegen, D., Chang, E. F., Crone, N. E., Parvizi, J., Knight, R. T., & D'Esposito, M. (2015). Oscillatory dynamics coordinating human frontal networks in support of goal maintenance. Nat. Neurosci., 18, 1318–1324.

Voytek, B. & Knight, R. T. (2015). Dynamic network communication as a unifying neural basis for cognition, development, aging, and disease. Biol. Psychiatry, 77, 1089–1097.

Xiang, Y., Tanaka, Y., Cakir, B., Patterson, B., Kim, K.-Y., Sun, P., Kang, Y.-J., Zhong, M., Liu, X., Patra, P., Lee, S.-H., Weissman, S. M., & Park, I.-H. (2019). hESC-Derived thalamic organoids form reciprocal projections when fused with cortical organoids. Cell Stem Cell, 24, 487–497.e7.

Xiang, Y., Tanaka, Y., Patterson, B., Kang, Y.-J., Govindaiah, G., Roselaar, N., Cakir, B., Kim, K.-Y., Lombroso, A. P., Hwang, S.-M., Zhong, M., Stanley, E. G., Elefanty, A. G., Naegele, J. R., Lee, S.-H., Weissman, S. M., & Park, I.-H. (2017). Fusion of regionally specified hPSC-Derived organoids models human brain development and interneuron migration. Cell Stem Cell, 21, 383–398.e7.

Yoon, S.-J., Elahi, L. S., Pașca, A. M., Marton, R. M., Gordon, A., Revah, O., Miura, Y., Walczak, E. M., Holdgate, G. M., Fan, H. C., Huguenard, J. R., Geschwind, D. H., & Pașca, S. P. (2019). Reliability of human cortical organoid generation. Nat. Methods, 16, 75–78.

Zerbino, D. R., Achuthan, P., Akanni, W., Amode, M. R., Barrell, D., Bhai, J., Billis, K., Cummins, C., Gall, A., Girón, C. G., Gil, L., Gordon, L., Haggerty, L., Haskell, E., Hourlier, T., Izuogu, O. G., Janacek, S. H., Juettemann, T., To, J. K., Laird, M. R., Lavidas, I., Liu, Z., Loveland, J. E., Maurel, T., McLaren, W., Moore, B., Mudge, J., Murphy, D. N., Newman, V., Nuhn, M., Ogeh, D., Ong, C. K., Parker, A., Patricio, M., Riat, H. S., Schuilenburg, H., Sheppard, D., Sparrow, H., Taylor, K., Thormann, A., Vullo, A., Walts, B., Zadissa, A., Frankish, A., Hunt, S. E., Kostadima, M., Langridge, N., Martin, F. J., Muffato, M., Perry, E., Ruffier, M., Staines, D. M., Trevanion, S. J., Aken, B. L., Cunningham, F., Yates, A., & Flicek, P. (2018). Ensembl 2018. Nucleic Acids Res., 46, D754–D761.

Zheng, G. X. Y., Terry, J. M., Belgrader, P., Ryvkin, P., Bent, Z. W., Wilson, R., Ziraldo, S. B., Wheeler, T. D., McDermott, G. P., Zhu, J., Gregory, M. T., Shuga, J., Montesclaros, L., Underwood, J. G., Masquelier, D. A., Nishimura, S. Y., Schnall-Levin, M., Wyatt, P. W., Hindson, C. M., Bharadwaj, R., Wong, A., Ness, K. D., Beppu, L. W., Deeg, H. J., McFarland, C., Loeb, K. R., Valente, W. J., Ericson, N. G., Stevens, E. A., Radich, J. P., Mikkelsen, T. S., Hindson, B. J., & Bielas, J. H. (2017). Massively parallel digital transcriptional profiling of single cells. Nat. Commun., 8, 14049.

Chapter 2

Inferring synaptic excitation/inhibition balance from field potentials

Abstract

Neural circuits sit in a dynamic balance between excitation (E) and inhibition (I). Fluctuations in E:I balance have been shown to influence neural computation, working memory, and information flow, while more drastic shifts and aberrant E:I patterns are implicated in numerous neurological and psychiatric disorders. Current methods for measuring E:I dynamics require invasive procedures that are difficult to perform in behaving animals, and nearly impossible in humans. This has limited the ability to examine the full impact that E:I shifts have in cognition and disease. In this study, we develop a computational model to show that E:I changes can be estimated from the power law exponent (slope) of the electrophysiological power spectrum. Predictions from the model are validated in published data from two species (rats and macaques). We find that reducing E:I ratio via the administration of general anesthetic in macaques results in steeper power spectra, tracking conscious state over time. This causal result is supported by inference from known anatomical E:I changes across the depth of rat hippocampus, as well as

oscillatory theta-modulated dynamic shifts in E:I. Our results provide evidence that E:I ratio may be inferred from electrophysiological recordings at many spatial scales, ranging from the local field potential to surface electrocorticography. This simple method for estimating E:I ratio—one that can be applied retrospectively to existing data—removes a major hurdle in understanding a currently difficult to measure, yet fundamental, aspect of neural computation.

2.1 Introduction

Neurons are constantly bombarded with spontaneous synaptic inputs. This state of fluctuating activity is referred to as the high-conductance state (Destexhe et al., 2003), and gives rise to the asynchronous, irregular (Poisson-like) firing observed in vivo (Destexhe et al., 2001). In this state, neural circuits sit in a balance between synaptic excitation (E) and inhibition (I), typically consisting of fast glutamate and slower GABA inputs, respectively, where inhibition is two to six times the strength of excitation (Alvarez & Destexhe, 2004; Xue et al., 2014). Physiologically, the balance of E:I interaction is essential for neuronal homeostasis (Turrigiano & Nelson, 2004) and the formation of neural oscillations (Atallah & Scanziani, 2009). Computationally, E:I balance allows for efficient information transmission and gating (Salinas & Sejnowski, 2001; Vogels & Abbott, 2009), network computation (Mariño et al., 2005), and working memory maintenance (Lim & Goldman, 2013). Conversely, an imbalance between excitation and inhibition, during key developmental periods or tonically thereafter, is implicated in neurological and psychiatric disorders such as epilepsy (González-Ramírez et al., 2015; Symonds, 1959), schizophrenia (Uhlhaas & Singer, 2010), and autism (Dani et al., 2005; Mariani et al., 2015; Rubenstein & Merzenich, 2003), as well as impairments in information processing and social exploration (Yizhar et al., 2011).

Given such a state of intricate balance and its profound consequences when disturbed, quantifying the E:I ratio could aid in better characterizing the functional state of the brain. Existing methods for estimating E:I ratio focus predominantly on interrogation of precisely selected cells, either through identification of excitatory and inhibitory neurons based on extracellular action potential waveforms (Peyrache et al., 2012), or by intracellular voltage-clamp recordings to measure synaptic currents (Monier et al., 2008), often combined with pharmacological or optogenetic manipulations (Reinhold et al., 2015; Xue et al., 2014). These methods are invasive and are restricted to small populations of cells, making them difficult to apply clinically and to in vivo population-level analyses critical for understanding neural network functioning. Other methods, such as magnetic resonance spectroscopy (Henry et al., 2011) and dynamic causal modeling (Legon et al., 2016), are able to provide greater spatial coverage, enabling the sampling of E:I ratio across the brain. However, this gain comes at a cost of temporal resolution – requiring several minutes of data for a single snapshot – and are based on restrictive connectivity assumptions.

Here, we aim to address this important gap in methodology to measure E:I ratio with broad population coverage and fine temporal resolution. Two recent lines of modeling work motivate our starting hypothesis. First, it has been shown that synaptic input fluctuations during the high conductance state can be accurately modeled by a summation of two stationary stochastic processes representing excitatory and inhibitory inputs (Alvarez & Destexhe, 2004). These inputs have different rates of decay, corresponding to a faster AMPA current and a slower GABAA current, which can be readily differentiated in the frequency domain and computationally inferred from single membrane voltage traces (Pospischil et al., 2009)(Fig. 2.1B). Second, population-level neural field recordings, such as the local field potential (LFP) and electrocorticography (ECoG), have been shown to be primarily dominated by postsynaptic currents (PSC) across large populations (Buzsáki et al., 2012; Mazzoni et al., 2015; Miller et al., 2009). Additionally, recent work by (Haider et al., 2016) observed tight coupling between the LFP and synaptic inputs in the time domain. Thus, we combine these two findings and reason that changes in the relative contribution between excitatory and inhibitory synaptic currents must also be reflected in the field potential, and in particular, in the frequency domain representation (power spectral density, or PSD) of LFP and ECoG recordings. In this work, we derive a straightforward metric that closely tracks E:I ratio via computational modeling, and demonstrate its empirical validity by reanalyzing publically available databases from two different mammalian species. Specifically, we test the hypotheses that anatomical and theta oscillation-modulated changes in excitation and inhibition in the rat hippocampus can be inferred from CA1 local field potentials, and that anesthesia-induced global inhibition is reflected in macaque cortical electrocorticography.

2.2 Materials & Methods

LFP simulation. We simulate local field potentials under the high conductance state (Alvarez & Destexhe, 2004), with the assumption that the LFP is a linear summation of total excitatory and inhibitory currents (Mazzoni et al., 2015). Poisson spike trains from one excitatory and one inhibitory population are generated by integrating interspike intervals (ISI) drawn from independent exponential distributions, with specified mean rate parameter (Fig. 2.1A). Each spike train is convolved with their respective conductance profiles, which are modeled as a difference-of-exponentials defined by the rise and decay time constants of AMPA and GABAA receptors (Eq.2.1, Fig. 2.1B). Aggregate values for synaptic constants are taken from CNRGlab @ UWaterloo (see Neurotransmitter Time Constants in Ref; Table 2.1). The two resulting time series represent total excitatory (gE) and inhibitory (gI) conductances, respectively (Fig. 2.1C). E:I ratio is defined as the ratio of mean excitatory conductance to mean inhibitory conductance over the simulation time, and specific E:I ratios are achieved by multiplying the inhibitory conductance by a constant, such that mean gI is 2-6 times mean gE. To calculate current, conductances are multiplied by the difference between resting potential (-65 mV) and AMPA and GABAA reversal potential, respectively. Local field potential (LFP), finally, is computed as the summation of the total excitatory and inhibitory current. All simulation parameters are specified in Table 2.1. Total

LFP power is normalized to unity for each E:I ratio.

$$PSC(t) = C(-e^{\frac{-t}{\tau_{rise}}} + e^{\frac{-t}{\tau_{decay}}}) \tag{2.1}$$

Equation 1. Difference-of-exponential PSC in time domain

Table 2.1: LFP Simulation Parameters.

Parameter	**Value**
Population Firing Rate (E, I)	2 Hz, 5 Hz
Population Size (E, I)	8000, 2000
Resting Membrane Potential	-65 mV
Reversal Potential (AMPA, GABAA)	0 mV, -80 mV
Conductance Rise Time (AMPA, GABAA)	0.1 ms, 0.5 ms
Conductance Decay Time (AMPA, GABAA)	2 ms, 10 ms
E:I Ratio	1:2 to 1:6

Power spectral density (PSD). For all time series data (simulated and recorded LFP, ECoG), the PSD is estimated by computing the median of the square magnitude of the sliding window (short-time) Fourier transform (STFT). The median was used instead of the mean (Welch's method) to account for the non-Gaussian distribution of spectral data, as well as to eliminate the contributions of extreme outliers. All STFT are computed with a window length of 1 second (2-seconds for CA1 data), and an overlap length of 0.25 seconds. A hamming window of corresponding length is applied prior to taking the FFT.

1/f Slope Fitting. To compute the 1/f power law exponent (log-log slope), we use robust linear regression (MATLAB robustfit.m) to find the slope for the line of best fit over specified frequency ranges of the PSD (30-50 Hz, 40-60 Hz for macaque ECoG due to the prescence of oscillations near 30Hz) (Eq.2).

$$argmin_{b,\chi}\,[log_{10}PSD - (b + \chi log_{10}F)],\, F \in [30,50]\, or\, [40,60] Hz \tag{2.2}$$

Equation 2. Log-Log Linear Fit Parameter over Empirical PSD

Hippocampal LFP and CA1 depth analysis. LFP data (1250 Hz sampling rate) is recorded in stratum pyramidale of CA1 via 4 to 8 shank electrodes (200-μm inter-shank distance), with 8 electrodes (160-μm^2 area) along the depth of each shank (20-μm spacing), perpendicular to the pyramidal cell body layer (Mizuseki et al., 2009). PSD is computed for each electrode as specified above, and 1/f slope extracted. As in (Mizuseki et al., 2011), we align the shanks such that the electrode with the maximal ripple power (150-250 Hz) is set to position 0, the middle of stratum pyramidale. Other electrodes are vertically translated accordingly. This procedure is repeated for all shanks in every recording (4 rats, 20 sessions total), resulting in slope estimates spanning a depth of 280-μm, centered on the pyramidal layer. AMPA and GABAA synapse densities are adapted from (Megías et al., 2001), for proximal stratum oriens and stratum radiatum dendrites, and smoothed with a 5-point Gaussian window to produce 15 data points at positions equivalent to LFP electrodes. Spearman correlation is computed by pooling slope values at the same depth across all sessions and all rats.

Multivariate Regression Model. Since the synaptic density estimates for E and I are independent but correlated measurements, and E:I ratio is dependent on both previous measures, we built a multivariate regression model to better delineate contributions from the synaptic variables. Combinations of E, I, and E:I ratio were used as predictors, and slope as the predicted variable, and we compute model coefficient, significance, and ordinary and adjusted R2 values (MATLAB, LinearModel.fit). In addition, bootstrap analysis was performed for each predictor combination (custom Python code), wherein 25 subsamples were randomly selected from the dataset and a regression model was built to compute one adjusted R2 value for the subsampled model. This was repeated 500 times to build a distribution of adjusted R2 values for each model (predictor combination), and model fitness was compared using paired-samples t-test.

Theta phase-modulated slope. Theta oscillation is first isolated with a FIR bandpass filter 5-12 Hz, (EEGLAB, eegfilt.m). Theta phase is computed as the complex phase angle of the Hilbert transform of the theta oscillation. Segments of theta phase are categorized as peak [$-\pi/2$ to $\pi/2$, through 0] or trough [$\pi/2$ to $3\pi/2$, through π]. Each corresponding segment in the raw data (75 samples) is then labeled as peak or trough, Hamming-windowed, and padded to 1250 samples. Average PSD for each phase category is computed as the median of all windowed FFT of the data segments of that category. 1/f slope is then fit to the average PSDs. Per-channel significance statistics are calculated by fitting 1/f slope to each individual cycle STFT for each channel and compared using two-sample t-test. To avoid power contamination in the short-time window estimates from observed beta oscillation, LFP data is notch filtered between 15-25 Hz. All results do not change when not filtered for beta, hence are not presented below.

Macaque ECoG During Anesthesia. ECoG data was collected from 2 macaque monkeys during rest, delivery of anesthesia (propofol, 5 & 5.2 mg/kg), and recovery (Yanagawa et al., 2013). PSD was computed for all ECoG channels (n = 128) for each experimental condition and fitted for 1/f slope. Due to clear gamma oscillation near 30 Hz biasing slope estimates, we fit over 40-60 Hz to avoid oscillatory contamination. We then compared slope fit differences at each electrode between conditions (paired-samples t-test). Time resolved slope fit was achieved by computing sliding window spectra (absolute value squared of FFT) throughout the duration of the recording (1 s window, 0.25 s step), and a slope estimate was computed for each window. A 15-second median filter was applied to smooth the slope time series plot for Fig. 2.4D. Simulation and analysis code can be found at https://github.com/voytekresearch/EISlope.

2.3 Results

E:I ratio drives 1/f changes in simulation

To model LFP under the high conductance state, we simulate an efferent “LFP” population receiving independent Poissonic spike trains from an excitatory and an inhibitory population, as detailed in the Methods. In the frequency domain, we observe that the power spectral density of the

LFP (LFP-PSD) follows a decaying (1/f) power law for frequencies past 20 Hz (negatively linear in log-log plot), which directly results from adding the two current components, both following power law decays (Fig. 2.1D). Note that the current-PSDs begin decaying at different frequencies, due to the different rise and decay time constants of AMPA and GABAA conductance profiles, which have been previously observed in intracellular models of the balanced, high conductance state (Destexhe & Rudolph, 2004).

By changing the relative contributions of excitation and inhibition (E:I ratio), we shift the frequency at which the current-PSDs cross over, which in turn produces different LFP-PSD slopes (power law exponent) in the intermediate frequency range (Fig. 2.1E). To quantify this relationship, we vary E:I ratio from 1:2 to 1:6, and observe that LFP-PSD slope between 30 to 50 Hz positively correlates with E:I ratio ($r = 0.55$, $p < 0.01$; Fig. 2.1F). The change in slope is restricted to only the low-to-intermediate frequency ranges (below 100 Hz), as we observe a steady decline in correlation between E:I ratio and PSD slope when slope is fitted across shifting, 20-Hz wide frequency windows (Fig. 2.1G). For subsequent slope analyses, we use a 20-Hz window of the lowest possible frequencies that are above visible oscillatory peaks in the PSD, as a clear drop in correlation is observed when a narrowband oscillation, such as beta (15-25 Hz), is present. Additionally, we avoid high frequency regions because action potentials and firing rate changes have been shown to alter high gamma power at frequencies as low as 50 Hz (Manning et al., 2009; Miller et al., 2007; Ray & Maunsell, 2011). In summary, our forward LFP model suggests that E:I ratio is monotonically related to LFP-PSD slope in a range between 30-70 Hz, when uncorrupted by oscillatory peaks, and that increasing E:I ratio increases (flattens) PSD slope.

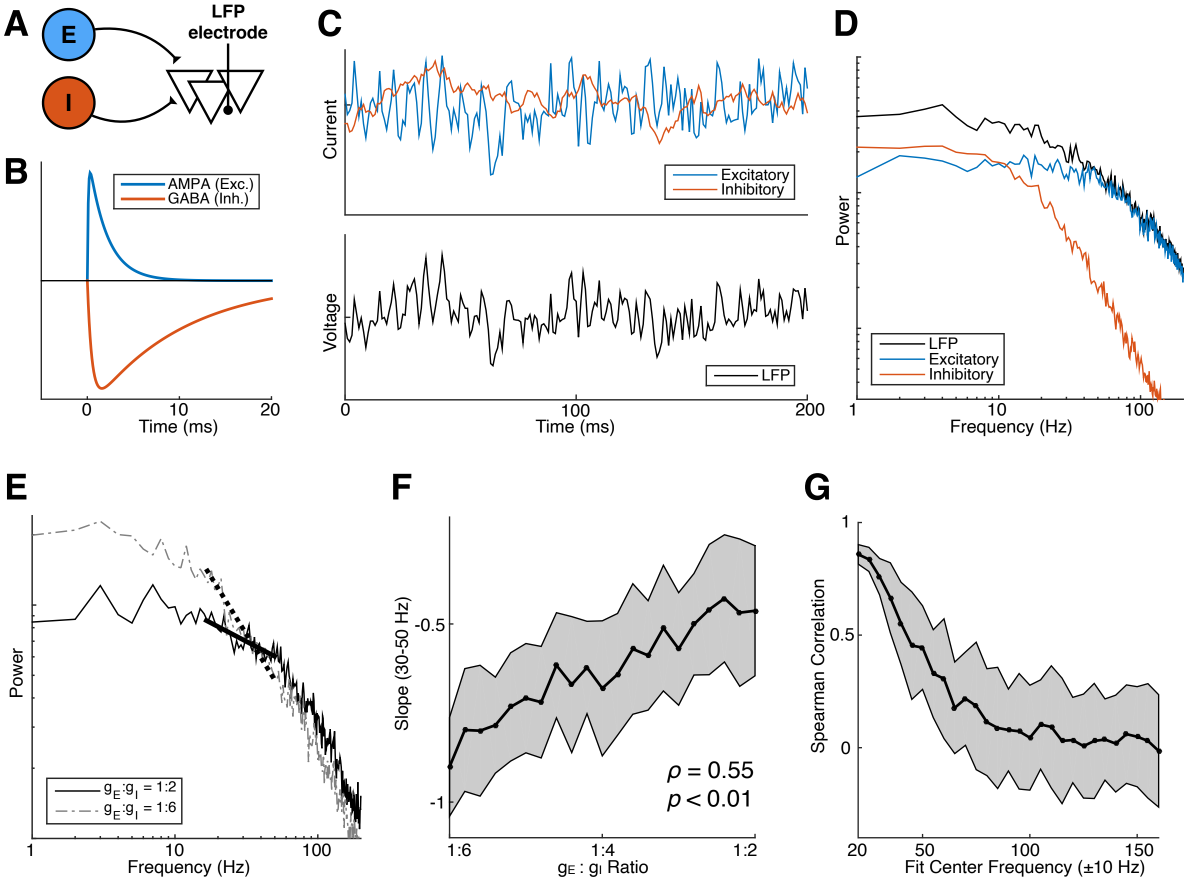

Figure 2.1: E:I ratio correlates with PSD slope in simulation. (A) Model schematic: an "LFP population" receives input from two Poisson populations, one excitatory and one inhibitory. (B) AMPA and GABAA conductance profiles follow a difference-of-exponentials with different rise and decay time constants. (C) Example time trace of simulated total synaptic currents (top) and LFP (bottom). (D) PSDs of simulated signals in (C). Note power law decays in current-PSDs that begin at different frequencies. (E) Increasing E:I ratio from 1:6 to 1:2 causes a rotation, producing a flatter PSD. (F) E:I ratio is positively correlated with PSD slope between 30-50 Hz. (G) Positive rank correlations between E:I ratio and PSD slope diminish with increasing frequency of fitting window, up to 100 Hz.

Depth-varying synapse density in rat CA1

To test the relationship between E:I ratio and PSD slope empirically, we first take advantage of the fact that excitatory and inhibitory synapse densities vary along the pyramidal dendrites in the CA1 region of the rat hippocampus (Megías et al., 2001). Given the results of the above modeling experiment, we ask: can changes in the ratio of excitatory to inhibitory synapse density be captured by changes in PSD slope, measured along the depth of CA1? Shank recordings are obtained from CRCNS data portal (Mizuseki et al., 2009), sampling LFP at evenly spaced electrodes across a depth of 280 μm centered (post hoc, see Methods) on the pyramidal cell layer in CA1 (Fig. 2.2A). PSDs are computed using data from entire recording sessions of open field foraging (Fig. 2.2B). PSD slopes are then fitted between 30-50 Hz to arrive at a slope profile that varied across depth (Fig. 2.2C). To compute E:I ratio, we adapt synapse density values from (Megías et al., 2001) and spatially smooth it to produce data points at equivalent LFP electrode depths (Fig. 2.2D).

We find that PSD slope across depth is significantly correlated with the AMPA to GABAA synapse ratio (Spearman's $\rho = 0.23$, $p < 10^{-5}$), corroborating our a priori simulation results (Fig. 2.2E). Interestingly, inhibitory synapse density alone correlates more strongly with PSD slope (Spearman's $\rho = -0.41$, $p < 10^{-5}$; Fig. 2.2F). To further dissect the covariation among the predictor variables, we create multivariate linear models regressing for slope, using every combination of excitatory density, inhibitory density, and E:I density ratio (Table 2.2). We find that each variable alone produces models that are significantly better than null (constant-only) and with coefficients in the direction expected (positive for E, E:I ratio; negative for I), where the full model with all 3 predictors achieves the highest adjusted R2. However, inhibitory density in any combination produces the largest increase in adjusted R2. To assess whether model differences are significant, we performed bootstrap validation by building a distribution of adjusted R2 values from subsampling 25 random samples of the data 500 times, then comparing the distributions with paired-sample t-tests. We find that, while I improves model prediction the most, adding either E or E:I ratio significantly improves adjusted R2 compared to I-only (I < [I & E], $p = 0.0003$; I < [I & E:I], $p = 0.005$). Thus, we find that PSD slope significantly correlates with E:I ratio in the rat CA1, as measured by synapse density, though the effect is strongly driven by changes in inhibition.

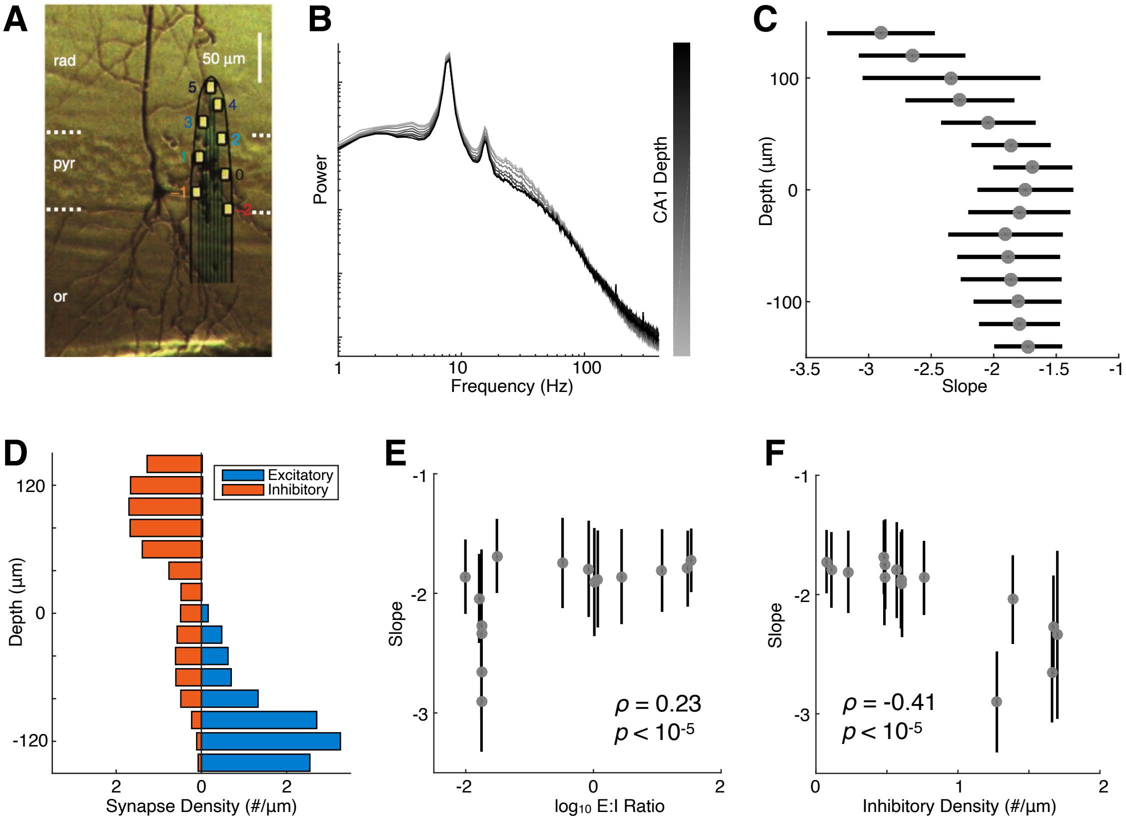

Figure 2.2: LFP-PSD slope varies with E:I synapse density ratio in rat CA1. (A) Example shank spanning across CA1 (rad: stratum radiatum; pyr: stratum pyramidale; or: stratum oriens; adapted from (Mizuseki et al., 2011)). (B) Example PSDs computed from electrodes along one recording shank. (C) Aggregate slope profile across depth, centered to the middle of pyramidal layer (0 μm) (horizontal bars denote standard deviation). (D) Excitatory (AMPA) and inhibitory (GABAA) synapse density varies across CA1 depth. (E and F) LFP-PSD slope correlates positively with E:I synapse density ratio (E) and negatively with GABAA density (F) (vertical bars denote standard deviation).

Theta-modulated cycles of excitation & inhibition

If LFP-PSD slope indeed tracks changes in the balance between excitation and inhibition, it should not only do so statically across space, but dynamically across time as well. Theta oscillation in the rat hippocampus reflects periodic bouts of excitation and inhibition (Buzsáki,

Table 2.2: Multivariate Linear Model Coefficients and R2 for Slope vs. E, I, and E:I Ratio. N/A indicates exclusion of predictor in model.

	Coefficients	R2				
Model	Constant	E	I	E:I	ordinary	adjusted
E	-1.985	0.085	N/A	N/A	0.027	0.026
I	-1.589	N/A	-0.451	N/A	0.223	0.222
E:I	-1.861	N/A	N/A	0.116	0.073	0.072
E & I	-1.460	-0.089	-0.548	N/A	0.243	0.241
E & E:I	-1.727	-0.128	N/A	0.208	0.090	0.088
I & E:I	-1.534	N/A	-0.590	-0.084	0.240	0.238
E, I & E:I	-1.474	-0.065	-0.575	-0.032	0.244	0.241

2002). Therefore, we posit that PSD slope would be steeper during the inhibitory phase of theta, and flatter during the excitatory phase. To test this, we use the same CA1 dataset as above, and divide each LFP recording into temporal segments of peak and trough based on theta phase (Fig. 2.3A; see Methods). Fast Fourier Transforms (FFTs) are computed from these short segments and averaged, showing distinctive slope differences (Fig. 2.3B). We find that, across all channels, PSD slope (30-50 Hz) during theta peaks were significantly more negative (steeper) than during theta troughs (paired t-test, $p < 10^{-5}$; Fig. 2.3C and 2.3D). On a single channel basis, we fit linear slopes to each short segment FFT, and found 844 out of 946 channels with significantly flatter slopes during troughs (2-sample t-test, $p < 10^{-5}$). From this we infer that theta troughs correspond to periods of excitation, which agrees with the biophysical view that negativity in the hippocampal LFP is due to depolarization of membrane potential (Buzsáki et al., 2012). Additionally, we observe that high-frequency (140-230 Hz) power – a surrogate for spiking activity and ripples in the hippocampus (Schomburg et al., 2012) – is higher during theta troughs than peaks, further indicating the correspondence between LFP troughs and windows of excitation (Fig. 2.3E). Taken together, we find evidence that PSD slope can dynamically track periods of excitation and inhibition facilitated by theta oscillations in the rat hippocampus.

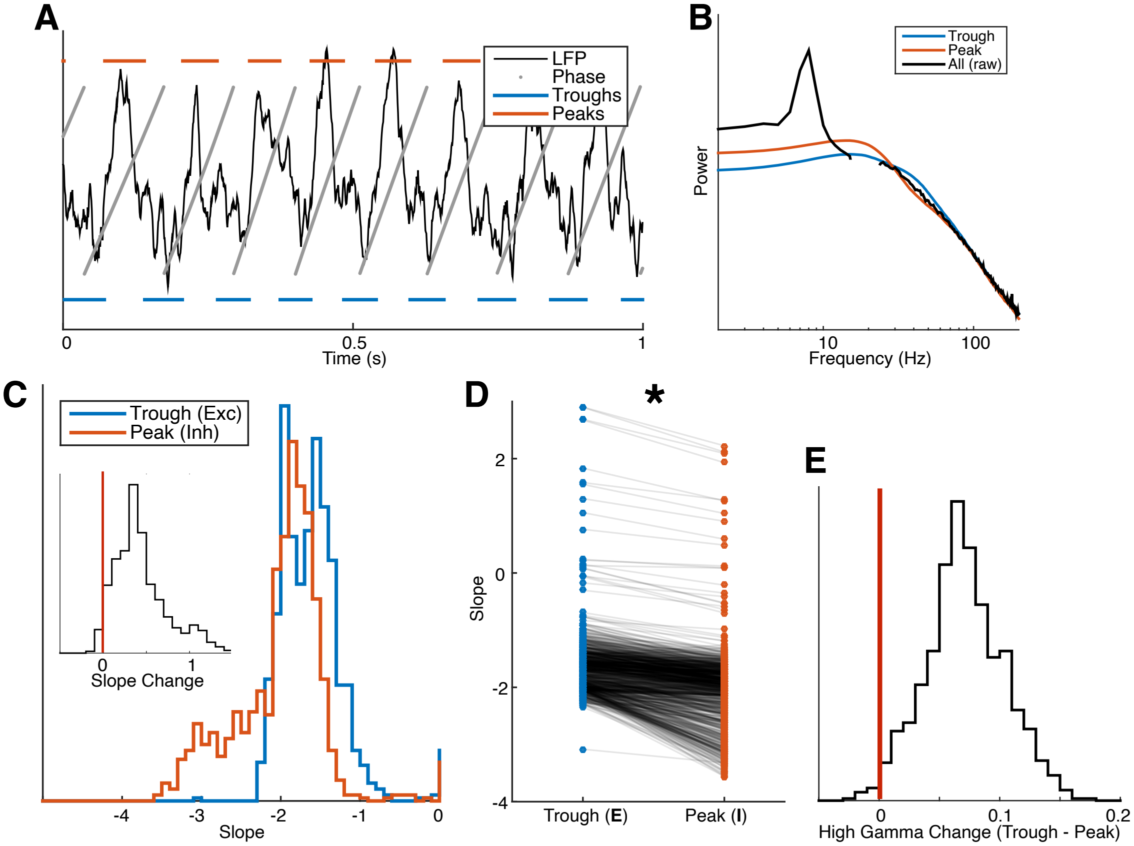

Figure 2.3: PSD slope tracks theta-modulated changes in E:I balance. (A) Schematic of how LFP segments are divided and binned based on theta phase. (B) Example PSD of a single channel over the entire recording (black, notch filter applied in beta range), and averages across all troughs (blue) and peaks (red) only. (C) Distribution of slope values shifts rightward (more positive) during theta troughs. Inset: distribution of difference in slope (trough minus peak) lies significantly above 0 (vertical red line). (D) Individual-channel comparison of slopes during theta troughs vs. peaks, each channel represented by a pair of connected dots showing nearly universally more negative slope during peaks compared to troughs (* $p < 10^{-5}$). (E) Distribution of difference (trough minus peak) in high frequency activity (HFA, 140-230 Hz) in all channels lies significantly above 0 (vertical red line), indicating an increase in high gamma power from peak to trough.

Propofol-induced increase in GABAA-mediated inhibition

Finally, having shown correlative evidence supporting the hypothesis, we aim to further test the simulation predictions through causal manipulations. Propofol is a general anesthetic that positively modulates the effect of GABA at GABAA receptors (Concas et al., 1991), effectively decreasing the global E:I ratio. Thus, we query another openly available dataset (http://www.neurotycho.org), in which electrocorticogram (ECoG) from macaques was recorded throughout sedation, to investigate whether ECoG-PSD slope reflects a decrease in E:I ratio induced via pharmacological manipulation (Yanagawa et al., 2013). PSDs are computed for all 128 recording channels per session, for awake resting and anesthetized conditions (Fig. 2.4A). We observe a significant decrease in PSD slope after onset of anesthesia for all 4 recording sessions (paired t-test, all $p < 10^{-5}$, Fig. 2.4B). The slope decrease is strongest in frontal and temporal electrodes (Fig. 2.4C), consistent with previous neuroimaging studies spatially locating propofol's region of effect (Zhang et al., 2010). Interestingly, electrodes in the precuneus region show increases in PSD slope during anesthesia instead, suggesting a gain of activity, perhaps due to its situation as a critical, core node within the default mode network (Utevsky et al., 2014). Finally, to calculate temporally precise demarcations of consciousness state changes, we estimate PSD slope in a time-resolved fashion by fitting over 1-second long sliding FFTs across the entire recording session. We find that PSD slope dynamically tracks the stability of brain state during awake resting, followed by a rapid push towards inhibition after injection that is consistent with propofol's time of onset (15-30 seconds), as well as the slow rebalancing during recovery from anesthesia (Fig. 2.4D). Unexpectedly, we also observe a rapid increase in slope, back to resting-state values, following the initial gain in inhibition, suggesting a global re-normalization process. Overall, we demonstrate that ECoG-PSD slope dynamically tracks propofol-induced gain in inhibition consistently across brain regions and time.

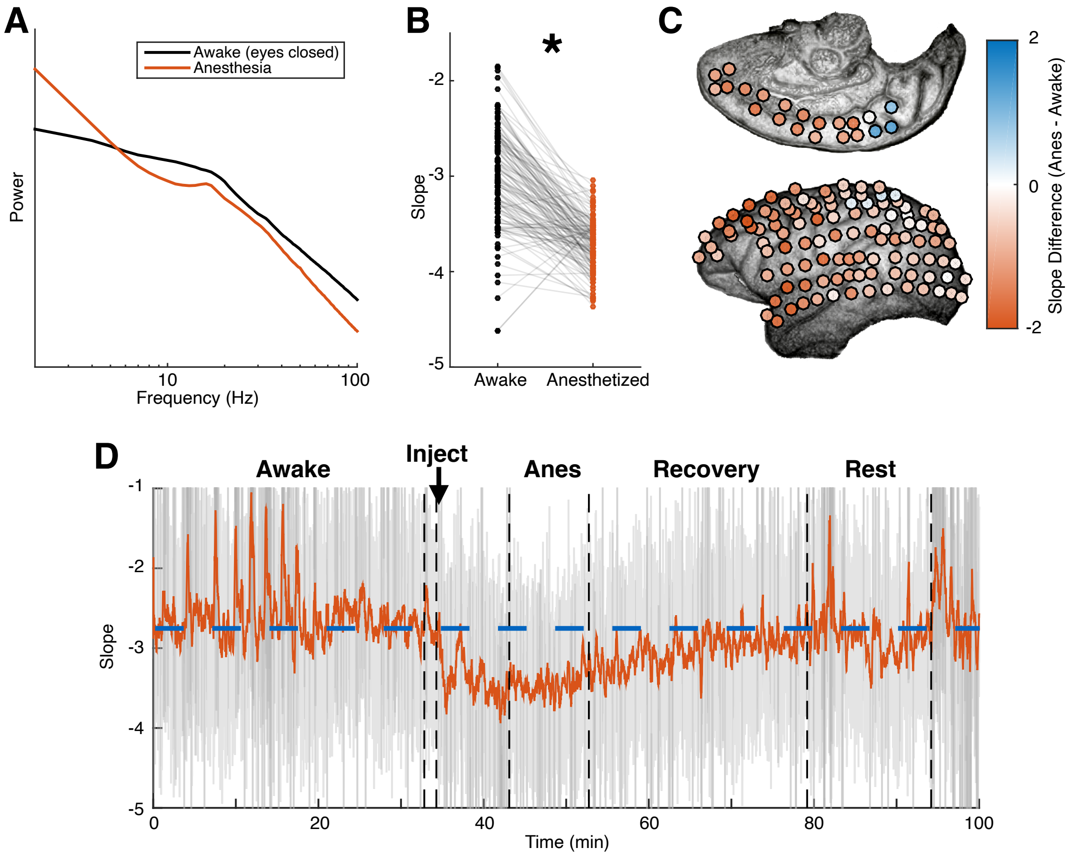

Figure 2.4: ECoG-PSD slope tracks propofol-induced global inhibition. (A) Average PSD across all channels during resting (black) and anesthetized (red) show distinct slope differences beyond 30 Hz. (B) Significant slope decrease is observed during anesthesia (pair t-test, * $p < 10^{-5}$). (C) Slope decrease is observed across most of cortex, most prominently in the frontal and temporal areas. Slope increase is observed exclusively in the precuneus. (D) Time-resolved estimate of PSD slope tracks, with fine temporal resolution, changes in brain state from awake to anesthetized (Anes), and as well as a slow recovery to baseline rest levels (marked by dashed blue line). Grey, unsmoothed; red, 15s smoothing window applied.

2.4 Discussion

Guided by predictions from our computational modeling results, our analyses of existing datasets from two mammalian species with different experimental manipulations and recording equipment demonstrate that information about local E:I ratio can be captured from the spectral representation of electrophysiological signals. Specifically, we show that LFP-PSD slope correlates with both anatomical E:I ratio—represented by changes in synaptic density ratio across CA1 layers—and dynamic E:I ratio as modulated by theta oscillation in the rat hippocampus. In addition, ECoG-PSD slope tracks the increase of inhibition in non-human primate brains induced by propofol, across brain regions and time. Evidence that spiking can be partially extracted from the broadband (2-250 Hz) or high gamma (>80 Hz) spectral power of meso-/macro-scale neural recordings (LFP, ECoG) provided an important link between local neuronal activity and the LFP, opening numerous avenues of research (Manning et al., 2009; Miller et al., 2009; Mukamel et al., 2005). In contrast to the copious literature regarding broadband/high gamma, much of the work on E:I balance has been limited to intracellular recordings, methods with limited temporal resolution, multiple single-unit recordings, or optogenetic manipulations. Given the broad and important role that E:I balance plays in neural computation, information transfer, and oscillatory and homeostatic mechanisms, the inability to easily measure E:I parameters at a large scale has hindered basic and clinical research. To this end, we develop a simple metric that can be applied at different intracranial recording scales, which can potentially be extended to extracranial EEG recordings, with profound implications for clinical and basic science research.

Limitations

There are several caveats in this study worth noting. Most notably is the underlying assumption that LFP and ECoG are solely composed of AMPA and GABAA synaptic currents. In reality, LFP reflects the integration of all ionic currents, including action potentials (Schomburg et al., 2012) – which shift the broadband/high gamma frequencies (Manning et al., 2009; Miller et al., 2009; Mukamel et al., 2005) – and slow glial currents (Buzsáki et al., 2012). The computational model also makes several assumptions, such as homogeneous-rate spiking and constant PSC waveforms, as well as excluding biophysical details like 3D arrangement of the spiking population. These factors will certainly influence the overall shape of the PSD, although it was shown that a linear combination of excitatory and inhibitory synaptic currents best approximates neuronal networks with 3D cellular morphology (Mazzoni et al., 2015). Additionally, such models have been used to capture the aforementioned broadband/high gamma relationship to spiking activity (Miller et al., 2009), a phenomenon that is also reproduced in our model through an overall (and equivalent) increase in firing rate from both excitatory and inhibitory populations.

Furthermore, although our computational model makes predictions that EI balance can be captured from the 1/f slope, we emphasize that our model assumes a linear independent summation of E and I currents that do not account for the fast-coupling or recurrent nature of cortical circuits. This assumption rests on the high-conductance state of cortical circuits over long recording lengths, effectively washing out stimulus-specific frequency response. So while our simple slope-fitting model captures significant variance in E:I ratio, the fact that the feedback engagement of E and I makes these two contributions inextricably linked suggests that more sophisticated models would perform better when the superposition assumption does not satisfy. In particular, previous works have shown that the amplitude of the power spectrum depends critically on this interaction in similar frequency ranges used in our analyses to infer E:I from the spectral slope, when considering time-inhomogeneous stimuli (Brunel & Wang, 2003; Mazzoni et al., 2008). Some methods have been proposed to estimate network parameters (including E:I ratio) when recurrent E:I interactions are taken into account (Barbieri et al., 2014). These methods are more complicated than, but complementary to, the model we propose, and they may be preferable when considering non-stationary, stimulus-evoked responses. Finally, because non-neural sources such as the amplifier, reference scheme, and ambient noise can affect spectral slope, slope-inferred E:I ratio should only be interpreted in the context of a comparative experimental design in which the relative E:I ratio can be interrogated in response to experimental manipulations or population differences, rather than ascribing meaning to the exact value of the slope itself. In particular, it has been shown that different referencing schemes, such as bipolar vs. common-average, have profound effects on the measured PSD slope (Shirhatti et al., 2016). In addition, we observe that

PSD slope of cortical ECoG is much more negative than that of CA1 LFP recordings, which, in turn, is lower than slopes produced by our LFP model, suggesting that anatomical differences and dendritic integration process all contribute to the measured slope (Lindén et al., 2010; Pettersen et al., 2014).

Power Law (1/f) Decay in Neural Recordings

Power law exponent (slope) changes of the PSD (“rotation”) have recently been observed in several empirical studies, linking it to changes in global awake and sleep states (He et al., 2010), age-related cognitive decline (Voytek & Knight, 2015; Voytek et al., 2015; Waschke et al., 2017) and visuomotor task-related activation (Podvalny et al., 2015). The 1/f power law nature of neural recordings has been interpreted within a self-organized criticality framework (Bak et al., 1987; He et al., 2010), with general anesthesia argued to alter the criticality of self-organized brain networks (Alonso et al., 2014). It has been shown, however, that power law statistics do not imply criticality in neuronal networks (Touboul & Destexhe, 2010), and the finding that neuronal activity exhibit power law statistics at all has been questioned (Bedard et al., 2006). Furthermore, many previous reports ignore or overlook the fact that PSD of neural recordings are not 1/f at all frequencies and do not have a constant power law exponent – both requirements in the self-organized criticality framework. Instead, LFP and ECoG PSDs often have relatively constant spectral power at low frequencies between 1-10 Hz, as well as different power law exponents at different frequencies. For example, ultra-low frequency region (<1 Hz) was posited to exhibit 1/f decay due to recurrent network activity (Chaudhuri et al., 2017), and power law in the very high frequency (>200 Hz) was shown to be a result of stochastic fluctuations in ion channels (Diba et al., 2004).

Our model and results reconcile the 1/f and low-frequency plateau observation by the simple fact that the spectral representation of synaptic currents (Lorentzian) takes on that shape (Fig. 2.1D), as others have noted before (Destexhe & Rudolph, 2004). In fact, previous works have modeled the Lorentzian form as due to the network propagation time constant of a recurrent excitatory population (Freeman & Zhai, 2009) and excitatory synaptic time constants coupled with dendritic filtering (Miller et al., 2009). However, recent evidence suggests that synaptic inhibition also plays a significant role in shaping the LFP time series (Telenczuk et al., 2017). As such, we infer that the balance between excitation and inhibition could be extracted from the extracellular field potential, though not from the polarity of the time series signal itself. Hence, we propose that slope changes in a particular frequency region (30-70 Hz) correspond to changes in E:I balance, while making no claims about other frequency regions, and our multivariate model in the CA1 analysis reveals that both inhibition alone and E:I ratio predict spectral slope better than excitation alone. Altogether, it follows that different processes may give rise to power law phenomenon at different temporal scales, hence different frequency ranges (Chaudhuri et al., 2017). Our observations here do not negate the criticality perspective, but reframes it in E:I terms, wherein constant E:I balancing is crucial for maintaining neuronal excitability at a critical state (Xue et al., 2014).

In summary, our results challenge the view that the relative contributions of EPSCs and IPSCs to electrophysiological signals cannot be readily inferred (Yizhar et al., 2011). We show that this limitation can be overcome using relatively simple metrics derived from meso- and macro-scale neural recordings, and that it can be easily applied retrospectively to existing data, opening new domains of inquiry and allowing for reanalyses within an E:I framework. Furthermore, our results provide insights into several ongoing research domains, such as possible contributors to the 1/f power law phenomenon often observed in field potential power spectra. By providing a new way for decoding the physiological information of the aggregate field potential, we can query brain states in novel ways, helping close the gap between cellular and cognitive neuroscience and increasing our ability to relate fundamental brain processes to behaviour and cognition as a result.

Acknowledgements

Chapter 2, in full, is a reprint of the material as it appears in the following manuscript published in *NeuroImage*: Gao, R., Peterson, E. J., & Voytek, B. (2017). **Inferring synaptic excitation/inhibition balance from field potentials.** The dissertation author was the primary investigator and author of this paper.

Bibliography

Alonso, L. M., Proekt, A., Schwartz, T. H., Pryor, K. O., Cecchi, G. A., & Magnasco, M. O. (2014). Dynamical criticality during induction of anesthesia in human ECoG recordings. Front. Neural Circuits, 8, 20.

Alvarez, F. P. & Destexhe, A. (2004). Simulating cortical network activity states constrained by intracellular recordings. Neurocomputing, 58-60, 285–290.

Atallah, B. V. & Scanziani, M. (2009). Instantaneous modulation of gamma oscillation frequency by balancing excitation with inhibition. Neuron, 62, 566–577.

Bak, P., Tang, C., & Wiesenfeld, K. (1987). Self-organized criticality: An explanation of the 1/f noise. Phys. Rev. Lett., 59, 381–384.

Barbieri, F., Mazzoni, A., Logothetis, N. K., Panzeri, S., & Brunel, N. (2014). Stimulus dependence of local field potential spectra: experiment versus theory. J. Neurosci., 34, 14589–14605.

Bedard, C., Kroeger, H., & Destexhe, A. (2006). Does the 1/f frequency scaling of brain signals reflect self-organized critical states? Phys. Rev. Lett., 97, 118102.

Brunel, N. & Wang, X.-J. (2003). What determines the frequency of fast network oscillations with irregular neural discharges? i. synaptic dynamics and excitation-inhibition balance. J. Neurophysiol., 90, 415–430.

Buzsáki, G. (2002). Theta oscillations in the hippocampus. Neuron, 33, 325–340.

Buzsáki, G., Anastassiou, C. A., & Koch, C. (2012). The origin of extracellular fields and currents–EEG, ECoG, LFP and spikes. Nat. Rev. Neurosci., 13, 407–420.

Chaudhuri, R., He, B. J., & Wang, X.-J. (2017). Random recurrent networks near criticality capture the broadband power distribution of human ECoG dynamics. Cereb. Cortex, 8, 1–13.

Concas, A., Santoro, G., Serra, M., Sanna, E., & Biggio, G. (1991). Neurochemical action of the general anaesthetic propofol on the chloride ion channel coupled with GABAA receptors. Brain Res., 542, 225–232.

Dani, V. S., Chang, Q., Maffei, A., Turrigiano, G. G., Jaenisch, R., & Nelson, S. B. (2005). Reduced cortical activity due to a shift in the balance between excitation and inhibition in a mouse model of rett syndrome. Proc. Natl. Acad. Sci. U. S. A., 102, 12560–12565.

Destexhe, A. & Rudolph, M. (2004). Extracting information from the power spectrum of synaptic noise. J. Comput. Neurosci., 17, 327–345.

Destexhe, A., Rudolph, M., Fellous, J. M., & Sejnowski, T. J. (2001). Fluctuating synaptic conductances recreate in vivo-like activity in neocortical neurons. Neuroscience, 107, 13–24.

Destexhe, A., Rudolph, M., & Paré, D. (2003). The high-conductance state of neocortical neurons in vivo. Nat. Rev. Neurosci., 4, 739–751.

Diba, K., Lester, H. A., & Koch, C. (2004). Intrinsic noise in cultured hippocampal neurons: experiment and modeling. J. Neurosci., 24, 9723–9733.

Freeman, W. J. & Zhai, J. (2009). Simulated power spectral density (PSD) of background electrocorticogram (ECoG). Cogn. Neurodyn., 3, 97–103.

González-Ramírez, L. R., Ahmed, O. J., Cash, S. S., Wayne, C. E., & Kramer, M. A. (2015). A biologically constrained, mathematical model of cortical wave propagation preceding seizure termination. PLoS Comput. Biol., 11, e1004065.

Haider, B., Schulz, D. P. A., Häusser, M., & Carandini, M. (2016). Millisecond coupling of local field potentials to synaptic currents in the awake visual cortex. Neuron, 90, 35–42.

He, B. J., Zempel, J. M., Snyder, A. Z., & Raichle, M. E. (2010). The temporal structures and functional significance of scale-free brain activity. Neuron, 66, 353–369.

Henry, M. E., Lauriat, T. L., Shanahan, M., Renshaw, P. F., & Jensen, J. E. (2011). Accuracy and stability of measuring GABA, glutamate, and glutamine by proton magnetic resonance spectroscopy: a phantom study at 4 tesla. J. Magn. Reson., 208, 210–218.

Legon, W., Punzell, S., Dowlati, E., Adams, S. E., Stiles, A. B., & Moran, R. J. (2016). Altered prefrontal Excitation/Inhibition balance and prefrontal output: Markers of aging in human memory networks. Cereb. Cortex, 26, 4315–4326.

Lim, S. & Goldman, M. S. (2013). Balanced cortical microcircuitry for maintaining information in working memory. Nat. Neurosci., 16, 1306–1314.

Lindén, H., Pettersen, K. H., & Einevoll, G. T. (2010). Intrinsic dendritic filtering gives low-pass power spectra of local field potentials. J. Comput. Neurosci., 29, 423–444.

Manning, J. R., Jacobs, J., Fried, I., & Kahana, M. J. (2009). Broadband shifts in local field potential power spectra are correlated with single-neuron spiking in humans. J. Neurosci., 29, 13613–13620.

Mariani, J., Coppola, G., Zhang, P., Abyzov, A., Provini, L., Tomasini, L., Amenduni, M., Szekely, A., Palejev, D., Wilson, M., Gerstein, M., Grigorenko, E. L., Chawarska, K., Pelphrey, K. A., Howe, J. R., & Vaccarino, F. M. (2015). FOXG1-Dependent dysregulation of GABA/Glutamate neuron differentiation in autism spectrum disorders. Cell, 162, 375–390.

Mariño, J., Schummers, J., Lyon, D. C., Schwabe, L., Beck, O., Wiesing, P., Obermayer, K., & Sur, M. (2005). Invariant computations in local cortical networks with balanced excitation and inhibition.

Mazzoni, A., Lindén, H., Cuntz, H., Lansner, A., Panzeri, S., & Einevoll, G. T. (2015). Computing the local field potential (LFP) from Integrate-and-Fire network models. PLoS Comput. Biol., 11, e1004584.

Mazzoni, A., Panzeri, S., Logothetis, N. K., & Brunel, N. (2008). Encoding of naturalistic stimuli by local field potential spectra in networks of excitatory and inhibitory neurons. PLoS Comput. Biol., 4, e1000239.

Megías, M., Emri, Z., Freund, T. F., & Gulyás, A. I. (2001). Total number and distribution of inhibitory and excitatory synapses on hippocampal CA1 pyramidal cells. Neuroscience, 102, 527–540.

Miller, K. J., Leuthardt, E. C., Schalk, G., Rao, R. P. N., Anderson, N. R., Moran, D. W., Miller, J. W., & Ojemann, J. G. (2007). Spectral changes in cortical surface potentials during motor movement. Journal of Neuroscience, 27, 2424–2432.

Miller, K. J., Sorensen, L. B., Ojemann, J. G., & den Nijs, M. (2009). Power-law scaling in the brain surface electric potential. PLoS Comput. Biol., 5, e1000609.

Mizuseki, K., Diba, K., Pastalkova, E., & Buzsáki, G. (2011). Hippocampal CA1 pyramidal cells form functionally distinct sublayers. Nat. Neurosci., 14, 1174–1181.

Mizuseki, K., Sirota, A., Pastalkova, E., & Buzsáki, G. (2009). Multi-unit recordings from the rat hippocampus made during open field foraging. Available online at: CRCNS. org.

Monier, C., Fournier, J., & Frégnac, Y. (2008). In vitro and in vivo measures of evoked excitatory and inhibitory conductance dynamics in sensory cortices. J. Neurosci. Methods, 169, 323–365.

Mukamel, R., Gelbard, H., Arieli, A., Hasson, U., Fried, I., & Malach, R. (2005). Coupling between neuronal firing, field potentials, and FMRI in human auditory cortex. Science, 309, 951–954.

Pettersen, K. H., Lindén, H., Tetzlaff, T., & Einevoll, G. T. (2014). Power laws from linear neuronal cable theory: power spectral densities of the soma potential, soma membrane current and single-neuron contribution to the EEG. PLoS Comput. Biol., 10, e1003928.

Peyrache, A., Dehghani, N., Eskandar, E. N., Madsen, J. R., Anderson, W. S., Donoghue, J. A., Hochberg, L. R., Halgren, E., Cash, S. S., & Destexhe, A. (2012). Spatiotemporal dynamics of neocortical excitation and inhibition during human sleep. Proc. Natl. Acad. Sci. U. S. A., 109, 1731–1736.

Podvalny, E., Noy, N., Harel, M., Bickel, S., Chechik, G., Schroeder, C. E., Mehta, A. D., Tsodyks, M., & Malach, R. (2015). A unifying principle underlying the extracellular field potential spectral responses in the human cortex. J. Neurophysiol., 114, 505–519.

Pospischil, M., Piwkowska, Z., Bal, T., & Destexhe, A. (2009). Extracting synaptic conductances from single membrane potential traces. Neuroscience, 158, 545–552.

Ray, S. & Maunsell, J. H. R. (2011). Network rhythms influence the relationship between spike-triggered local field potential and functional connectivity. J. Neurosci., 31, 12674–12682.

Reinhold, K., Lien, A. D., & Scanziani, M. (2015). Distinct recurrent versus afferent dynamics in cortical visual processing. Nat. Neurosci., 18, 1789–1797.

Rubenstein, J. L. R. & Merzenich, M. M. (2003). Model of autism: increased ratio of excitation/inhibition in key neural systems. Genes Brain Behav., 2, 255–267.

Salinas, E. & Sejnowski, T. J. (2001). Correlated neuronal activity and the flow of neural information. Nat. Rev. Neurosci., 2, 539–550.

Schomburg, E. W., Anastassiou, C. A., Buzsaki, G., & Koch, C. (2012). The spiking component of oscillatory extracellular potentials in the rat hippocampus.

Shirhatti, V., Borthakur, A., & Ray, S. (2016). Effect of reference scheme on power and phase of the local field potential. Neural Comput., 28, 882–913.

Symonds, C. (1959). EXCITATION AND INHIBITIION IN EPILEPSY.

Telenczuk, B., Dehghani, N., Le Van Quyen, M., Cash, S. S., Halgren, E., Hatsopoulos, N. G., & Destexhe, A. (2017). Local field potentials primarily reflect inhibitory neuron activity in human and monkey cortex. Sci. Rep., 7.

Touboul, J. & Destexhe, A. (2010). Can Power-Law scaling and neuronal avalanches arise from stochastic dynamics?

Turrigiano, G. G. & Nelson, S. B. (2004). Homeostatic plasticity in the developing nervous system.

Uhlhaas, P. J. & Singer, W. (2010). Abnormal neural oscillations and synchrony in schizophrenia. Nat. Rev. Neurosci., 11, 100–113.

Utevsky, A. V., Smith, D. V., & Huettel, S. A. (2014). Precuneus is a functional core of the Default-Mode network.

Vogels, T. P. & Abbott, L. F. (2009). Gating multiple signals through detailed balance of excitation and inhibition in spiking networks. Nat. Neurosci., 12, 483–491.

Voytek, B. & Knight, R. T. (2015). Dynamic network communication as a unifying neural basis for cognition, development, aging, and disease. Biol. Psychiatry, 77, 1089–1097.

Voytek, B., Kramer, M. A., Case, J., Lepage, K. Q., Tempesta, Z. R., Knight, R. T., & Gazzaley, A. (2015). Age-Related changes in 1/f neural electrophysiological noise. J. Neurosci., 35, 13257–13265.

Waschke, L., Wöstmann, M., & Obleser, J. (2017). States and traits of neural irregularity in the age-varying human brain.

Xue, M., Atallah, B. V., & Scanziani, M. (2014). Equalizing excitation-inhibition ratios across visual cortical neurons. Nature, 511, 596–600.

Yanagawa, T., Chao, Z. C., Hasegawa, N., & Fujii, N. (2013). Large-scale information flow in conscious and unconscious states: an ECoG study in monkeys. PLoS One, 8, e80845.

Yizhar, O., Fenno, L. E., Prigge, M., Schneider, F., Davidson, T. J., O'Shea, D. J., Sohal, V. S., Goshen, I., Finkelstein, J., Paz, J. T., Stehfest, K., Fudim, R., Ramakrishnan, C., Huguenard, J. R., Hegemann, P., & Deisseroth, K. (2011). Neocortical excitation/inhibition balance in information processing and social dysfunction. Nature, 477, 171–178.

Zhang, H., Wang, W., Zhao, Z., Ge, Y., Zhang, J., Yu, D., Chai, W., Wu, S., & Xu, L. (2010). The action sites of propofol in the normal human brain revealed by functional magnetic resonance imaging. Anat. Rec., 293, 1985–1990.

Chapter 3

Neuronal timescales are functionally dynamic and shaped by cortical microarchitecture

Abstract

Complex cognitive functions such as working memory and decision-making require information maintenance over seconds to years, from transient sensory stimuli to long-term contextual cues. While theoretical accounts predict the emergence of a corresponding hierarchy of neuronal timescales, direct electrophysiological evidence across the human cortex is lacking. Here, we infer neuronal timescales from invasive intracranial recordings. Timescales increase along the principal sensorimotor-to-association axis across the entire human cortex, and scale with single-unit timescales within macaques. Cortex-wide transcriptomic analysis shows direct alignment between timescales and expression of excitation- and inhibition-related genes, as well as genes specific to voltage-gated transmembrane ion transporters. Finally, neuronal timescales are functionally dynamic: prefrontal cortex timescales expand during working memory maintenance

and predict individual performance, while cortex-wide timescales compress with aging. Thus, neuronal timescales follow cytoarchitectonic gradients across the human cortex, and are relevant for cognition in both short- and long-terms, bridging microcircuit physiology with macroscale dynamics and behavior.

3.1 Introduction

Human brain regions are broadly specialized for different aspects of behavior and cognition, and the temporal dynamics of neuronal populations across the cortex are thought to be an intrinsic property (i.e., neuronal timescale) that enables the representation of information over multiple durations in a hierarchically embedded environment (Kiebel et al., 2008). For example, primary sensory neurons are tightly coupled to changes in the environment, firing rapidly to the onset and removal of a stimulus, and showing characteristically short intrinsic timescales (Ogawa & Komatsu, 2010; Runyan et al., 2017). In contrast, neurons in cortical association (or transmodal) regions, such as the prefrontal cortex (PFC), can sustain their activity for many seconds when a person is engaged in working memory (Zylberberg & Strowbridge, 2017), decision-making (Gold & Shadlen, 2007), and hierarchical reasoning (Sarafyazd & Jazayeri, 2019). This persistent activity in the absence of immediate sensory stimuli reflects longer neuronal timescales, which is thought to result from neural attractor states (Wang, 2002; Wimmer et al., 2014) shaped by NMDA-mediated recurrent excitation and fast feedback inhibition (Wang, 1999, 2008), with contributions from other synaptic and cell-intrinsic properties (Duarte & Morrison, 2019; Gjorgjieva et al., 2016). How connectivity and various cellular properties combine to shape neuronal dynamics across the cortex remains an open question.

Anatomical connectivity measures based on tract tracing data, such as laminar feedforward vs. feedback projection patterns, have classically defined a hierarchical organization of the cortex (Felleman & Van Essen, 1991; Hilgetag & Goulas, 2020; Vezoli et al., 2020). Recent studies have also shown that variations in many microarchitectural features follow continuous and coinciding gradients along a sensory-to-association axis across the cortex, including cortical thickness, cell density, and distribution of excitatory and inhibitory neurons (Huntenburg et al., 2018; Wang, 2020). In particular, grey matter myelination (Glasser & Van Essen, 2011)—a non-invasive proxy of anatomical hierarchy consistent with laminar projection data—varies with the expression of genes related to microcircuit function in the human brain, such as NMDA receptor and inhibitory cell-type marker genes (Burt et al., 2018). Functionally, specialization of the human cortex, as well as structural and functional connectivity (Margulies et al., 2016), also follow similar macroscopic gradients. Moreover, in addition to the broad differentiation between sensory and association cortices, there is evidence for an even finer hierarchical organization within the frontal cortex (Sarafyazd & Jazayeri, 2019). For example, the anterior-most parts of the PFC are responsible for long timescale goal-planning behavior (Badre & D'Esposito, 2009; Voytek et al., 2015a), while healthy aging is associated with a shift in these gradients such that older adults become more reliant on higher-level association regions to compensate for altered lower-level cortical functioning (Davis et al., 2008).

Despite convergent observations of cortical gradients in structural features and cognitive specialization, there is no direct evidence for a similar gradient of neuronal timescales across the human cortex. Such a gradient of neuronal dynamics is predicted to be a natural consequence of macroscopic variations in synaptic connectivity and microarchitectural features (Chaudhuri et al., 2015; Duarte et al., 2017; Huang & Doiron, 2017; Huntenburg et al., 2018; Wang, 2020), and would be a primary candidate for how functional specialization emerges as a result of hierarchical temporal processing (Kiebel et al., 2008). Single-unit recordings in rodents and non-human primates demonstrated a hierarchy of timescales that increase, or lengthen, progressively along a posterior-to-anterior axis (Dotson et al., 2018; Murray et al., 2014; Runyan et al., 2017; Wasmuht et al., 2018), while intracranial recordings and functional neuroimaging data collected during perceptual and cognitive tasks suggest likewise in humans (Baldassano et al., 2017; Honey et al., 2012; Lerner et al., 2011; Watanabe et al., 2019). However, these data are either sparsely sampled across the cortex or do not measure neuronal activity at the cellular and synaptic level directly, prohibiting the full construction of an electrophysiological timescale gradient across the human cortex. As a result, while whole-cortex data of transcriptomic and anatomical variations exist, we cannot take advantage of them to dissect the contributions of synaptic, cellular, and circuit connectivity in shaping fast neuronal timescales, nor ask whether regional timescales are dynamic and relevant for human cognition.

Here, we combine several publicly available datasets to infer neuronal timescales from invasive human electrocorticography (ECoG) recordings and relate them to whole-cortex transcriptomic and anatomical data, as well as probe their functional relevance during behavior (Figure 3.1A for schematic of study; Table 3.1 and 3.2 for dataset information). Unless otherwise specified, (neuronal) timescale in the following sections refers to ECoG-derived timescales, which are more reflective of fast synaptic and transmembrane current timescales than single-unit or population spiking timescales (Figure 3.1A, left box), though we demonstrate in macaques a close correspondence between the two. In humans, neuronal timescales increase along the principal sensorimotor-to-association axis across the cortex and align with macroscopic gradients of grey matter myelination (T1w/T2w ratio) and synaptic receptor and ion channel gene expression. Finally, we find that human prefrontal cortex timescales expand during working memory maintenance and predict individual performance, while cortex-wide timescales compress with aging. Thus, neuronal timescales follow cytoarchitectonic gradients across the human cortex, and are relevant for cognition in both short- and long-terms, bridging microcircuit physiology with macroscale dynamics and behavior.

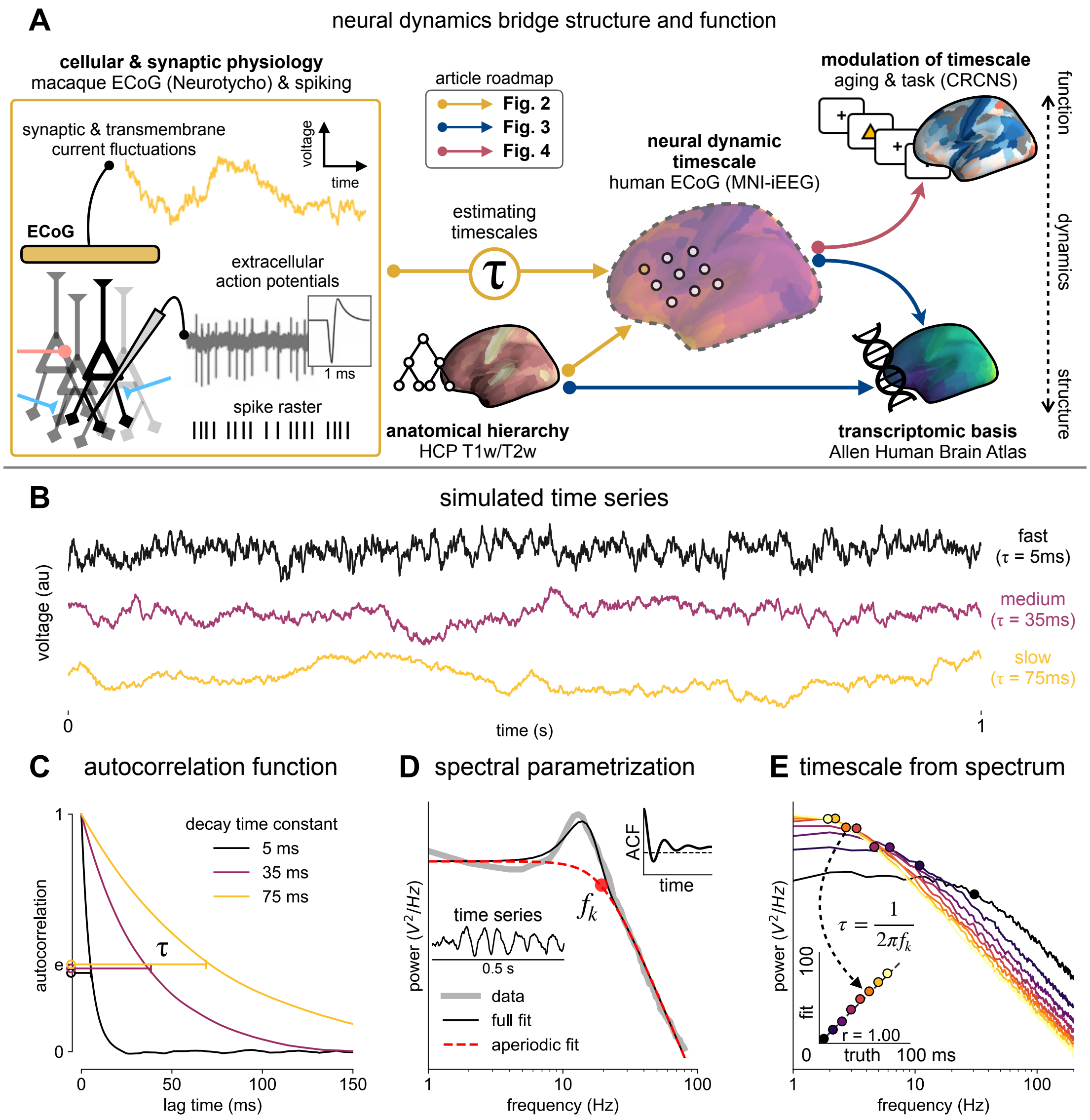

Figure 3.1: Schematic of study and timescale inference technique. (A) in this study, we infer neuronal timescales from intracranial field potential recordings, which reflect integrated synaptic and transmembrane current fluctuations over large neural populations (Buzsáki et al., 2012). Combining multiple open-access datasets (Table 3.1), we link timescales to known human anatomical hierarchy, dissect its cellular and physiological basis via transcriptomic analysis, and demonstrate its functional modulation during behavior and through aging. (B) simulated time series, and their (C) autocorrelation functions (ACF), with increasing (longer) decay time constant, τ (which neuronal timescale is defined to be). (D) example macaque ECoG power spectral density (PSD) showing the aperiodic component fit (red dashed), and the "knee frequency" at which power drops off (f_k, red circle; insets: time series and ACF). (E) estimation of timescale from PSDs of simulated time series in (B), where the knee frequency, f_k, is converted to timescale, τ, via the embedded equation (inset: correlation between ground truth and estimated timescale values).

3.2 Results

Neuronal timescale can be inferred from the frequency domain

Neural time series often exhibit time-lagged correlation (i.e., autocorrelation), where future values are partially predictable from past values, and predictability decreases with increasing time lags. For demonstration, we simulate the aperiodic (non-rhythmic) component of ECoG recordings by convolving Poisson population spikes with exponentially-decaying synaptic kernels with varying decay constant (Figure 3.1B). Empirically, the degree of self-similarity is characterized by the autocorrelation function (ACF), and "timescale" is defined as the time constant (τ) of an exponential decay function ($e^{\frac{-t}{\tau}}$) fit to the ACF, i.e., the time it takes for the autocorrelation to decrease by a factor of e (Figure 3.1C).

Equivalently, we can estimate timescale in the frequency domain from the power spectral density (PSD). PSDs of neural time series often follow a Lorentzian function of the form $\frac{1}{f_k^2+f^2}$, where power is approximately constant until the "knee frequency" (f_k, Figure 3.1D), then decays following a power law. This approach is similar to the one presented in (Chaudhuri et al., 2017), but here we further allow the power law exponent (fixed at 2 in the equation above) to be a free parameter representing variable scale-free activity (He et al., 2010; Miller et al., 2009; Podvalny et al., 2015; Voytek et al., 2015b). We also simultaneously parameterize oscillatory components as Gaussians peaks, allowing us to remove their effect on the power spectrum, providing more accurate estimates of the knee frequency. From the knee frequency of the aperiodic component, neural timescale (decay constant) can then be computed exactly as $\tau = \frac{1}{2\pi f_k}$.

Compared to fitting exponential decay functions in the time domain, e.g., (Murray et al., 2014)—which can be biased even without the presence of additional components (Zeraati et al., 2020)—the frequency domain approach is advantageous when a variable power law exponent and strong oscillatory components are present, as is often the case for neural signals (example of real data in Figure 3.1D). While the oscillatory component can corrupt naive measurement of τ as time for the ACF to reach 1/e (Figure 3.1D, inset), it can be more easily accounted for and removed in the frequency domain as Gaussian-like peaks. This is especially important considering neural oscillations with non-stationary frequencies. For example, a broad peak in the power spectrum (e.g., ∼10Hz in bandwidth in Figure 3.1D) represents drifts in the oscillation frequency over time, which is easily accounted for with a single Gaussian, but requires multiple cosine terms to capture well in the autocorrelation. Therefore, in this study, we apply spectral parameterization to extract timescales from intracranial recordings (Donoghue et al., 2020). We validate this approach on PSDs computed from simulated neural time series and show that the extracted timescales closely match their ground-truth values (Figure 3.1E).

Timescales follow anatomical hierarchy and are 10x faster than spiking timescales

Applying this technique, we infer a continuous gradient of neuronal timescales across the human cortex by analyzing a large dataset of human intracranial (ECoG) recordings of task-free brain activity (Frauscher et al., 2018a). The MNI-iEEG dataset contains 1 minute of resting state data across 1772 channels from 106 patients (13-62 years old, 48 females) with variable coverages, recorded using either surface strip/grid or stereoEEG electrodes, and cleaned of visible artifacts. Figure 3.2A shows example data traces along the cortical hierarchy with increasing timescales estimated from their PSDs (Figure 3.2B; circles denote fitted knee frequency). Timescales from individual channels were extracted and projected from MNI coordinates onto the left hemisphere of HCP-MMP1.0 surface parcellation (Glasser et al., 2016) for each patient using a Gaussian-weighted mask centered on each electrode. While coverage is sparse and idiosyncratic in individual patients, it does not vary as a function of age, and when pooling across the entire population, 178 of 180 parcels have at least one patient with an electrode within 4mm (Figure 3.5A-F).

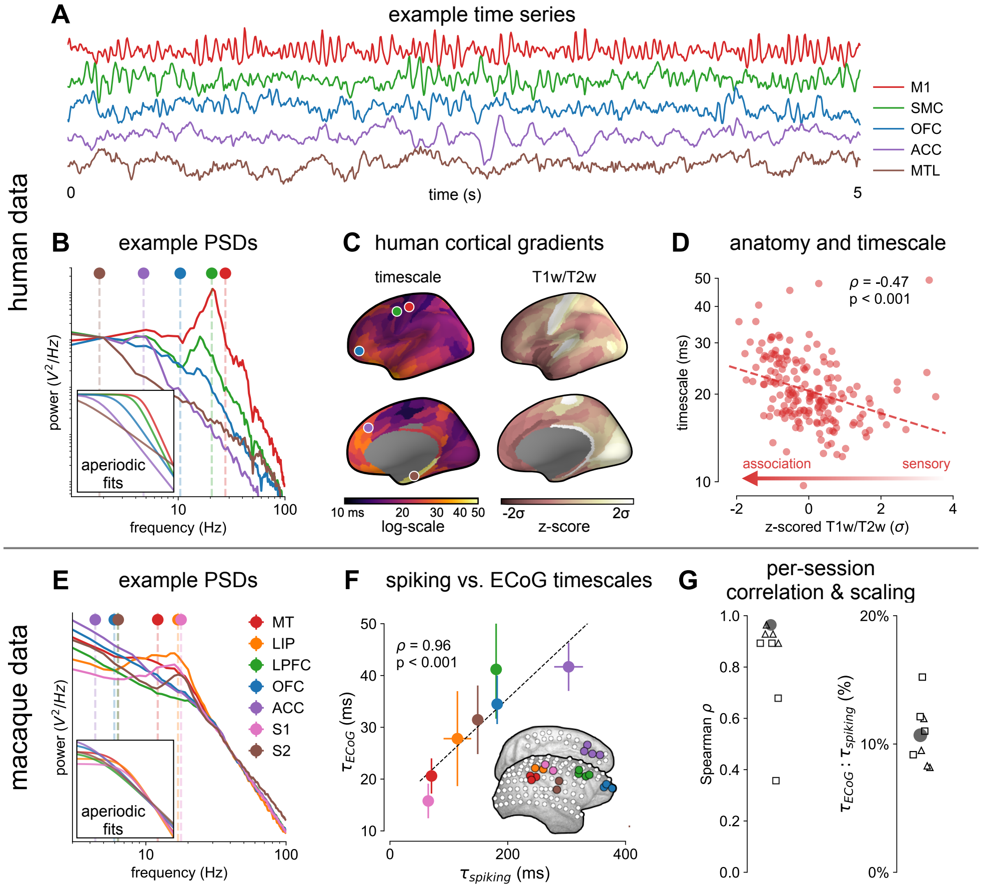

Figure 3.2: Timescale increases along the anatomical hierarchy in humans and macaques. (A) example time series from 5 electrodes along the human cortical hierarchy (M1: primary motor cortex; SMC: supplementary motor cortex; OFC: orbitofrontal cortex; ACC: anterior cingulate cortex; MTL: medial temporal lobe), and (B) their corresponding PSDs computed over 1 minute. Circle and dashed line indicate the knee frequency for each PSD, derived from the aperiodic component fits (inset). Data: MNI-iEEG database, N = 106 participants. (C) human cortical timescale gradient (left) falls predominantly along the rostrocaudal axis, similar to T1w/T2w ratio (right; z-scored, in units of standard deviation). Colored dots show electrode locations of example data. (D) neuronal timescales are negatively correlated with cortical T1w/T2w, thus increasing along the anatomical hierarchy from sensory to association regions (Spearman correlation; p-value corrected for spatial autocorrelation, Figure 3.6A-C). (E) Example PSDs from macaque ECoG recordings, similar to (B) (LIP: lateral intraparietal cortex; LPFC: lateral prefrontal cortex; S1 & S2: primary and secondary somatosensory cortex). PSDs are averaged over electrodes within each region (inset of (F)). Data: Neurotycho, N = 8 sessions from 2 animals. (F) macaque ECoG timescales track published single-unit spiking timescales (Murray et al., 2014) in corresponding regions (error bars represent mean±s.e.m). Inset: ECoG electrode map of one animal and selected electrodes for comparison. (G) ECoG-derived timescales are consistently correlated to (left), and ∼10 times faster than (right), single-unit timescales across individual sessions. Hollow markers: individual sessions; shapes: animals; circles: grand average from (F).

Across the human cortex, timescales of fast electrophysiological dynamics (∼10-50 ms) predominantly follow a rostrocaudal gradient (Figure 3.2C, circles denote location of example data from 2A). Consistent with numerous accounts of a principal cortical axis spanning from primary sensory to association regions (Hilgetag & Goulas, 2020; Margulies et al., 2016; Wang, 2020), timescales are shorter in sensorimotor and early visual areas, and longer in association regions, especially cingulate, ventral/medial frontal, and medial temporal regions (Figure 3.5G shows further pooling into 21 labeled macro-regions). We then compare the timescale gradient to the average T1w/T2w map from the Human Connectome Project, which captures grey matter myelination and indexes the proportion of feedforward vs. feedback connections between cortical regions, thus acting as a non-invasive proxy of connectivity-based anatomical hierarchy (Glasser & Van Essen, 2011; Burt et al., 2018). We find that neuronal timescales are negatively correlated with T1w/T2w across the entire cortex (Figure 3.2D, $\rho = -0.47$, $p < 0.001$; corrected for spatial autocorrelation (SA), see Materials and Methods and Figure 3.6A-C for a comparison of correction methods), such that timescales are shorter in more heavily myelinated (i.e., lower-level, sensory) regions. Timescales are also positively correlated with cortical thickness (Figure 3.7, $\tau = 0.37$, $p = 0.035$)—another index of cortical hierarchy that is itself anti-correlated with T1w/T2w. Thus, we observe that neuronal timescales lengthen along the human cortical hierarchy, from sensorimotor to association regions.

While surface ECoG recordings offer much broader spatial coverage than extracellular single-unit recordings, they are fundamentally different signals: ECoG and field potentials largely reflect integrated synaptic and other transmembrane currents across many neuronal and glial cells, rather than putative action potentials from single neurons (Buzsáki et al., 2012) (Figure 3.1A, yellow box). Considering this, we ask whether timescales measured from ECoG in this study (τ_{ECoG}) are related to single-unit spiking timescales along the cortical hierarchy ($\tau_{spiking}$). To test this, we extract neuronal timescales from task-free ECoG recordings in macaques (Nagasaka et al., 2011) and compare them to a separate dataset of single-unit spiking timescales from a different group of macaques (Murray et al., 2014) (see Figure 3.8 for electrode locations). Consistent with $\tau_{spiking}$ estimates (Murray et al., 2014; Wasmuht et al., 2018), τ_{ECoG} also increase along the macaque cortical hierarchy. While there is a strong correspondence between spiking and ECoG timescales (Figure 3.2F; $\rho = 0.96$, $p < 0.001$)—measured from independent datasets—across the macaque cortex, τ_{ECoG} are $\sim$10 times faster than $\tau_{spiking}$ and are conserved across individual sessions (Figure 3.2G). This suggests that neuronal spiking and transmembrane currents have distinct but related timescales of fluctuations, and that both are hierarchically organized along the primate cortex.

Synaptic and ion channel genes shape timescales of neuronal dynamics

Next, we identify potential cellular and synaptic mechanisms underlying timescale variations across the human cortex. Theoretical accounts posit that NMDA-mediated recurrent excitation coupled with fast inhibition (Chaudhuri et al., 2015; Wang, 1999, 2008), as well as cell-intrinsic properties (Duarte & Morrison, 2019; Gjorgjieva et al., 2016; Koch et al., 1996), are crucial for shaping neuronal timescales. While in vitro and in vivo studies in model organisms (van Vugt et al., 2020; Wang et al., 2013) can test these hypotheses at the single-neuron level, causal manipulation and large-scale recording of neuronal networks embedded in the human brain is severely limited. Here, we apply an approach analogous to multimodal single-cell profiling (Bomkamp et al., 2019) and examine the transcriptomic basis of neuronal dynamics at the macroscale.

Leveraging whole-cortex interpolation of the Allen Human Brain Atlas bulk mRNA expression (Hawrylycz et al., 2012; Gryglewski et al., 2018), we project voxel-wise expression maps onto the HCP-MMP1.0 surface parcellation, and find that the neuronal timescale gradient overlaps with the dominant axis of gene expression (i.e., 1st principal component of 2429 brain-related genes) across the human cortex (Figure 3.3A, $\rho = -0.60$, $p < 0.001$; see Figure 3.9 for similar results with all 18114 genes). Consistent with theoretical predictions (Figure 3.3B), timescales significantly correlate with the expression of genes encoding for NMDA (GRIN2B) and GABA-A (GABRA3) receptor subunits, voltage-gated sodium (SCN1A) and potassium (KCNA3) ion channel subunits, as well as inhibitory cell-type markers (parvalbumin, PVALB), and genes previously identified to be associated with single-neuron membrane time constants (PRR5) (Bomkamp et al., 2019) (all Spearman correlations corrected for spatial autocorrelation in gradients).

More specifically, in vitro electrophysiological studies have shown that, for example, increased expression of receptor subunit 2B extends the NMDA current time course (Flint et al., 1997), while 2A expression shortens it (Monyer et al., 1994). Similarly, the GABA-A receptor time constant lengthens with increasing a3:a1 subunit ratio (Eyre et al., 2012). We show that these relationships are recapitulated at the macroscale, where neuronal timescales positively correlate with GRIN2B and GABRA3 expression, and negatively correlate with GRIN2A and GABRA1 (Figure 3.3C). These results demonstrate that timescales of neural dynamics depend on specific receptor subunit combinations with different (de)activation timescales (Duarte et al., 2017; Gjorgjieva et al., 2016), in addition to broad excitation-inhibition interactions (Gao et al., 2017; Wang, 2002, 2020). Notably, almost all genes related to voltage-gated sodium and potassium ion channel alpha-subunits—the main functional subunits—are correlated with timescale, while all inhibitory cell-type markers except parvalbumin have strong positive associations with timescale (Figure 3.3C and 3.10).

Figure 3.3: Timescale gradient is linked to expression of genes related to synaptic receptors and transmembrane ion channels across the human cortex. (A) timescale gradient follows the dominant axis of gene expression variation across the cortex (z-scored PC1 of 2429 brain-specific genes, arbitrary direction). (B) timescale gradient is significantly correlated with expression of genes known to alter synaptic and neuronal membrane time constants, as well as inhibitory cell-type markers, but (C) members within a gene family (e.g., NMDA receptor subunits) can be both positively and negatively associated with timescales, consistent with predictions from in-vitro studies. (D) macroscale timescale-transcriptomic correlation captures association between RNA-sequenced expression of the same genes and single-cell timescale properties fit to patch clamp data from two studies, and the correspondence improves for genes (separated by quintiles) that are more strongly correlated with timescale (solid: N = 170 (Tripathy et al., 2017), dashed: N = 4168 genes (Bomkamp et al., 2019); horizontal lines: correlation across all genes from the two studies, $\rho = 0.36$ and 0.25, $p < 0.001$ for both). (E) T1w/T2w gradient is regressed out from timescale and gene expression gradients, and a partial least squares (PLS) model is fit to the residual maps. Genes with significant PLS weights (filled blue boxes) compared to SA-preserved null distributions are submitted for gene ontology enrichment analysis (GOEA), returning a set of significant GO terms that represent functional gene clusters (filled green boxes). (F) enriched genes are primarily linked to potassium and chloride transmembrane transporters, and GABA-ergic synapses; genes specifically with strong negative associations further over-represent transmembrane ion exchange mechanisms, especially voltage-gated potassium and cation transporters. Branches indicate GO items that share higher-level (parent) items, e.g., voltage-gated cation channel activity is a child of cation channel activity in the Molecular Functions (MF) ontology, and both are significantly associated with timescale. Color of lines indicate curated ontology (BP - Biological Process, CC - Cellular Components, or MF). Dotted, dashed, and solid lines correspond to analysis performed using all genes or only those with positive or negative PLS weights. Spatial correlation p-values in (A-C) are corrected for spatial autocorrelation (see Materials and Methods; asterisks in (B,D) indicate $p < 0.05$, 0.01, 0.005, and 0.001 respectively; filled circles in (C,D) indicate $p < 0.05$).

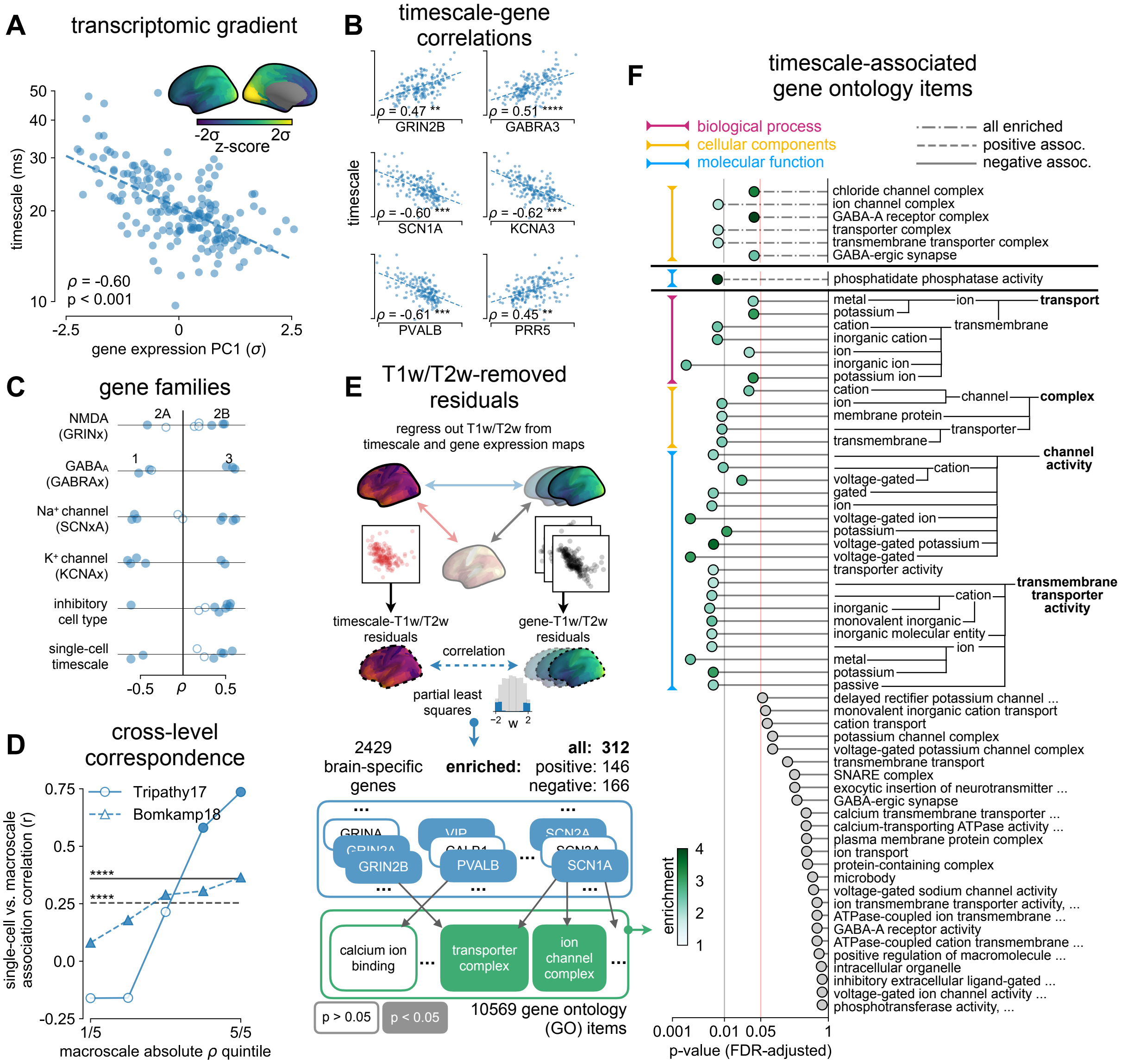
A
transcriptomic gradient
timescale (ms)
50
40
30
20
10
-2σ
2σ
z-score
ρ = -0.60
p < 0.001
-2.5
0
2.5
gene expression PC1 (σ)
B
timescale-gene correlations
timescale
ρ = 0.47 **
GRIN2B
ρ = 0.51 ****
GABRA3
ρ = -0.60 ***
SCN1A
ρ = -0.62 ***
KCNA3
ρ = -0.61 ***
PVALB
ρ = 0.45 **
PRR5
C
gene families
NMDA (GRINx)
2A
2B
GABAA (GABRAx)
1
3
Na⁺ channel (SCNxA)
K⁺ channel (KCNAx)
inhibitory cell type
single-cell timescale
-0.5
ρ
0.5
D
cross-level correspondence
single-cell vs. macroscale association correlation (r)
0.75
0.5
0.25
0.0
-0.25
Tripathy17
Bomkamp18
****
****
1/5
5/5
macroscale absolute ρ quintile
E
T1w/T2w-removed residuals
regress out T1w/T2w from timescale and gene expression maps
timescale-T1w/T2w residuals
gene-T1w/T2w residuals
correlation
partial least squares
-2
w
2
2429 brain-specific genes
enriched:
all: 312
positive: 146
negative: 166
GRIN2B
PVALB
SCN1A
calcium ion binding
transporter complex
ion channel complex
p > 0.05
p < 0.05
10569 gene ontology (GO) items
F
timescale-associated gene ontology items
biological process
cellular components
molecular function
all enriched
positive assoc.
negative assoc.
chloride channel complex
ion channel complex
GABA-A receptor complex
transporter complex
transmembrane transporter complex
GABA-ergic synapse
phosphatidate phosphatase activity
metal
potassium
ion
transport
cation
transmembrane
inorganic cation
ion
inorganic ion
potassium ion
cation
ion
channel
complex
membrane protein
transporter
transmembrane
channel activity
cation
voltage-gated
gated
ion
voltage-gated ion
potassium
voltage-gated potassium
voltage-gated
transporter activity
transmembrane transporter activity
cation
inorganic
monovalent inorganic
inorganic molecular entity
ion
metal
potassium
passive
delayed rectifier potassium channel ...
monovalent inorganic cation transport
cation transport
potassium channel complex
voltage-gated potassium channel complex
transmembrane transport
SNARE complex
exocytic insertion of neurotransmitter ...
GABA-ergic synapse
calcium transmembrane transporter ...
calcium-transporting ATPase activity ...
plasma membrane protein complex
ion transport
protein-containing complex
microbody
voltage-gated sodium channel activity
ion transmembrane transporter activity, ...
ATPase-coupled ion transmembrane ...
GABA-A receptor activity
ATPase-coupled cation transmembrane ...
positive regulation of macromolecule ...
intracellular organelle
inhibitory extracellular ligand-gated ...
voltage-gated ion channel activity ...
phosphotransferase activity, ...
enrichment
4
3
2
1
0.001
0.01
0.05
1
p-value (FDR-adjusted)

We further test whether single-cell timescale-transcriptomic associations are captured at the macroscale as follows: for a given gene, we can measure how strongly its expression correlates with membrane time constant parameters at the single-cell level using patch-clamp and RNA sequencing (scRNASeq) data (Tripathy et al., 2017; Bomkamp et al., 2019). Analogously, we can measure its macroscopic transcriptomic-timescale correlation using the cortical gradients above. If the association between the expression of this gene and neuronal timescale is preserved at both levels, then the correlation across cells at the microscale should be similar to the correlation across cortical regions at the macroscale. Comparing across these two scales for all previously-identified timescale-related genes in two studies (N = 170 (Tripathy et al., 2017) and 4168 (Bomkamp et al., 2019) genes), we find a significant correlation between the strength of association at the single-cell and macroscale levels (Figure 3.3D, horizontal black lines; $\rho = 0.36$ and 0.25 for the two datasets, $p < 0.001$ for both). Furthermore, genes with stronger associations to timescale tend to conserve this relationship across single-cell and macroscale levels (Figure 3.3D, separated by macroscale correlation magnitude). Thus, the association between cellular variations in gene expression and cell-intrinsic temporal dynamics is captured at the macroscale, even though scRNAseq and microarray data represent entirely different measurements of gene expression.

While we have shown associations between cortical timescales and genes suspected to influence neuronal dynamics, these data present an opportunity to discover additional novel genes that are functionally related to timescales through a data-driven approach. However, since transcriptomic variation and anatomical hierarchy overlap along a shared macroscopic gradient (Burt et al., 2018; Huntenburg et al., 2018; Margulies et al., 2016), we cannot specify the role certain genes play based on their level of association with timescale alone: gene expression differences across the cortex first result in cell-type and connectivity differences, sculpting the hierarchical organization of cortical anatomy. Consequently, anatomy and cell-intrinsic properties jointly shape neuronal dynamics through connectivity differences (Chaudhuri et al., 2015; Demirtaş et al., 2019) and expression of ion transport and receptor proteins with variable activation timescales, respectively. Therefore, we ask whether variation in gene expression still accounts for variation in timescale beyond the principal structural gradient, and if associated genes have known functional roles in biological processes (schematic in Figure 3.3E). To do this, we first remove the contribution of anatomical hierarchy by linearly regressing out the T1w/T2w gradient from both timescale and individual gene expression gradients. We then fit partial least squares (PLS) models to simultaneously estimate regression weights for all genes (Whitaker et al., 2016), submitting those with significant associations for gene ontology enrichment analysis (GOEA) (Klopfenstein et al., 2018).

We find that genes highly associated with neuronal timescales are preferentially related to transmembrane ion transporter complexes, as well as GABAergic synapses and chloride channels (see Figure 3.3F and Supplementary File 1, Table 3.3 for GOEA results with brain genes only, and Supplementary File 2, Table 3.4 for all genes). When restricted to positively-associated genes only (expression increases with timescales), one functional group related to phosphatidate phosphatase activity is uncovered, including the gene PLPPR1, which has been linked to neuronal plasticity (Savaskan et al., 2004), which is a much slower timescale physiological process. Conversely, genes that are negatively associated with timescale are related to numerous groups involved in the construction and functioning of transmembrane transporters and voltage-gated ion channels, especially potassium and other inorganic cation transporters. To further ensure that these genes specifically relate to neuronal timescale, we perform the same enrichment analysis with T1w/T2w vs. gene maps as a control. The control analysis yields no significant GO terms when restricted to brain-specific genes (in contrast to Figure 3.3F), while repeating the analysis with all genes does yield significant GO terms related to ion channels and synapses, but are much less specific to those (see Supplementary File 3, Table 3.5), including a variety of other gene clusters associated with general metabolic processes, signalling pathways, and cellular components. This further strengthens the point that removing the contribution of T1w/T2w aids in identifying genes that are more specifically associated with neurodynamics, suggesting that inhibition (Telenczuk et al., 2017)—mediated by GABA and chloride channels—and voltage-gated potassium channels have prominent roles in shaping neuronal timescale dynamics at the macroscale level, beyond what's expected based on the anatomical hierarchy alone.

Timescales lengthen in working memory and shorten in aging

Finally, having shown that neuronal timescales are associated with stable anatomical and gene expression gradients across the human cortex, we turn to the final question of the study: are cortical timescales relatively static, or are they functionally dynamic and relevant for human cognition. While previous studies have shown hierarchical segregation of task-relevant information corresponding to intrinsic timescales of different cortical regions (Baldassano et al., 2017; Chien & Honey, 2020; Honey et al., 2012; Runyan et al., 2017; Sarafyazd & Jazayeri, 2019; Wasmuht et al., 2018), as well as optimal adaptation of behavioral timescales to match the environment (Ganupuru et al., 2019; Ossmy et al., 2013), evidence for functionally relevant changes in regional neuronal timescales is lacking. Here, we examine whether timescales undergo short- and long-term shifts during working memory maintenance and aging, respectively.

We first analyze human ECoG recordings from parietal, frontal (PFC & OFC), and medial temporal (MTL) regions of patients (N = 14) performing a visuospatial working memory task that requires a delayed cued response (Figure 3.4A) (Johnson et al., 2018a). Neuronal timescales were extracted for pre-stimulus baseline and memory maintenance delay periods (900 ms, both stimulus-free). Replicating our previous result in Figure 3.5G, we observe that baseline neuronal timescales follow a hierarchical progression across association regions, where parietal cortex, PFC, OFC, and MTL have gradually longer timescales (pairwise Mann-Whitney U test, Figure 3.4B). If neuronal timescales track the temporal persistence of information in a functional manner, then they should expand during delay periods. Consistent with our prediction, timescales in all regions are $\sim$20% longer during delay periods (Figure 3.4C; Wilcoxon rank-sum test). Moreover, only timescale changes in the PFC are significantly correlated with behavior across participants, where longer delay-period timescales relative to baseline are associated with better working memory performance (Figure 3.4D, $\rho = 0.75$, $p = 0.003$). No other spectral features in the recorded brain regions show consistent changes from baseline to delay periods while also significantly correlating with individual performance, including the 1/f-like spectral exponent, narrowband theta (3-8 Hz), and high-frequency (70-100 Hz) activity power (Figure 3.11).

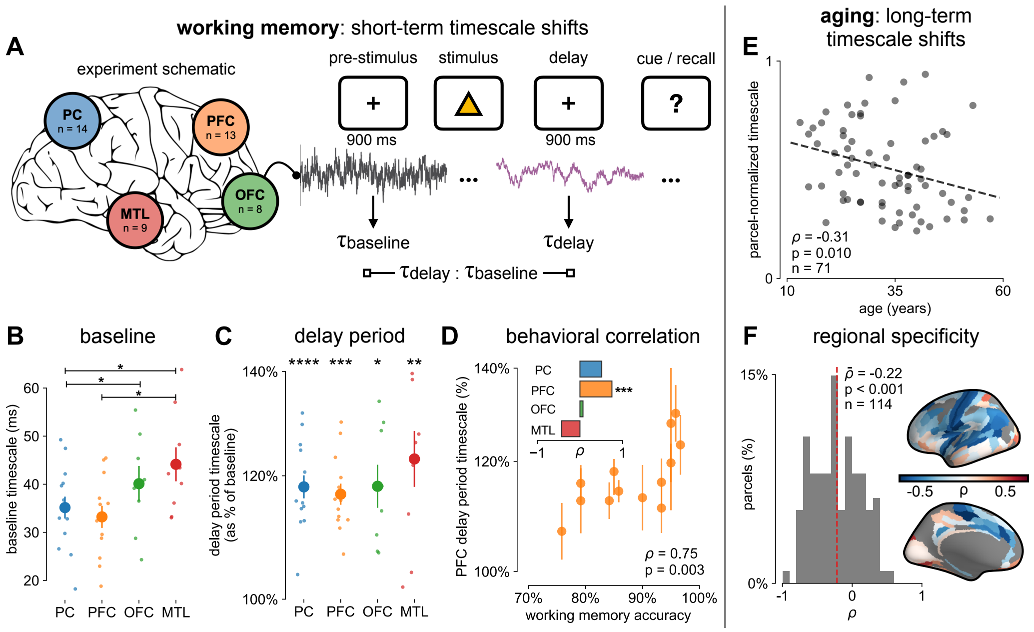

Figure 3.4: Timescales expand during working memory maintenance while tracking performance, and task-free average timescales compress in older adults. (A) 14 participants with overlapping intracranial coverage performed a visuospatial working memory task, with 900 ms of baseline (pre-stimulus) and delay period data analyzed (PC: parietal, PFC: prefrontal, OFC: orbitofrontal, MTL: medial temporal; n denotes number of subjects with electrodes in that region). (B) baseline timescales follow hierarchical organization within association regions (*: $p < 0.05$, Mann-Whitney U test; small dots represent individual participants, large dots and errorbar for mean±s.e.m. across participants). (C) all regions show significant timescale increase during delay period compared to baseline (asterisks represent $p < 0.05, 0.01, 0.005, 0.001$, Wilcoxon signed-rank test). (D) PFC timescale expansion during delay periods predicts average working memory accuracy across participants (dot represents individual participants, mean±s.e.m. across PFC electrodes within participant); inset: correlation between working memory accuracy and timescale change for all regions. (E) in the MNI-iEEG dataset, participant-average cortical timescales decrease (become faster) with age (n = 71 participants with at least 10 valid parcels, see Figure 3.12B). (F) most cortical parcels show a negative relationship between timescales and age, with the exception being parts of the visual cortex and the temporal poles (one-sample t-test, $t = -7.04$, $p < 0.001$; n = 114 parcels where at least 6 participants have data, see Figure 3.12C).

While timescales are consistent with the anatomical and gene expression hierarchy at a snapshot, brain structure itself is not static over time, undergoing many slower, neuroplastic changes during early development and throughout aging in older populations. In particular, aging is associated with a broad range of functional and structural changes, such as working memory impairments (Voytek et al., 2015b; Wang et al., 2011), as well as changes in neuronal dynamics (Voytek et al., 2015b; Voytek & Knight, 2015; Wang et al., 2011) and cortical structure (de Villers-Sidani et al., 2010), such as the loss of slow-deactivating NMDA receptor subunits (Pegasiou et al., 2020). Since neuronal timescales may support working memory maintenance, we predict that timescales would shorten across the lifespan, in agreement with the observed cognitive and structural deteriorations. To this end, we leverage the wide age range in the MNI-iEEG dataset (13-62 years old) and probe average cortical timescales for each participant as a function of age. Since ECoG coverage is sparse and non-uniform across participants, simply averaging across parcels within individual participants confounds the effect of aging with the spatial effect of cortical hierarchy. Instead, we first normalize each parcel by its max value across all participants before averaging within participants, excluding those with fewer than 10 valid parcels (N = 71 of 106 subjects remaining; results hold for a large range of threshold values, Figure 3.12B). We observe that older adults have faster neuronal timescales ($\rho = -0.31$, $p = 0.010$; Figure 3.4E), and that timescales shorten with age in most areas across the cortex (Figure 3.4F, $t = -7.04$, $p < 0.001$; 114 out of 189 parcels where at least 6 participants have data, see Figure 3.12C). This timescale compression is especially prominent in sensorimotor, temporal, and medial frontal regions. These results support our hypothesis that neuronal timescales, estimated from transmembrane current fluctuations, can rapidly shift in a functionally relevant manner, as well as slowly—over decades—in healthy aging.

3.3 Discussion

Theoretical accounts and converging empirical evidence predict a graded variation of neuronal timescales across the human cortex (Chaudhuri et al., 2015; Huntenburg et al., 2018; Wang, 2020), which reflects functional specialization and implements hierarchical temporal processing crucial for complex cognition (Kiebel et al., 2008). This timescale gradient is thought to emerge as a consequence of cortical variations in cytoarchitecture, as well as both macroscale and microcircuit connectivity, thus serving as a bridge from brain structure to cognitive function (Kanai and Rees 2011). In this work, we infer the timescale of non-rhythmic transmembrane current fluctuations from invasive human intracranial recordings and test those predictions explicitly. We discuss the implications and limitations of our findings below.

Multiple quantities for neuronal timescale and anatomical hierarchy

We first find that neuronal timescales vary continuously across the human cortex and coincide with the anatomical hierarchy, with timescales increasing from primary sensory and motor to association regions. While we use the continuous T1w/T2w gradient as a surrogate measure for anatomical hierarchy, there are multiple related but distinct perspectives on what "cortical hierarchy" means, including, for example, laminar connectivity patterns from tract tracing data (Felleman & Van Essen, 1991; Vezoli et al., 2020), continuous (and latent-space) gradients of gene expression and microarchitectural features (Huntenburg et al., 2018), and network connectivity scales (see review of (Hilgetag & Goulas, 2020))—with most of these following a graded sensorimotor-to-association area progression. Similarly, it is important to note that there exist many different quantities that can be considered as characteristic neuronal timescales across several spatial scales, including membrane potential and synaptic current timescales (Duarte et al., 2017), single-unit spike-train timescales (Murray et al., 2014), population code timescales (Runyan et al., 2017), and even large-scale circuit timescales measured from the fMRI BOLD signal (Watanabe et al., 2019). We show here that timescales inferred from ECoG are consistently approximately ten times faster than single-unit spiking timescales in macaques, corroborating the fact that field potential signals mainly reflect fast transmembrane and synaptic currents (Buzsáki et al., 2012), whose timescales are related to, but distinct from, single-unit timescales measured in previous studies (Dotson et al., 2018; Ogawa & Komatsu, 2010; Wasmuht et al., 2018).

Because field potential fluctuations are driven by currents from both locally generated and distal inputs, our results raise questions on how and when these timescales interact to shape downstream spiking dynamics. Furthermore, while we specifically investigate here the aperiodic timescale, which corresponds to the exponential decay timescale measured in previous studies, recent work has shown a similar gradient of oscillatory timescales (i.e., frequency) along the anterior-posterior axis of the human cortex (Mahjoory et al., 2020). Based on the similarity of these gradients and known mechanisms of asynchronous and oscillatory population dynamics (e.g., balance of excitation and inhibition in generating gamma oscillations and the asynchronous irregular state in cortical circuits (Brunel, 2000; Brunel & Wang, 2003)), we speculate that timescales of oscillatory and aperiodic neural dynamics may share (at least partially) circuit mechanisms at different spatial scales, analogous to the relationship between characteristic frequency and decay constant in a damped harmonic oscillator model.

Collinearity and surrogate nature of post-mortem gene expression gradients

Using post-mortem gene expression data as a surrogate for protein density, transcriptomic analysis uncovers the potential roles that transmembrane ion transporters and synaptic receptors play in establishing the cortical gradient of neuronal timescales. The expression of voltage-gated potassium channel, chloride channel, and GABAergic receptor genes, in particular, are strongly associated with the spatial variation of neuronal timescale. Remarkably, we find that electrophysiology/transcriptomic relationships discovered at the single-cell level, through patch-clamp recordings and single-cell RNA sequencing, are recapitulated at the macroscale between bulk gene expression and timescales inferred from ECoG. That being said, it is impossible to make definitive causal claims with the data presented in this study, especially considering the fact that several microanatomical features, such as grey matter myelination and cortical thickness, follow similar gradients across the cortex (Burt et al., 2018). To discover genes specifically associated with timescale while accounting for the contribution of the overlapping anatomical hierarchy, we linearly regress out the T1w/T2w gradient from both timescale and gene expression gradients. Although this procedure does not account for any nonlinear contributions from anatomy, gene enrichment control analysis using T1w/T2w instead of timescales further demonstrates that the discovered genes—transmembrane ion transporters and inhibitory synaptic receptors—are more specifically associated with the timescale gradient, over and above the level predicted by anatomical hierarchy alone. From these results, we infer that potassium and chloride ion channels, as well as GABAergic receptors, may play a mechanistic role in altering the timescale of transmembrane currents at the macroscopic level.

However, this interpretation rests on the key assumption that mRNA expression level is a faithful representation of the amount of functional proteins in a given brain region. In general, gene expression levels are highly correlated with the percentage of cells expressing that gene within brain regions (Lein et al., 2007). Therefore, on a population level, the regional density of a particular ion channel or receptor protein is high if bulk mRNA expression is high. Furthermore, recent works have shown that neurotransmitter receptor density measured via autoradiography in post-mortem brains follows similar cortical gradients (Goulas et al., 2020), and that gene expression levels of neurotransmitter receptors (e.g., 5HT) are strongly correlated with ligand binding potential measured via PET (Gryglewski et al., 2018). Thus, as a first order approximation, receptor gene expression is an adequate surrogate for receptor protein density in the brain at the macroscale, though the relationship between mRNA expression and their transport and translation into channel proteins, the process of incorporating those proteins into membranes and synapses, and how these gene expression maps can be related to other overlapping macroscopic gradients are complex issues (see e.g., (Fornito et al., 2019; Liu et al., 2016)). Thus, our analyses represent an initial data-mining process at the macroscopic level, which should motivate further studies in investigating the precise roles voltage-gated ion channels and synaptic inhibition play in shaping functional neuronal timescales through causal manipulations, complementary to existing lines of research focusing on NMDA activation and recurrent circuit motifs.

Structural constraints vs. behaviorally-required flexibility in timescale

Finally, we show that neuronal timescales are not static, but can change both in the short- and long-term. Transmembrane current timescales across multiple association regions, including parietal, frontal, and medial temporal cortices, increase during the delay period of a working memory task, consistent with the emergence of persistent spiking during working memory delay. Working memory performance across individuals, however, is predicted by the extent of timescale increase in the PFC only. This further suggests that behaviorally relevant neural activity may be localized despite widespread task-related modulation (Pinto et al., 2019), even at the level of neuronal membrane fluctuations. In the long-term, we find that neuronal timescale shortens with age in most cortical regions, linking age-related synaptic, cellular, and connectivity changes—particularly those that influence neuronal integration timescale—to the compensatory posterior-to-anterior shift of functional specialization in healthy aging (Davis et al., 2008).

These results raise further questions regarding contrasting, and potentially complementary, aspects of neuronal timescale: on the one hand, task-free timescales across the cortex are shaped by relatively static macro- and microarchitectural properties (Figures 2 and 3); on the other hand, timescales are dynamic and shift with behavioral demand (Figure 3.4). While long-term structural changes in the brain can explain shifts in neuronal timescales throughout the aging process, properties such as ion channel protein density probably do not change within seconds during a working memory task. We speculate that structural properties may constrain dynamical properties (such as timescale) to a possible range within a particular brain region and at different spatial scales, while task requirements, input statistics, short-term synaptic plasticity, and neuromodulation can then shift timescale within this range. We posit, then, that only shifts in dynamics within the area of relevance (i.e., PFC for working memory) are indicative of task performance, consistent with recent ideas of computation-through-dynamics (Vyas et al., 2020). Nevertheless, which neuromodulatory and circuit mechanisms are involved in shifting local timescales, and how timescales at different spatial scales (e.g., synaptic, neuronal, population) interact to influence each other (Breakspear, 2017; Duarte et al., 2017; Freeman, 2000; Freeman & Erwin, 2008; Gjorgjieva et al., 2016; Shine et al., 2019) remain open questions for future investigation.

Conclusion

In summary, we identify consistent and converging patterns between transcriptomics, anatomy, dynamics, and function across multiple datasets of different modalities from different individuals and multiple species. As a result, evidence for these relationships can be supplemented by more targeted approaches such as imaging of receptor metabolism. Furthermore, the introduction and validation of an open-source toolbox (Donoghue et al., 2020) for inferring timescales from macroscale electrophysiological recordings potentially allows for the non-invasive estimation of neuronal timescales, using widely accessible tools such as EEG and MEG. These results open up many avenues of research for discovering potential relationships between microscale gene expression and anatomy with the dynamics of neuronal population activity at the macroscale in humans.

3.4 Materials & Methods

Summary of data and code All IPython notebooks: https://github.com/rdgao/field-echos/tree/master/notebooks. Projection of T1w/T2w and gene expression maps from MNI volumetric coordinates to HCP-MMP1.0 can be found: https://github.com/rudyvdbrink/Surface_projection.

Table 3.1: Summary of open-access datasets used.

Data	**Ref.**	**Specific Source/ Format Used**	**Participant info**	**Relevant Figures**
MNI Open iEEG Atlas	(Frauscher et al., 2018b,a)		N = 105 (48 female); Ages: 13-65, 33.4±10.6	Fig. 2A-D, Fig. 3, Fig. 4E-F
Tw1/T2w & cortical thickness maps from Human Connectome Project	(Glasser & Van Essen, 2011; Glasser et al., 2016)	Release S1200, March 1, 2017	N = 1096 (596 female); Ages: 22-36+ (details restricted due to identifiability)	Fig. 2C-D, Fig. 3D-F
Neurotycho macaque ECoG	(Nagasaka et al., 2011; Yanagawa et al., 2013)	Eyes-open state from anesthesia datasets (propofol and ketamine)	2 animals (Chibi and Geroge), 4 sessions each	Fig. 2E-G
Macaque single-unit timescales	(Murray et al., 2014)	Fig. 1 of reference		Fig. 2E-G
Whole-cortex interpolated Allen Brain Atlas human gene expression	(Hawrylycz et al., 2012; Gryglewski et al., 2018)		N = 6 (1 female); Age: 24,31,39,49,55,57 (42.5±12.2)	Fig. 3
Single-cell timescale-related genes	(Tripathy et al., 2017; Bomkamp et al., 2019)	Table S3 from (Tripathy et al., 2017), Online Table 1 from (Bomkamp et al., 2019)	N = 170 (Tripathy et al., 2017) and 4168 (Bomkamp et al., 2019) genes	Fig. 3C-D
Human working memory ECoG	(Johnson et al., 2018b,a; Johnson, 2019, 2018)	CRCNS fcx-2 and fcx-3	N = 14 (5 female); Age: 22-50, 30.9±7.8	Fig. 4A-D

Inferring timescale from autocorrelation and power spectral density. Consistent with

Table 3.2: Reproducing figures from code repository.

Notebook	**Results**
1_sim_method_schematic.ipynb	**simulations**: Fig. 1B-E
2_viz_NeuroTycho-SU.ipynb	**macaque timescales**: Fig. 2E-G, Figure 2—figure supplement 4
3_viz_human_structural.ipynb	**human timescales vs. T1w/T2w and gene expression**: Fig. 2A-D, Figure 2—figure supplement 1,3, Fig. 3, Figure 3—figure supplement 1-2, Supplementary File 1-3
4b_viz_human_wm.ipynb	**human working memory: Fig. 4A-D**, Figure 4—figure supplement 1
4a_viz_human_aging.ipynb	**human aging**: Fig. 4E-F, Figure 4—figure supplement 2
supp_spatialautocorr.ipynb	**spatial autocorrelation-preserving nulls**: Figure 2—figure supplement 2

previous studies, we define "neuronal timescale" as the exponential decay time constant (τ) of the empirical autocorrelation function (ACF), or lagged correlation (Honey et al., 2012; Murray et al., 2014). τ can be naively estimated to be the time it takes for the ACF to decrease by a factor of e when there are no additional long-term, scale-free, or oscillatory processes, or by fitting a function of the form $f(t) = e^{\frac{-t}{\tau}}$ and extracting the parameter τ. Equivalently, the power spectral density (PSD) is the Fourier Transform of the ACF via Wiener-Khinchin theorem (Khintchine, 1934), and follows a Lorentzian function of the form $L(f) = \frac{A}{k+f^{\chi}}$ for approximately exponential-decay processes, with χ=2 exactly when the ACF is solely composed of an exponential decay term, though it is often variable and in the range between 2-6 for neural time series (Donoghue et al., 2020; Miller et al., 2009; Podvalny et al., 2015; Voytek et al., 2015b). Timescale can be computed from the parameter k as $\tau = \frac{1}{2\pi f_k}$, where $f_k \approx k^{\frac{1}{\chi}}$ is approximated to be the "knee frequency", at which a bend or knee in the power spectrum occurs, and equality holds when χ=2.

Computing power spectral density (PSD). PSDs are estimated using a modified Welch's method, where short-time windowed Fourier transforms (STFT) are computed from the time series, but the median is taken across time instead of the mean (in conventional Welch's method) to minimize the effect of high-amplitude transients and artifacts (Izhikevich et al., 2018). Custom functions for this can be found in NeuroDSP (Cole et al., 2019), a published and open-source digital signal processing toolbox for neural time series (neurodsp.spectral.compute_spectrum). For simulated data, Neurotycho macaque ECoG, and MNI-iEEG datasets, we use 1-second long Hamming windows with 0.5-s overlap. To estimate single-trial PSDs for the working memory ECoG dataset (CRCNS Johnson-ECoG (Johnson, 2019, 2018)), we simply apply Hamming window to 900-ms long epoched time series and compute the squared magnitude of the windowed-Fourier transform.

Spectral parametrization - Fitting Oscillations and 1/f (FOOOF). We apply spectral parameterization (Donoghue et al., 2020) to extract timescales from PSDs. Briefly, we decompose log-power spectra into a summation of narrowband periodic components—modeled as Gaussians—and an aperiodic component—modeled as a generalized Lorentzian function centered at 0 Hz ($L(f)$ above). For inferring decay timescale, this formalism can be practically advantageous when a strong oscillatory or variable power-law (χ) component is present, as is often the case for neural signals. While oscillatory and power-law components can corrupt naive measurements of τ as time for the ACF to reach $\frac{1}{e}$, they can be easily accounted for and ignored in the frequency domain as narrowband peaks and 1/f-exponent fit. We discard the periodic components and infer timescale from the aperiodic component of the PSD. For a complete mathematical description of the model, see (Donoghue et al., 2020).

Simulation and validation. We simulate the aperiodic background component of neural field potential recordings as autocorrelated stochastic processes by convolving Poisson population spikes with exponentially-decaying synaptic kernels with predefined decay time constants (neurodsp.sim.sim_synaptic_current). PSDs of the simulated data are computed and parameterized as described above, and we compare the fitted timescales with their ground-truth values.

Macaque ECoG and single unit timescales data. Macaque single-unit timescales are taken directly from values reported in Figure 1c of (Murray et al., 2014). Whole-brain surface ECoG data (1000Hz sampling rate) is taken from the Neurotycho repository (Nagasaka et al., 2011; Yanagawa et al., 2013), with 8 sessions of 128-channel recordings from two animals

(George and Chibi, 4 sessions each). Results reported in Figure. 2E-G are from 10 minutes eyes-open resting periods to match the pre-stimulus baseline condition of single-unit experiments. Timescales for individual ECoG channels are extracted and averaged over regions corresponding to single-unit recording areas from (Murray et al., 2014) (Figure 3.2F inset and Figure 3.8), which are selected visually based on the overlapping cortical map and landmark sulci/gyri. Each region included between 2-4 electrodes (see Figure 3.8B for selected ECoG channel indices for each region).

Statistical analysis for macaque ECoG and spiking timescale. For each individual recording session, as well as the grand average, Spearman rank correlation was computed between spiking and ECoG timescales. Linear regression models were fit using the python package scipy (Virtanen et al., 2020) (scipy.stats.linregress) and the linear slope was used to compute the scaling coefficient between spiking and ECoG timescales.

Variations in neuronal timescale, T1/T2 ratio, and mRNA expression across human cortex. The following sections describe procedures for generating the average cortical gradient maps for neuronal timescale, MR-derived T1w/T2w ratio, and gene expression from the respective raw datasets. All maps were projected onto the 180 left hemisphere parcels of Human Connectome Project's Multimodal Parcellation (Glasser et al., 2016) (HCP-MMP1.0) for comparison, described in the individual sections. All spatial correlations are computed as Spearman rank correlations between maps. Procedure for computing statistical significance while accounting for spatial autocorrelation is described in detail below under the sections spatial statistics and spatial autocorrelation modeling.

Neuronal timescale map. The MNI Open iEEG dataset consists of 1 minute of resting state data across 1772 channels from 106 epilepsy patients (13-62 years old, 58 males and 48 females), recorded using either surface strip/grid or stereoEEG electrodes, and cleaned of visible artifacts (Frauscher et al., 2018a,b). Neuronal timescales were extracted from PSDs of individual channels, and projected from MNI voxel coordinates onto HCP-MMP1.0 surface parcellation as follows:

For each patient, timescale estimated from each electrode was extrapolated to the rest of the cortex in MNI coordinates using a Gaussian weighting function (confidence mask), $w(r) = e^{-\frac{r^2}{\alpha^2}}$, where r is the Euclidean distance between the electrode and a voxel, and α is the distance scaling constant, chosen here such that a voxel 4mm away has 50% weight (or, confidence). Timescale at each voxel is computed as a weighted spatial average of timescales from all electrodes (i) of that patient, i.e., $\tau_{voxel} = \frac{\sum_i w(r_i)\tau_i}{\sum_i w(r_i)}$. Similarly, each voxel is assigned a confidence rating that is the maximum of weights over all electrodes (w_{voxel} (r_{min}), of the closest electrode), i.e., a voxel right under an electrode has a confidence of 1, while a voxel 4mm away from the closest electrode has a confidence of 0.5, etc.

Timescales for each HCP-MMP parcel were then computed as the confidence-weighted arithmetic mean across all voxels that fall within the boundaries of that parcel. HCP-MMP boundary map is loaded and used for projection using NiBabel (Brett et al., 2020). This results in a 180 parcels-by-106 patients timescale matrix. A per-parcel confidence matrix of the same dimensions was computed by taking the maximum confidence over all voxels for each parcel (Figure 3.5A). The average cortical timescale map (gradient) is computed by taking the confidence-weighted average at each parcel across all participants. Note that this procedure for locally thresholded and weighted average is different from projection procedures used for the mRNA and T1w/T2w data due to region-constrained and heterogeneous ECoG electrode sites across participants. While coverage is sparse and idiosyncratic in individual participants, it does not vary as a function of age, and when pooling across the entire population, 178 of 180 parcels have at least one patient with an electrode within 4mm, with the best coverage in sensorimotor, temporal, and frontal regions (Figure 3.5).

T1w/T2w ratio and cortical thickness maps. As a measure of structural cortical hierarchy, we used the ratio between T1- and T2-weighted structural MRI, referred to as T1w/T2w map in main text, or the myelin map (Burt et al., 2018; Glasser & Van Essen, 2011). Since there is little variation in the myelin map across individuals, we used the group average myelin map of the WU-Minn HCP S1200 release (N = 1096, March 1, 2017 release) provided in HCP-MMP1.0 surface space. For correlation with other variables, we computed the median value per parcel, identical to the procedure for mRNA expression below. Cortical thickness map was similarly generated.

mRNA expression maps. We used the Allen Human Brain Atlas (AHBA) gene expression dataset (Hawrylycz et al., 2012, 2015) that comprised postmortem samples of 6 donors (1 female, 5 male) that underwent microarray transcriptional profiling. Spatial maps of mRNA expression were available in volumetric 2 mm isotropic MNI space, following improved nonlinear registration and whole-brain prediction using variogram modeling as implemented by (Gryglewski et al., 2018). We used whole-brain maps available from (Gryglewski et al., 2018) rather than the native sample-wise values in the AHBA database to prevent bias that could occur due to spatial inhomogeneity of the sampled locations. In total, 18114 genes were included for analyses that related to the dominant axis of expression across the genome.

We projected the volumetric mRNA expression data onto the HCP-MMP cortical surface using the HCP workbench software (v1.3.1 running on Windows OS 10) with the "enclosing" method, and custom MATLAB code (github.com/rudyvdbrink/surface_projection). The enclosing method extracts for all vertices on the surface the value from enclosing voxels in the volumetric data. Alternative projection methods such as trilinear 3D linear interpolation of surrounding voxels, or ribbon mapping that constructs a polyhedron from each vertex's neighbors on the surface to compute a weighted mean for the respective vertices, yielded comparable values, but less complete cortical coverage. Moreover, the enclosing method ensured that no transformation of the data (non-linear or otherwise) occurred during the projection process and thus the original values in the volumetric data were preserved.

Next, for each parcel of the left hemisphere in HCP-MMP, we extracted the median vertex-wise value. We used the median rather than the mean because it reduced the contribution of outliers in expression values within parcels. Vertices that were not enclosed by voxels that contained data in volumetric space were not included in the parcel-wise median. This was the case for 539 vertices (1.81% of total vertices). Linear interpolation across empty vertices prior to computing median parcel-wise values yielded near-identical results (r = 0.95 for reconstructed surfaces). Lastly, expression values were mean and variance normalized across parcels to facilitate visualization. Normalization had no effect on spatial correlation between gene expression and other variables since the spatial distribution of gene expression was left unaltered.

Selection of brain-specific genes. Similar to (Burt et al., 2018; Fagerberg et al., 2014; Genovese et al., 2016), N = 2429 brain-specific genes were selected based on the criteria that expression in brain tissues were 4 times higher than the median expression across all tissue types, using Supplementary Dataset 1 of (Fagerberg et al., 2014). PC1 result shown in Figure 3.3A is computed from brain-specific genes, though findings are identical when using all genes ($\rho = -0.56$ with timescale map, Figure 3.9).

Spatial statistics. All correlations between spatial maps (timescale, T1w/T2w, gene principal component, and individual gene expressions) were computed using Spearman rank correlation. As noted in (Burt et al., 2018, 2020; Vos de Wael et al., 2020), neural variables vary smoothly and continuously across the cortical surface, violating the assumption of independent samples. As a result, when correlating two variables, each with non-trivial spatial autocorrelation, the naive p-value is artificially lowered since it is compared against an inappropriate null hypothesis, i.e., randomly distributed or shuffled values across space. Instead, a more appropriate null hypothesis introduces spatial autocorrelation-preserving null maps, which destroys any potential correlation between two maps while respecting their spatial autocorrelations. For all spatial correlation analyses, we generated N = 1000 null maps of one variable (timescale map unless otherwise noted), and the test statistic, Spearman correlation (ρ), is computed against the other variable of interest to build the null distribution. Two-tailed significance is then computed as the proportion of the null distribution that is less extreme than the empirical correlation value. All regression lines were computed by fitting a linear regression to log-timescale and the structural feature maps.

Spatial autocorrelation modeling. To generate spatial autocorrelation-preserving null maps, we used Moran's Spectral Randomization (MSR) (Wagner & Dray, 2015) from the python package BrainSpace (Vos de Wael et al., 2020). Details of the algorithm can be found in the above references. Briefly, MSR performs eigendecomposition on a spatial weight matrix of choice, which is taken here to be the inverse average geodesic distance matrix between all pairs of parcels in HCP-MMP1.0. The eigenvectors of the weight matrix are then used to generate randomized null feature maps that preserves the autocorrelation of the empirical map. We used the singleton procedure for null map generation. All significance values reported (Figure 3.2D, Figure 3.3A-C) were adjusted using the above procedure.

We also compare two other methods of generating null maps: spatial variogram fitting (Burt et al., 2020) and spin permutation (Alexander-Bloch et al., 2018). Null maps were generated for timescale using spatial variogram fitting, while for spin permutation they were generated for vertex-wise T1w/T2w and gene PC1 maps before parcellation, so as to preserve surface locations of the parcellation itself. All methods perform similarly, producing comparable spatial autocorrelation in the null maps, assessed using spatial variogram, as well as null distribution of spatial correlation coefficients between timescale and T1w/T2w (Figure 3.6).

Principal Component Analysis (PCA) of gene expression. We used scikit-learn (Pedregosa, 2011) PCA (sklearn.decomposition.PCA) to identify the dominant axes of gene expression variation across the entire AHBA dataset, as well as for brain-specific genes. PCA was computed on the variance-normalized average gene expression maps, X, an N x P matrix where N = 18114 (or N = 2429 brain-specific) genes, and P = 180 cortical parcels. Briefly, PCA factorizes X such that $X = USV^T$, where U and V are unitary matrices of dimensionality N x N and P x P, respectively. S is the same dimensionality as X and contains non-negative descending eigenvalues on its main diagonal (Λ). Columns of V are defined as the principal components (PCs), and the dominant axis of gene expression is then defined as the first column of V, whose proportion of variance explained in the data is the first element of Λ divided by the sum over Λ. Results for PC1 and PC2-10 are shown in Figure 3.3A and Figure 3.9, respectively.

Comparison of timescale-transcriptomic association with single-cell timescale genes. Single-cell timescale genes were selected based on data from Table S3 and Online Table 1 of (Tripathy et al., 2017; Bomkamp et al., 2019), respectively. Using single-cell RNA sequencing data and patch-clamp recordings from transgenic mice cortical neurons, these studies identified genes whose expression significantly correlated with electrophysiological features derived from generalized linear integrate and fire (GLIF) model fits. We selected genes that were significantly correlated to membrane time constant (tau), input resistance (Rin or ri), or capacitance (Cm or cap) in the referenced data tables, and extracted the level of association between gene expression and those electrophysiological feature (correlation 'DiscCorr' in (Tripathy et al., 2017) and linear coefficient "beta_gene" in (Bomkamp et al., 2019)).

To compare timescale-gene expression association at the single-cell and macroscale level, we correlated the single-cell associations extracted above with the spatial correlation coefficient (macroscale ρ) between ECoG timescale and AHBA microarray expression data for those same genes, restricting to genes with $p < 0.05$ for macroscale correlation (results identical for non-restrictive gene set). Overall association for all genes, as well as split by quintiles of their absolute macroscale correlation coefficient, are shown in Figure 3.3D. Example "single-cell timescale" genes shown in Figure 3.3B-C are genes showing the highest correlations with those electrophysiology features reported in Table 2 of (Bomkamp et al., 2019).

T1w/T2w-removed timescale and gene expression residual maps. To remove anatomical hierarchy as a potential mediating variable in timescale-gene expression relationships, we linearly regress out the T1w/T2w map from the (log) timescale map and individual gene expression maps. T1w/T2w was linearly fit to log-timescale, and the error between T1w/T2w-predicted timescale and empirical timescale was extracted (residual); this identical procedure was applied to every gene expression map to retrieve the gene residuals. Spatial autocorrelation-preserving null timescale residual maps were similarly created using MSR.

Partial least squares regression model. Due to multicollinearity in the high-dimensional gene expression dataset (many more genes than parcels), we fit a partial least squares model to the timescale map with one output dimension (sklearn.cross_decomposition.PLSRegression) to estimate regression coefficient for all genes simultaneously, resulting in N = 18114 (or N = 2429 brain-specific) PLS weights (Vértes et al., 2016; Whitaker et al., 2016). To determine significantly associated (or, "enriched") genes, we repeated the above PLS-fitting procedure 1000 times but replaced the empirical timescale map (or residual map) with null timescale maps (or residual maps) that preserved its spatial autocorrelation. Genes whose absolute empirical PLS weight that was greater than 95% of its null weight distribution was deemed to be enriched, and submitted for gene ontology enrichment analysis.

Gene ontology enrichment analysis (GOEA). The Gene Ontology (GO) captures hierarchically structured relationships between GO items representing aspects of biological processes (BP), cellular components (CC), or molecular functions (MF). For example, "synaptic signaling", "chemical synaptic transmission", and "glutamatergic synaptic transmission" are GO items with increasing specificity, with smaller subsets of genes associated with each function. Each GO item is annotated with a list of genes that have been linked to that particular process or function. GOEA examines the list of enriched genes from above to identify GO items that are more associated with those genes than expected by chance. We used GOATOOLS (Klopfenstein et al., 2018) to perform GOEA programmatically in python.

The list of unranked genes with significant empirical PLS weights was submitted for GOEA as the "study set", while either the full ABHA list or brain-specific gene list was used as the "reference set". The output of GOEA is a list of GO terms with annotated genes that are enriched or purified (i.e., preferentially appearing or missing in the study list, respectively) more often than by chance, determined by Fisher's exact test.

Enrichment ratio is defined as follows: given a reference set with N total genes, and n were found to be significantly associated with timescale (in the study set), for a single GO item with B total genes annotated to it, where b of them overlap with the study set, then enrichment = (b/n)/(B/N). Statistical significance is adjusted for multiple comparisons following Benjamini-Hochberg procedure (false discovery rate q-value reported in Figure 3.3F), and all significant GO items ($q < 0.05$) are reported in Figure 3.3F, in addition to some example items that did not pass significance threshold. For a detailed exposition, see (Bauer, 2017). Figure 3.3F shows results using brain-specific genes. The GO items that are significantly associated are similar when using the full gene set, but typically with larger q-values (Supplementary File 1 and 2, Table 3.3 and 3.4) due to a much larger set of (non-brain-specific) genes. Control analysis was conducted using T1w/T2w, with 1000 similarly generated null maps, instead of timescale.

Working memory ECoG data and analysis. The CRCNS fcx-2 and fcx-3 datasets include 17 intracranial ECoG recordings in total from epilepsy patients (10 and 7, respectively) performing the same visuospatial working memory task (Johnson et al., 2018a,b; Johnson, 2019, 2018). Subject 3 (s3) from fcx-2 was discarded due to poor data quality upon examination of trial-averaged PSDs (high noise floor near 20 Hz), while s5 and s7 from fcx-3 correspond to s5 and s8 in fcx-2 and were thus combined. Together, data from 14 unique participants (22-50 years old, 5 female) were analyzed, with variable and overlapping coverage in parietal cortex (PC, n=14), prefrontal cortex (PFC, n=13), orbitofrontal cortex (OFC, n=8), and medial temporal lobe (MTL, n=9). Each channel was annotated as belonging to one of the above macro regions.

Experimental setup is described in (Johnson et al., 2018a,b; Johnson, 2019, 2018) in detail. Briefly, following a 1-second pre-trial fixation period (baseline), subjects were instructed to focus on one of two stimulus contexts (“identity” or “relation” information). Then two shapes were presented in sequence for 200 ms each. After a 900 or 1150 ms jittered precue delay (delay1), the test cue appeared for 800 ms, followed by another post-cue delay period of the same length (delay2). Finally, the response period required participants to perform a 2-alternative forced choice test based on the test cue, which varied based on trial condition. For our analysis, we collapsed across the stimulus context conditions and compared neuronal timescales during the last 900 ms of baseline and delay periods from the epoched data, which were free of visual stimuli, in order to avoid stimulus-related event-related potential effects. Behavioral accuracy for each experimental condition was reported for each participant, and we average across both stimulus context conditions to produce a single working memory accuracy per participant.

Single-trial power spectra were computed for each channel as the squared magnitude of the Hamming-windowed Fourier Transform. We used 900 ms of data in all 3 periods (pre-trial, delay1, and delay2). Timescales were estimated by applying spectral parameterization as above, and the two delay-period estimates were averaged to produce a single delay period value. For comparison, we computed single-trial theta (3-8 Hz) and high-frequency activity (high gamma (Mukamel et al., 2005), 70-100 Hz) powers as the mean log-power within those frequency bins, as well as spectral exponent (χ). Single-trial timescale difference between delay and baseline was calculated as the difference of the log timescales due to the non-normal distribution of single-trial timescale estimates. All other neural features were computed by subtracting baseline from the delay period.

All neural features were then averaged across channels within the same regions, then trials, for each participant, to produce per-participant region-wise estimates, and finally averaged across all participants for the regional average in Figure 3.4B-C. Two-sided Mann-Whitney U tests were used to test for significant differences in baseline timescale between pairs of regions (Figure 3.4B). Two-sided Wilcoxon rank-sum tests were used to determine the statistical significance of timescale change in each region (Figure 3.4C), where the null hypothesis was no change between baseline and delay periods (i.e., delay is 100% of baseline). Spearman rank correlation was used to determine the relationship between neural activity (timescale; theta; high-frequency; χ) change and working memory accuracy across participants (Figure 3.4D, Figure 3.11).

Per-subject average cortical timescale across age. Since electrode coverage in the MNI-iEEG dataset is sparse and non-uniform across participants (Figure 3.5), simply averaging across parcels within individuals to estimate an average cortical timescale per participant confounds the effect of age with the spatial effect of cortical hierarchy. Therefore, we instead first normalize each parcel by its max value across all participants before averaging within participants, excluding those with fewer than 10 valid parcels (71 of 106 subjects remaining; results hold for a range of threshold values; Figure 3.12B). Spearman rank correlation was used to compute the association between age and average cortical timescale.

Age-timescale association for individual parcels. Each cortical parcel had a variable number of participants with valid timescale estimates above the consistency threshold, so we compute Spearman correlation between age and timescale for each parcel, but including only those with at least 5 participants (114 of 180 parcels, result holds for a range of threshold values; Figure 3.12C). Spatial effect of age-timescale variation is plotted in Figure 3.4F, where parcels that did not meet the threshold criteria are greyed out. Mean age-timescale correlation from individual parcels was significantly negative under one-sample t-test.

Acknowledgements

Chapter 3, in full, is a reprint of the material as it appears in the following manuscript published in *eLife*: Gao, R., van den Brink, R. L., Pfeffer, T., & Voytek, B. (2020). **Neuronal timescales are functionally dynamic and shaped by cortical microarchitecture.** The dissertation author was the primary investigator and author of this paper.

3.5 Figure Supplements

Figure 3.5: Figure 3.2—figure supplement 1. MNI-iEEG dataset electrode coverage. (A) per-parcel Gaussian-weighted mask values showing how close the nearest electrode was to a given HCP-MMP1.0 parcel for each participant. Brighter means closer, 0.5 corresponds to the nearest electrode being 4 mm away. (B) maximum mask weight for each parcel across all participants. Most parcels have electrodes very close by in at least one participant across the entire participant pool. (C) the number of valid HCP-MMP parcels each participant has above the confidence threshold of 0.5 is uncorrelated with age. (D) cortical map of the number of participants with confidence above threshold at each parcel. Sensorimotor, frontal, and lateral temporal regions have the highest coverage. (E) cortical map of the average age of participants with confidence above threshold at each parcel. (F) age distribution of participants with confidence above threshold at each parcel. Average age per parcel (red line) is relatively stable while age distribution varies from parcel to parcel (each subject is a black dot). (G) Average neuronal timescale when further aggregating the 180 Glasser parcels into 21 macro-regions (mean$\pm$s.e.m across parcels within the macro-region).

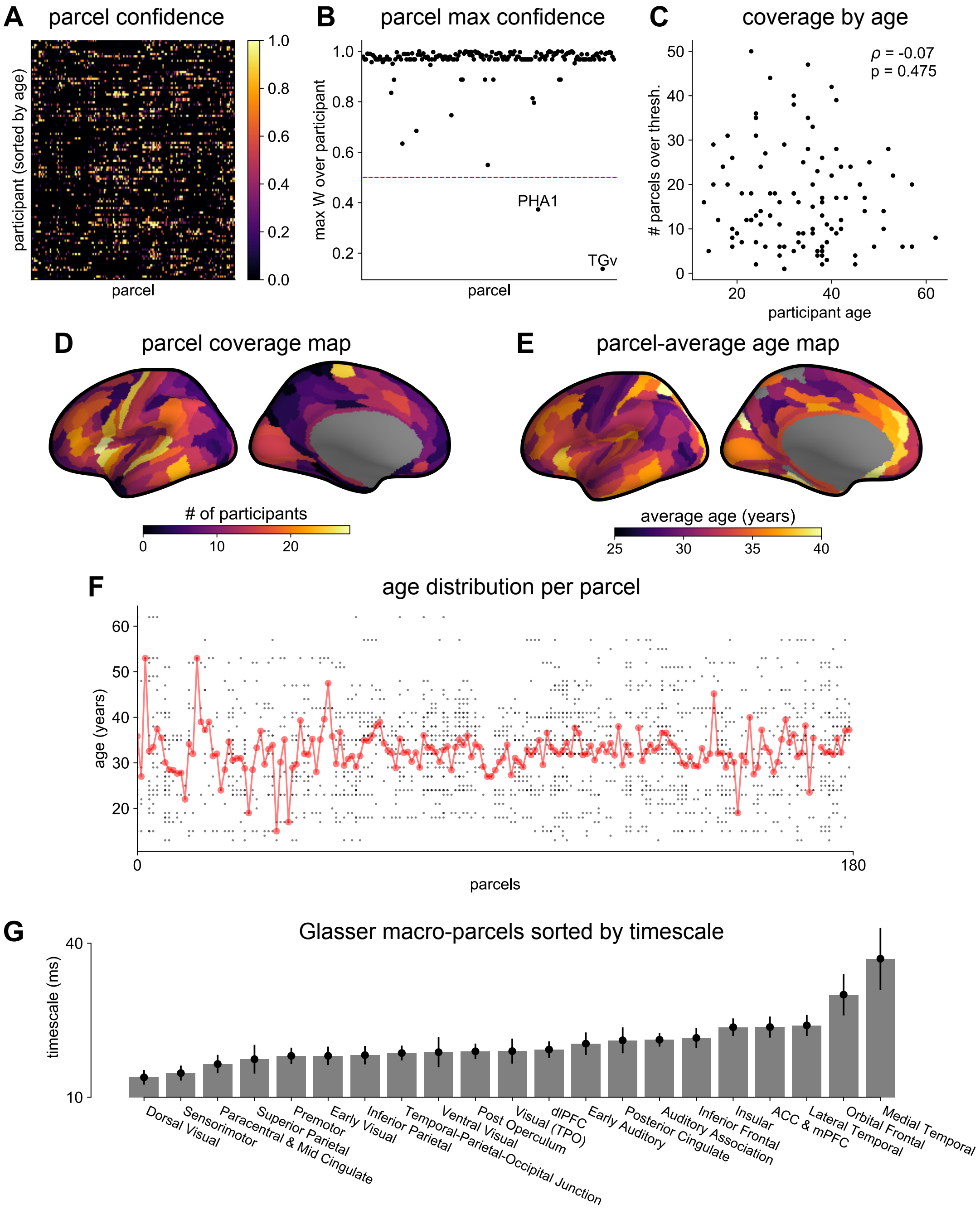
A
parcel confidence
participant (sorted by age)
parcel
0.0
0.2
0.4
0.6
0.8
1.0
B
parcel max confidence
max W over participant
parcel
PHA1
TGv
C
coverage by age
parcels over thresh.
participant age
ρ = -0.07
p = 0.475
D
parcel coverage map
# of participants
0
10
20
E
parcel-average age map
average age (years)
25
30
35
40
F
age distribution per parcel
age (years)
parcels
0
180
G
Glasser macro-parcels sorted by timescale
timescale (ms)
10
40
Dorsal Visual
Sensorimotor
Paracentral & Mid Cingulate
Superior Parietal
Premotor
Early Visual
Inferior Parietal
Temporal-Parietal-Occipital Junction
Ventral Visual
Post Operculum
Visual (TPO)
dlPFC
Early Auditory
Posterior Cingulate
Auditory Association
Inferior Frontal
Insular
ACC & mPFC
Lateral Temporal
Orbital Frontal
Medial Temporal

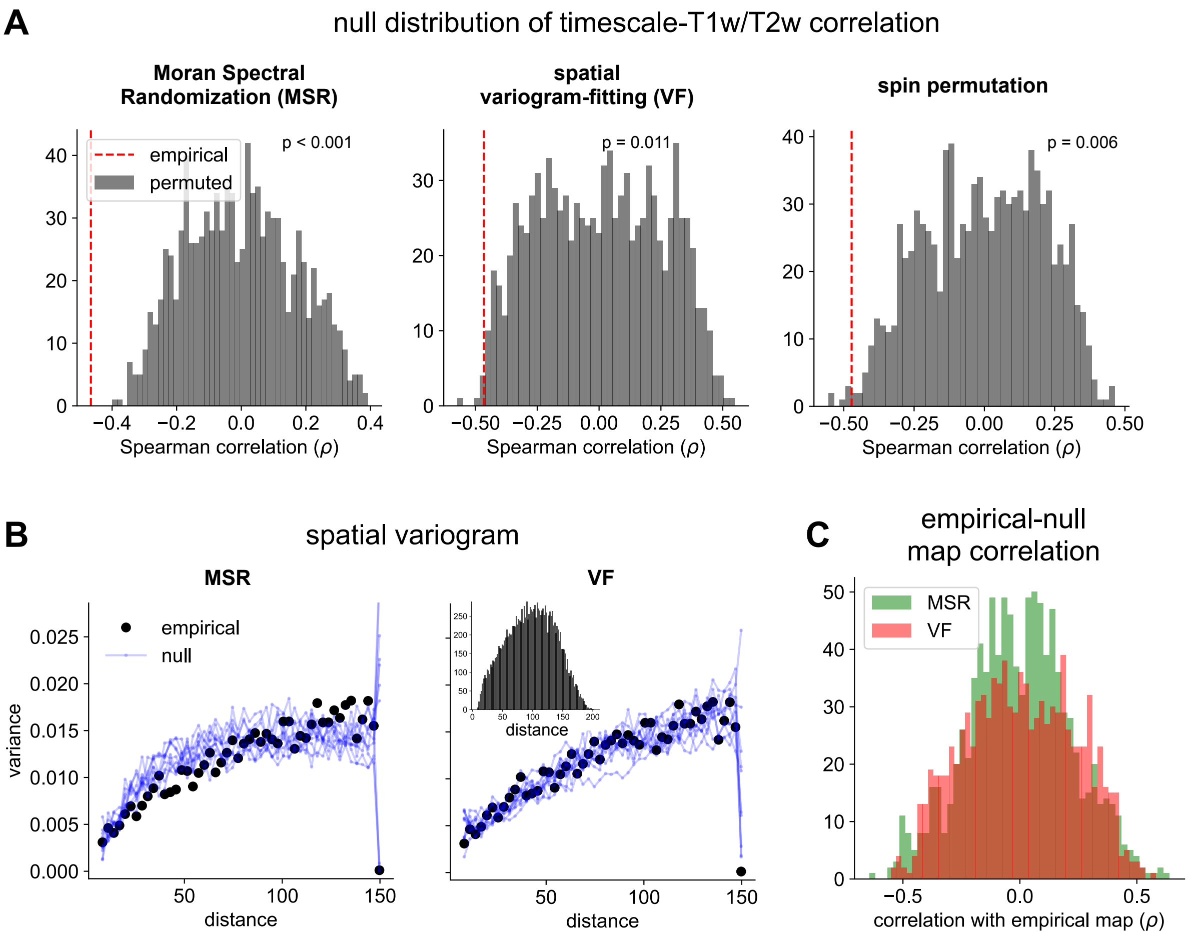

Figure 3.6: Figure 3.2—figure supplement 2. Comparison of spatial autocorrelation-preserving null map generation methods. (A) distributions of Spearman correlation values between empirical T1w/T2w map and 1000 spatial-autocorrelation preserving null timescale maps generated using Moran Spectral Randomization (MSR), spatial variogram fitting (VF), and spin permutation. Red dashed line denotes correlation between empirical timescale and T1w/T2w maps, p-values indicate two-tailed significance, i.e., proportion of distribution with values more extreme than empirical correlation. (B) spatial variogram for empirical timescale map (black) and 10 null maps (blue) generated using MSR (left) and VF (right). Inset shows distribution of distances between pairs of HCP-MMP parcels. (C) distribution of Spearman correlations between empirical and 1000 null timescale maps generated using MSR (green) and VF (red), showing similar levels of correlation between empirical and null maps for both methods.

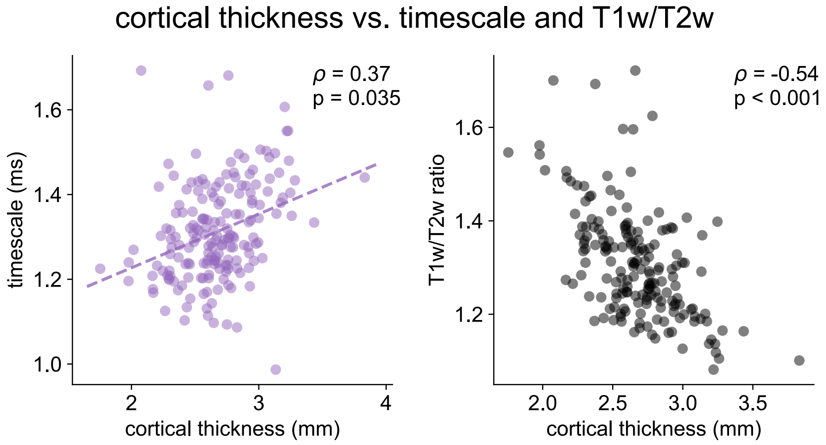

Figure 3.7: Figure 3.2—figure supplement 3. Cortical thickness. Cortical thickness from the HCP dataset is positively correlated with neuronal timescale (left), and negatively correlated with T1w/T2w, i.e., thicker brain regions have longer (slower) timescales and less grey matter myelination, corresponding to higher-order association areas.

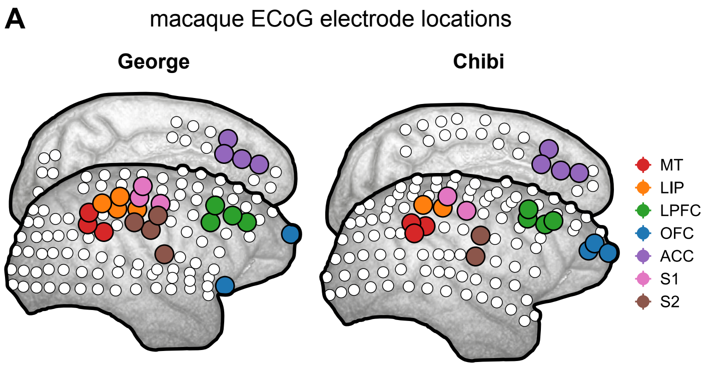

B indices of ECoG electrodes (1-based indexing)

	MT	LIP	LPFC	OFC	ACC	S1	S2
George	4, 13, 22	10, 11, 20, 21	15, 24, 25, 26	45, 66	52, 57, 58, 59	18, 19, 30	1, 2, 9, 108
Chibi	3, 4, 109	10, 11	15, 25, 25, 26	23, 34, 45	52, 57, 58, 59	9, 19	95, 108

Figure 3.8: Figure 3.2—figure supplement 4. Macaque ECoG and single-unit coverage. (A) locations of 180-electrode ECoG grid from 2 animals in the Neurotycho dataset, colors correspond to locations used for comparison with single-unit timescales. (B) electrode indices of the sampled areas from the two animals, corresponding to those colored in (A).

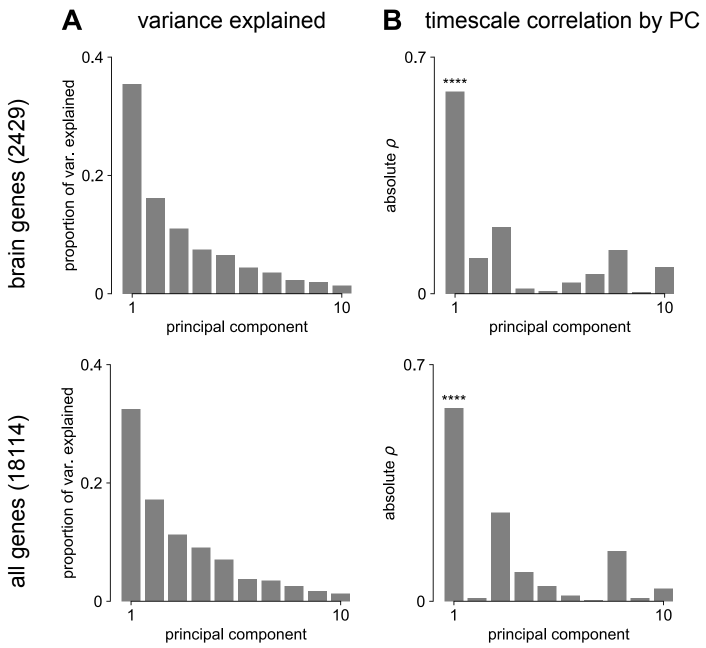

Figure 3.9: Figure 3.3—figure supplement 1. Transcriptomic PCA results. (A) proportion of variance explained by the top 10 principal components (PCs) of brain-specific genes (top) and all AHBA genes (bottom). (B) absolute Spearman correlation between timescale map and top 10 PCs from brain-specific or full gene dataset. Asterisks indicate resampled significance while accounting for spatial autocorrelation, **** indicate p < 0.001. Top PCs explain similar amounts of variance, while only PC1 in both cases is significantly correlated with timescale.

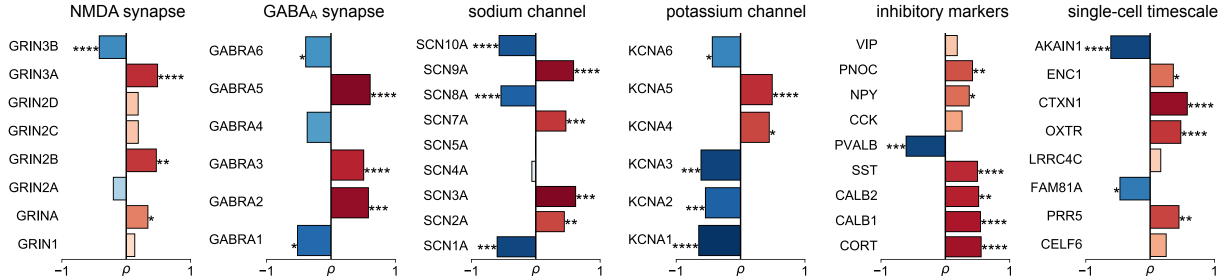

Figure 3.10: Figure 3.3—figure supplement 2. Individual timescale-gene correlations magnitudes. Correlation between timescale and expression of genes from Figure. 3.3C, with gene symbols labeled and grouped into functional families for ease of interpretation.

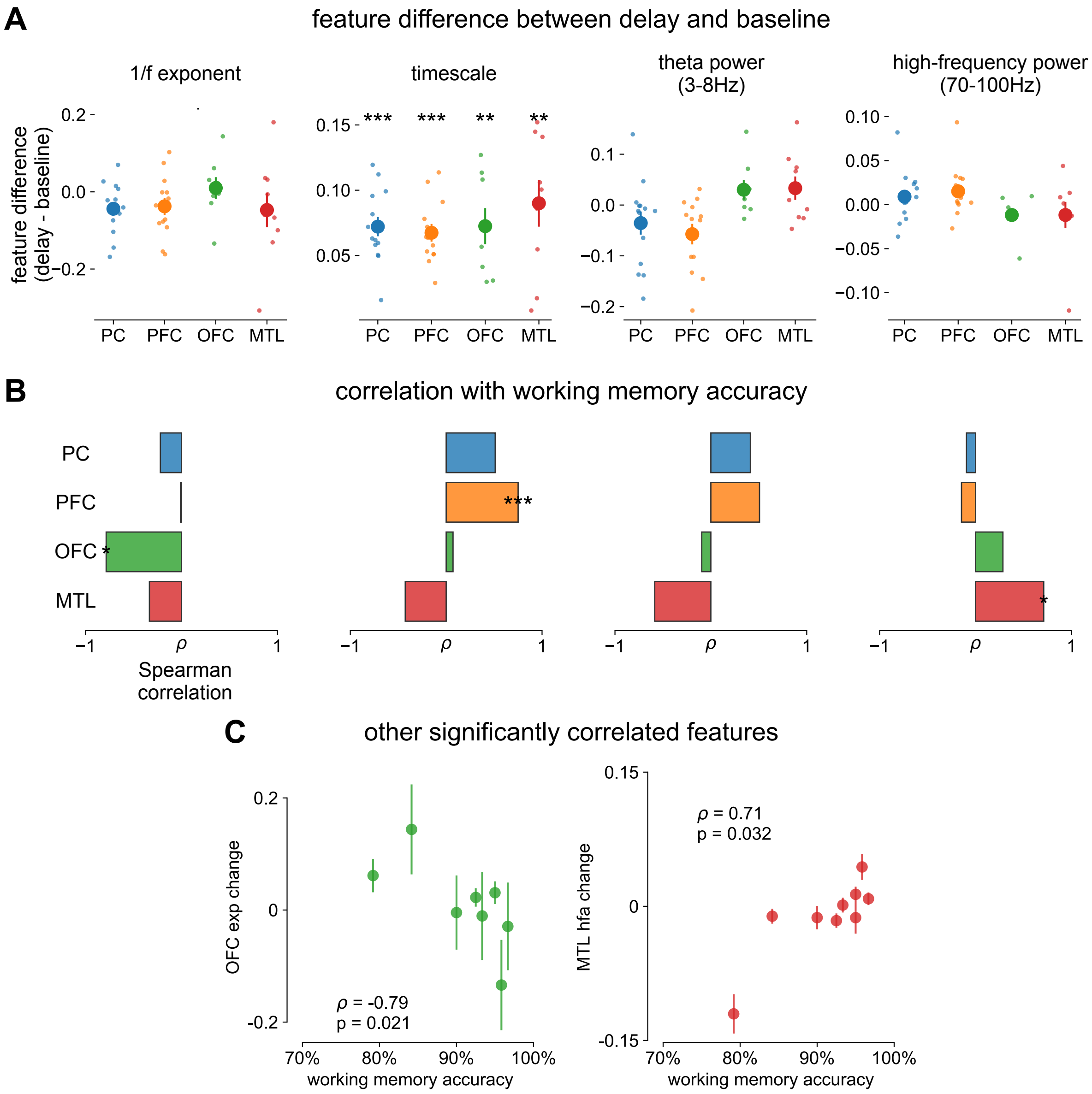

Figure 3.11: Figure 3.4—figure supplement 1. Spectral correlates of working memory performance. (A) difference between delay and baseline periods for 1/f-exponent, timescale (same as main Figure. 3.4C but absolute units on y-axis, instead of percentage), theta power, and high-frequency power. (B) Spearman correlation between spectral feature difference and working memory accuracy across participants, same features as in (A). * $p < 0.05$, ** $p < 0.01$, *** $p < 0.005$ in (A, B). (C) scatter plot of other significantly correlated spectral features from (B).

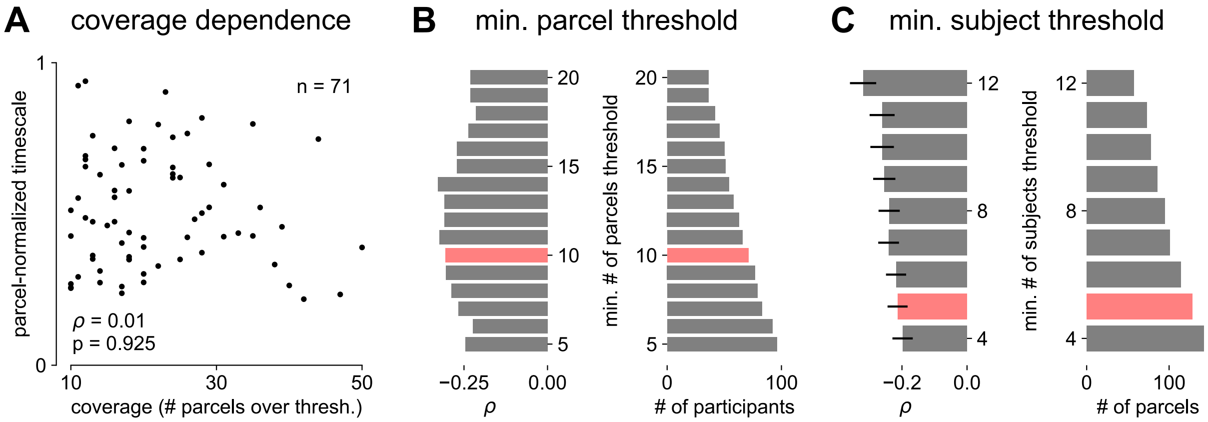

Figure 3.12: Figure 3.4—figure supplement 2. Parameter sensitivity for timescale-aging analysis. (A) cortex-averaged timescale is independent of parcel coverage across participants. (B) sensitivity analysis for the number of valid parcels a participant must have in order to be included in analysis for main Figure 3.4E (red). As threshold increases (more stringent), fewer participants satisfy the criteria (right) but correlation between participant age and timescale remains robust (left). (C) sensitivity analysis for the number of valid participants a parcel must have in order to be included in analysis for main Figure 3.4F. As threshold increases (more stringent), fewer parcels satisfy the criteria (right) but average correlation across all parcels remains robust (left, error bars denote s.e.m of distribution as in Figure 3.4F).

Table 3.3: **Supplementary File 1. Significant items from brain-specific GOEA. gene assoc.**: direction of association with timescale; "all" includes both positive and negative. **e/p**: enriched or purified; **ont.**: ontology: BP: biological process; CC: cellular components; MF: molecular function

gene assoc.	**ID**	**e/p**	**ont.**	**name**	**enrich. ratio**	**p-value (FDR-adjusted)**
all	GO:0034702	e	CC	ion channel complex	1.959	0.008
all	GO:1902495	e	CC	transmembrane transporter complex	1.91	0.008
all	GO:1990351	e	CC	transporter complex	1.91	0.008
all	GO:0098982	e	CC	GABA-ergic synapse	2.497	0.038
all	GO:1902711	e	CC	GABA-A receptor complex	4.541	0.038
all	GO:0034707	e	CC	chloride channel complex	3.385	0.038
pos	GO:0008195	e	MF	phosphatidate phosphatase activity	13.864	0.007
neg	GO:0098660	e	BP	inorganic ion transmembrane transport	2.515	0.002
neg	GO:0098662	e	BP	inorganic cation transmembrane transport	2.529	0.007
neg	GO:0098655	e	BP	cation transmembrane transport	2.439	0.007
neg	GO:0034220	e	BP	ion transmembrane transport	2.057	0.03
neg	GO:0030001	e	BP	metal ion transport	2.239	0.036
neg	GO:0071805	e	BP	potassium ion transmembrane transport	3.122	0.036
neg	GO:0006813	e	BP	potassium ion transport	3.081	0.037
neg	GO:1902495	e	CC	transmembrane transporter complex	2.334	0.009
neg	GO:1990351	e	CC	transporter complex	2.334	0.009
neg	GO:0034702	e	CC	ion channel complex	2.36	0.009
neg	GO:0098796	e	CC	membrane protein complex	2.063	0.009
neg	GO:0034703	e	CC	cation channel complex	2.379	0.03
neg	GO:0005244	e	MF	voltage-gated ion channel activity	3.081	0.002
neg	GO:0022832	e	MF	voltage-gated channel activity	3.081	0.002
neg	GO:0046873	e	MF	metal ion transmembrane transporter activity	2.453	0.002
neg	GO:0022890	e	MF	inorganic cation transmembrane transporter activity	2.24	0.005
neg	GO:0005216	e	MF	ion channel activity	2.289	0.006
neg	GO:0008324	e	MF	cation transmembrane transporter activity	2.173	0.006
neg	GO:0015318	e	MF	inorganic molecular entity transmembrane transporter activity	2.04	0.006
neg	GO:0015077	e	MF	monovalent inorganic cation transmembrane transporter activity	2.535	0.006
neg	GO:0015075	e	MF	ion transmembrane transporter activity	2.024	0.006

. . . Table 3.3 continued.

gene assoc.	ID	e/p	ont.	name	enrich. ratio	p-value (FDR-adjusted)
neg	GO:0015079	e	MF	potassium ion transmembrane transporter activity	3.041	0.006
neg	GO:0005215	e	MF	transporter activity	1.883	0.006
neg	GO:0022857	e	MF	transmembrane transporter activity	1.906	0.006
neg	GO:0022836	e	MF	gated channel activity	2.301	0.006
neg	GO:0015267	e	MF	channel activity	2.191	0.006
neg	GO:0022803	e	MF	passive transmembrane transporter activity	2.191	0.006
neg	GO:0005249	e	MF	voltage-gated potassium channel activity	3.658	0.006
neg	GO:0005261	e	MF	cation channel activity	2.353	0.009
neg	GO:0005267	e	MF	potassium channel activity	3.058	0.011
neg	GO:0022843	e	MF	voltage-gated cation channel activity	2.744	0.022

Table 3.4: **Supplementary File 2. Significant items from all-gene GOEA. gene assoc.**: direction of association with timescale; "all" includes both positive and negative. **e/p**: enriched or purified; **ont.**: ontology: BP: biological process; CC: cellular components; MF: molecular function

gene assoc.	**ID**	**e/p**	**ont.**	**name**	**enrich. ratio**	**p-value (FDR-adjusted)**
all	GO:0034702	e	CC	ion channel complex	1.83	0.008
all	GO:1990351	e	CC	transporter complex	1.774	0.008
all	GO:1902495	e	CC	transmembrane transporter complex	1.79	0.008
all	GO:0034703	e	CC	cation channel complex	1.952	0.009
all	GO:0098982	e	CC	GABA-ergic synapse	2.468	0.048
all	GO:1902711	e	CC	GABA-A receptor complex	5.035	0.048
pos	GO:0050866	e	BP	negative regulation of cell activation	3.596	0
pos	GO:0002376	e	BP	immune system process	1.629	0
pos	GO:0006955	e	BP	immune response	1.992	0
pos	GO:0002695	e	BP	negative regulation of leukocyte activation	3.343	0.001
pos	GO:0045087	e	BP	innate immune response	2.297	0.005
pos	GO:0050865	e	BP	regulation of cell activation	2.099	0.005
pos	GO:0045321	e	BP	leukocyte activation	1.834	0.006
pos	GO:0007165	e	BP	signal transduction	1.301	0.006
pos	GO:0051250	e	BP	negative regulation of lymphocyte activation	3.305	0.007
pos	GO:0070663	e	BP	regulation of leukocyte proliferation	2.82	0.007
pos	GO:0002252	e	BP	immune effector process	1.778	0.009
pos	GO:0050670	e	BP	regulation of lymphocyte proliferation	2.823	0.009
pos	GO:0032944	e	BP	regulation of mononuclear cell proliferation	2.807	0.009
pos	GO:0050776	e	BP	regulation of immune response	1.787	0.011
pos	GO:0002682	e	BP	regulation of immune system process	1.571	0.015
pos	GO:0046634	e	BP	regulation of alpha-beta T cell activation	3.772	0.016
pos	GO:0001775	e	BP	cell activation	1.709	0.016
pos	GO:0032956	e	BP	regulation of actin cytoskeleton organization	2.229	0.016
pos	GO:0003150	e	BP	muscular septum morphogenesis	17.672	0.016
pos	GO:0032945	e	BP	negative regulation of mononuclear cell proliferation	4.208	0.016
pos	GO:0050672	e	BP	negative regulation of lymphocyte proliferation	4.208	0.016
pos	GO:0006952	e	BP	defense response	1.686	0.016

. . . Table 3.4 continued.

gene as-soc.	ID	e/p	ont.	name	enrich. ratio	p-value (FDR-adjusted)
pos	GO:0002694	e	BP	regulation of leukocyte activation	2.013	0.016
pos	GO:0002253	e	BP	activation of immune response	2.183	0.016
pos	GO:0030833	e	BP	regulation of actin filament polymerization	2.832	0.016
pos	GO:0032970	e	BP	regulation of actin filament-based process	2.136	0.017
pos	GO:0002684	e	BP	positive regulation of immune system process	1.708	0.017
pos	GO:0046640	e	BP	regulation of alpha-beta T cell proliferation	6.094	0.017
pos	GO:0050868	e	BP	negative regulation of T cell activation	3.381	0.017
pos	GO:0002274	e	BP	myeloid leukocyte activation	1.926	0.017
pos	GO:0008064	e	BP	regulation of actin polymerization or depolymerization	2.697	0.017
pos	GO:0030832	e	BP	regulation of actin filament length	2.681	0.017
pos	GO:0006334	e	BP	nucleosome assembly	3.053	0.018
pos	GO:0070664	e	BP	negative regulation of leukocyte proliferation	3.956	0.018
pos	GO:0038096	e	BP	Fc-gamma receptor signaling pathway involved in phagocytosis	3.787	0.026
pos	GO:0002433	e	BP	immune response-regulating cell surface receptor signaling pathway involved in phagocytosis	3.787	0.026
pos	GO:0098883	e	BP	synapse pruning	10.041	0.027
pos	GO:0038094	e	BP	Fc-gamma receptor signaling pathway	3.734	0.029
pos	GO:0051249	e	BP	regulation of lymphocyte activation	2.035	0.029
pos	GO:0002431	e	BP	Fc receptor mediated stimulatory signaling pathway	3.682	0.03
pos	GO:0042116	e	BP	macrophage activation	4.734	0.03
pos	GO:0110053	e	BP	regulation of actin filament organization	2.279	0.03
pos	GO:0150064	e	BP	vertebrate eye-specific patterning	22.09	0.03
pos	GO:0002683	e	BP	negative regulation of immune system process	2.008	0.03
pos	GO:0051049	e	BP	regulation of transport	1.428	0.03
pos	GO:0098542	e	BP	defense response to other organism	1.811	0.033
pos	GO:0150146	e	BP	cell junction disassembly	9.204	0.033
pos	GO:0016322	e	BP	neuron remodeling	9.204	0.033

. . . Table 3.4 continued.

gene as-soc.	ID	e/p	ont.	name	enrich. ratio	p-value (FDR-adjusted)
pos	GO:1903038	e	BP	negative regulation of leukocyte cell-cell adhesion	3.04	0.033
pos	GO:0007166	e	BP	cell surface receptor signaling pathway	1.391	0.034
pos	GO:0034728	e	BP	nucleosome organization	2.591	0.037
pos	GO:0036336	e	BP	dendritic cell migration	6.976	0.037
pos	GO:0048584	e	BP	positive regulation of response to stimulus	1.379	0.039
pos	GO:0001774	e	BP	microglial cell activation	5.727	0.039
pos	GO:0002269	e	BP	leukocyte activation involved in inflammatory response	5.727	0.039
pos	GO:0050778	e	BP	positive regulation of immune response	1.82	0.039
pos	GO:2000112	p	BP	regulation of cellular macromolecule biosynthetic process	0.718	0.017
pos	GO:0051252	p	BP	regulation of RNA metabolic process	0.718	0.019
pos	GO:0044271	p	BP	cellular nitrogen compound biosynthetic process	0.554	0.029
pos	GO:0019219	p	BP	regulation of nucleobase-containing compound metabolic process	0.737	0.029
pos	GO:0090304	p	BP	nucleic acid metabolic process	0.654	0.037
pos	GO:0032993	e	CC	protein-DNA complex	2.829	0.016
pos	GO:0000786	e	CC	nucleosome	3.488	0.016
pos	GO:0005887	e	CC	integral component of plasma membrane	1.555	0.016
pos	GO:0031226	e	CC	intrinsic component of plasma membrane	1.536	0.016
pos	GO:0044815	e	CC	DNA packaging complex	3.217	0.023
pos	GO:0030666	e	CC	endocytic vesicle membrane	2.705	0.034
pos	GO:0031514	e	CC	motile cilium	2.897	0.034
pos	GO:0043235	e	CC	receptor complex	1.981	0.04
pos	GO:0000839	e	CC	Hrd1p ubiquitin ligase ERAD-L complex	11.045	0.047
pos	GO:0016021	e	CC	integral component of membrane	1.232	0.047
pos	GO:0005634	p	CC	nucleus	0.79	0.04
pos	GO:0003676	p	MF	nucleic acid binding	0.694	0.012
neg	GO:0006813	e	BP	potassium ion transport	2.911	0.004

. . . Table 3.4 continued.

gene assoc.	ID	e/p	ont.	name	enrich. ratio	p-value (FDR-adjusted)
neg	GO:0071805	e	BP	potassium ion transmembrane transport	2.868	0.008
neg	GO:0015079	e	MF	potassium ion transmembrane transporter activity	2.888	0.001
neg	GO:0015075	e	MF	ion transmembrane transporter activity	1.726	0.001
neg	GO:0022857	e	MF	transmembrane transporter activity	1.649	0.001
neg	GO:0046873	e	MF	metal ion transmembrane transporter activity	2.068	0.001
neg	GO:0005215	e	MF	transporter activity	1.587	0.002
neg	GO:0022832	e	MF	voltage-gated channel activity	2.468	0.006
neg	GO:0005244	e	MF	voltage-gated ion channel activity	2.468	0.006
neg	GO:0015318	e	MF	inorganic molecular entity transmembrane transporter activity	1.662	0.008
neg	GO:0001227	e	MF	DNA-binding transcription repressor activity, RNA polymerase II-specific	2.227	0.011
neg	GO:0001217	e	MF	DNA-binding transcription repressor activity	2.218	0.011
neg	GO:0022836	e	MF	gated channel activity	2.007	0.015
neg	GO:0005249	e	MF	voltage-gated potassium channel activity	3.126	0.015
neg	GO:0015077	e	MF	monovalent inorganic cation transmembrane transporter activity	1.916	0.022
neg	GO:0005267	e	MF	potassium channel activity	2.703	0.022
neg	GO:0022890	e	MF	inorganic cation transmembrane transporter activity	1.701	0.033

Table 3.5: **Supplementary File 3. Significant items from all-gene GOEA with T1w/T2w as control.** **gene assoc.**: direction of association with timescale; "all" includes both positive and negative. **e/p**: enriched or purified; **ont.**: ontology: BP: biological process; CC: cellular components; MF: molecular function

gene assoc.	ID	e/p	ont.	name	enrich. ratio	p-value (FDR-adjusted)
all	GO:1990351	e	CC	transporter complex	1.564	0.038
all	GO:1902495	e	CC	transmembrane transporter complex	1.563	0.038
all	GO:0034702	e	CC	ion channel complex	1.572	0.043
all	GO:1990904	p	CC	ribonucleoprotein complex	0.641	0.038
pos	GO:0006955	e	BP	immune response	1.647	0.001
pos	GO:0045087	e	BP	innate immune response	1.963	0.001
pos	GO:0002274	e	BP	myeloid leukocyte activation	1.789	0.001
pos	GO:0002376	e	BP	immune system process	1.383	0.001
pos	GO:0002684	e	BP	positive regulation of immune system process	1.607	0.001
pos	GO:0050865	e	BP	regulation of cell activation	1.778	0.002
pos	GO:0045321	e	BP	leukocyte activation	1.602	0.002
pos	GO:0042116	e	BP	macrophage activation	4.158	0.002
pos	GO:0050776	e	BP	regulation of immune response	1.605	0.002
pos	GO:0002694	e	BP	regulation of leukocyte activation	1.802	0.002
pos	GO:0050670	e	BP	regulation of lymphocyte proliferation	2.287	0.004
pos	GO:0002682	e	BP	regulation of immune system process	1.427	0.005
pos	GO:0070663	e	BP	regulation of leukocyte proliferation	2.256	0.005
pos	GO:0002253	e	BP	activation of immune response	1.905	0.005
pos	GO:0032944	e	BP	regulation of mononuclear cell proliferation	2.274	0.006
pos	GO:0150146	e	BP	cell junction disassembly	7.277	0.006
pos	GO:0050778	e	BP	positive regulation of immune response	1.697	0.006
pos	GO:0006898	e	BP	receptor-mediated endocytosis	2.296	0.007
pos	GO:0030833	e	BP	regulation of actin filament polymerization	2.319	0.008
pos	GO:0001775	e	BP	cell activation	1.504	0.008
pos	GO:0051249	e	BP	regulation of lymphocyte activation	1.806	0.009
pos	GO:0034314	e	BP	Arp2/3 complex-mediated actin nucleation	5.871	0.009
pos	GO:0002252	e	BP	immune effector process	1.521	0.009
pos	GO:0050866	e	BP	negative regulation of cell activation	2.248	0.009
pos	GO:0001774	e	BP	microglial cell activation	4.62	0.009
pos	GO:0045010	e	BP	actin nucleation	4.62	0.009

. . . Table 3.5 continued.

gene assoc.	ID	e/p	ont.	name	enrich. ratio	p-value (FDR-adjusted)
pos	GO:0002269	e	BP	leukocyte activation involved in inflammatory response	4.62	0.009
pos	GO:0032940	e	BP	secretion by cell	1.49	0.011
pos	GO:0045055	e	BP	regulated exocytosis	1.598	0.012
pos	GO:0140352	e	BP	export from cell	1.475	0.012
pos	GO:0002697	e	BP	regulation of immune effector process	1.787	0.019
pos	GO:0032103	e	BP	positive regulation of response to external stimulus	1.702	0.02
pos	GO:0002366	e	BP	leukocyte activation involved in immune response	1.621	0.02
pos	GO:0006887	e	BP	exocytosis	1.539	0.021
pos	GO:0098754	e	BP	detoxification	2.45	0.021
pos	GO:0051046	e	BP	regulation of secretion	1.505	0.024
pos	GO:0050863	e	BP	regulation of T cell activation	1.865	0.025
pos	GO:0098883	e	BP	synapse pruning	6.805	0.025
pos	GO:1903530	e	BP	regulation of secretion by cell	1.521	0.025
pos	GO:0002263	e	BP	cell activation involved in immune response	1.609	0.026
pos	GO:0048584	e	BP	positive regulation of response to stimulus	1.284	0.027
pos	GO:0043299	e	BP	leukocyte degranulation	1.656	0.027
pos	GO:0038096	e	BP	Fc-gamma receptor signaling pathway involved in phagocytosis	2.851	0.027
pos	GO:0002433	e	BP	immune response-regulating cell surface receptor signaling pathway involved in phagocytosis	2.851	0.027
pos	GO:0002695	e	BP	negative regulation of leukocyte activation	2.216	0.029
pos	GO:0016192	e	BP	vesicle-mediated transport	1.33	0.03
pos	GO:0002275	e	BP	myeloid cell activation involved in immune response	1.64	0.03
pos	GO:0038094	e	BP	Fc-gamma receptor signaling pathway	2.811	0.03
pos	GO:0002696	e	BP	positive regulation of leukocyte activation	1.84	0.031
pos	GO:0032722	e	BP	positive regulation of chemokine production	3.18	0.033
pos	GO:0002431	e	BP	Fc receptor mediated stimulatory signaling pathway	2.772	0.033

. . . Table 3.5 continued.

gene assoc.	ID	e/p	ont.	name	enrich. ratio	p-value (FDR-adjusted)
pos	GO:0009607	e	BP	response to biotic stimulus	1.432	0.033
pos	GO:0043207	e	BP	response to external biotic stimulus	1.435	0.035
pos	GO:0016322	e	BP	neuron remodeling	6.238	0.035
pos	GO:0008064	e	BP	regulation of actin polymerization or depolymerization	2.103	0.037
pos	GO:0030832	e	BP	regulation of actin filament length	2.091	0.038
pos	GO:1903037	e	BP	regulation of leukocyte cell-cell adhesion	1.821	0.04
pos	GO:0032930	e	BP	positive regulation of superoxide anion generation	5.137	0.041
pos	GO:0042129	e	BP	regulation of T cell proliferation	2.202	0.042
pos	GO:0055069	e	BP	zinc ion homeostasis	4.01	0.045
pos	GO:0042534	e	BP	regulation of tumor necrosis factor biosynthetic process	4.01	0.045
pos	GO:0061900	e	BP	glial cell activation	3.669	0.046
pos	GO:0002283	e	BP	neutrophil activation involved in immune response	1.627	0.046
pos	GO:0042119	e	BP	neutrophil activation	1.626	0.049
pos	GO:0051252	p	BP	regulation of RNA metabolic process	0.704	0
pos	GO:2000112	p	BP	regulation of cellular macromolecule biosynthetic process	0.711	0
pos	GO:2001141	p	BP	regulation of RNA biosynthetic process	0.704	0
pos	GO:0019219	p	BP	regulation of nucleobase-containing compound metabolic process	0.729	0
pos	GO:1903506	p	BP	regulation of nucleic acid-templated transcription	0.705	0
pos	GO:0010556	p	BP	regulation of macromolecule biosynthetic process	0.733	0
pos	GO:0006355	p	BP	regulation of transcription, DNA-templated	0.713	0
pos	GO:0010468	p	BP	regulation of gene expression	0.77	0
pos	GO:0031326	p	BP	regulation of cellular biosynthetic process	0.757	0.001
pos	GO:0080090	p	BP	regulation of primary metabolic process	0.812	0.001
pos	GO:0009889	p	BP	regulation of biosynthetic process	0.769	0.001

. . . Table 3.5 continued.

gene as-soc.	ID	e/p	ont.	name	enrich. ratio	p-value (FDR-adjusted)
pos	GO:0060255	p	BP	regulation of macromolecule metabolic process	0.829	0.002
pos	GO:0051171	p	BP	regulation of nitrogen compound metabolic process	0.819	0.002
pos	GO:0019222	p	BP	regulation of metabolic process	0.846	0.005
pos	GO:0031323	p	BP	regulation of cellular metabolic process	0.837	0.006
pos	GO:0090304	p	BP	nucleic acid metabolic process	0.739	0.029
pos	GO:0005887	e	CC	integral component of plasma membrane	1.417	0.016
pos	GO:0031226	e	CC	intrinsic component of plasma membrane	1.396	0.016
pos	GO:0005885	e	CC	Arp2/3 protein complex	7.485	0.017
pos	GO:0030666	e	CC	endocytic vesicle membrane	2.291	0.017
pos	GO:0070062	e	CC	extracellular exosome	1.285	0.042
pos	GO:1903561	e	CC	extracellular vesicle	1.279	0.042
pos	GO:0043230	e	CC	extracellular organelle	1.278	0.042
pos	GO:0016021	e	CC	integral component of membrane	1.173	0.042
pos	GO:0031224	e	CC	intrinsic component of membrane	1.165	0.043
pos	GO:0098797	e	CC	plasma membrane protein complex	1.559	0.043
pos	GO:0005634	p	CC	nucleus	0.803	0.004
pos	GO:0043229	p	CC	intracellular organelle	0.905	0.042
pos	GO:0043231	p	CC	intracellular membrane-bounded organelle	0.891	0.043
pos	GO:0000785	p	CC	chromatin	0.633	0.043
pos	GO:0003676	p	MF	nucleic acid binding	0.69	0
pos	GO:0097159	p	MF	organic cyclic compound binding	0.78	0
pos	GO:1901363	p	MF	heterocyclic compound binding	0.779	0
pos	GO:0003677	p	MF	DNA binding	0.687	0.001
pos	GO:0140110	p	MF	transcription regulator activity	0.636	0.004
pos	GO:0003700	p	MF	DNA-binding transcription factor activity	0.592	0.008
neg	GO:0034220	e	BP	ion transmembrane transport	1.619	0.013
neg	GO:0006820	e	BP	anion transport	1.785	0.013
neg	GO:0006811	e	BP	ion transport	1.486	0.013
neg	GO:0055085	e	BP	transmembrane transport	1.486	0.015
neg	GO:0098660	e	BP	inorganic ion transmembrane transport	1.674	0.035
neg	GO:0098656	e	BP	anion transmembrane transport	2.067	0.04

. . . Table 3.5 continued.

gene assoc.	**ID**	**e/p**	**ont.**	**name**	**enrich. ratio**	**p-value (FDR-adjusted)**
neg	GO:0006813	e	BP	potassium ion transport	2.359	0.046
neg	GO:0015075	e	MF	ion transmembrane transporter activity	1.702	0
neg	GO:0005215	e	MF	transporter activity	1.58	0
neg	GO:0022857	e	MF	transmembrane transporter activity	1.615	0
neg	GO:0046873	e	MF	metal ion transmembrane transporter activity	1.978	0
neg	GO:0015318	e	MF	inorganic molecular entity transmembrane transporter activity	1.67	0.001
neg	GO:0008509	e	MF	anion transmembrane transporter activity	1.983	0.007
neg	GO:0015079	e	MF	potassium ion transmembrane transporter activity	2.341	0.031
neg	GO:0022890	e	MF	inorganic cation transmembrane transporter activity	1.625	0.045
neg	GO:0008514	e	MF	organic anion transmembrane transporter activity	2.111	0.045

Bibliography

Alexander-Bloch, A. F., Shou, H., Liu, S., Satterthwaite, T. D., Glahn, D. C., Shinohara, R. T., Vandekar, S. N., & Raznahan, A. (2018). On testing for spatial correspondence between maps of human brain structure and function. Neuroimage, 178, 540–551.

Badre, D. & D'Esposito, M. (2009). Is the rostro-caudal axis of the frontal lobe hierarchical? Nat. Rev. Neurosci., 10, 659–669.

Baldassano, C., Chen, J., Zadbood, A., Pillow, J. W., Hasson, U., & Norman, K. A. (2017). Discovering event structure in continuous narrative perception and memory. Neuron, 95, 709–721.e5.

Bomkamp, C., Tripathy, S. J., Bengtsson Gonzales, C., Hjerling-Leffler, J., Craig, A. M., & Pavlidis, P. (2019). Transcriptomic correlates of electrophysiological and morphological diversity within and across excitatory and inhibitory neuron classes. PLoS Comput. Biol., 15, e1007113.

Breakspear, M. (2017). Dynamic models of large-scale brain activity. Nat. Neurosci., 20, 340–352.

Brett, M., Markiewicz, C. J., Hanke, M., Côté, M.-A., Cipollini, B., McCarthy, P., Jarecka, D., Cheng, C. P., Halchenko, Y. O., Cottaar, M., Ghosh, S., Larson, E., Wassermann, D., Gerhard, S., Lee, G. R., Wang, H.-T., Kastman, E., Kaczmarzyk, J., Guidotti, R., Duek, O., Rokem, A., Madison, C., Morency, F. C., Moloney, B., Goncalves, M., Markello, R., Riddell, C., Burns, C., Millman, J., Gramfort, A., Leppäkangas, J., Sólon, A., van den Bosch, J. J. F., Vincent, R. D., Braun, H., Subramaniam, K., Gorgolewski, K. J., Raamana, P. R., Nichols, B. N., Baker, E. M., Hayashi, S., Pinsard, B., Haselgrove, C., Hymers, M., Esteban, O., Koudoro, S., Oosterhof, N. N., Amirbekian, B., Nimmo-Smith, I., Nguyen, L., Reddigari, S., St-Jean, S., Panfilov, E., Garyfallidis, E., Varoquaux, G., Legarreta, J. H., Hahn, K. S., Hinds, O. P., Fauber, B., Poline, J.-B., Stutters, J., Jordan, K., Cieslak, M., Moreno, M. E., Haenel, V., Schwartz, Y., Baratz, Z., Darwin, B. C., Thirion, B., Papadopoulos Orfanos, D., Pérez-García, F., Solovey, I., Gonzalez, I., Palasubramaniam, J., Lecher, J., Leinweber, K., Raktivan, K., Fischer, P., Gervais, P., Gadde, S., Ballinger, T., Roos, T., Reddam, V. R., & freec (2020). nipy/nibabel: 3.1.0.

Brunel, N. (2000). Dynamics of sparsely connected networks of excitatory and inhibitory spiking neurons. J. Comput. Neurosci., 8, 183–208.

Brunel, N. & Wang, X.-J. (2003). What determines the frequency of fast network oscillations with irregular neural discharges? i. synaptic dynamics and excitation-inhibition balance. J. Neurophysiol., 90, 415–430.

Burt, J. B., Demirtaş, M., Eckner, W. J., Navejar, N. M., Ji, J. L., Martin, W. J., Bernacchia, A., Anticevic, A., & Murray, J. D. (2018). Hierarchy of transcriptomic specialization across human cortex captured by structural neuroimaging topography. Nat. Neurosci., 21, 1251–1259.

Burt, J. B., Helmer, M., Shinn, M., Anticevic, A., & Murray, J. D. (2020). Generative modeling of brain maps with spatial autocorrelation.

Buzsáki, G., Anastassiou, C. A., & Koch, C. (2012). The origin of extracellular fields and currents–EEG, ECoG, LFP and spikes. Nat. Rev. Neurosci., 13, 407–420.

Chaudhuri, R., He, B. J., & Wang, X.-J. (2017). Random recurrent networks near criticality capture the broadband power distribution of human ECoG dynamics. Cereb. Cortex, 8, 1–13.

Chaudhuri, R., Knoblauch, K., Gariel, M.-A., Kennedy, H., & Wang, X.-J. (2015). A Large-Scale circuit mechanism for hierarchical dynamical processing in the primate cortex. Neuron, 88, 419–431.

Chien, H.-Y. S. & Honey, C. J. (2020). Constructing and forgetting temporal context in the human cerebral cortex. Neuron.

Cole, S., Donoghue, T., Gao, R., & Voytek, B. (2019). NeuroDSP: a package for neural digital signal processing. Journal of Open Source Software, 4, 1272.

Davis, S. W., Dennis, N. A., Daselaar, S. M., Fleck, M. S., & Cabeza, R. (2008). Que PASA? the posterior–anterior shift in aging. Cereb. Cortex, 18, 1201–1209.

de Villers-Sidani, E., Alzghoul, L., Zhou, X., Simpson, K. L., Lin, R. C. S., & Merzenich, M. M. (2010). Recovery of functional and structural age-related changes in the rat primary auditory cortex with operant training. Proc. Natl. Acad. Sci. U. S. A., 107, 13900–13905.

Demirtaş, M., Burt, J. B., Helmer, M., Ji, J. L., Adkinson, B. D., Glasser, M. F., Van Essen, D. C., Sotiropoulos, S. N., Anticevic, A., & Murray, J. D. (2019). Hierarchical heterogeneity across human cortex shapes Large-Scale neural dynamics. Neuron, 101, 1181–1194.e13.

Donoghue, T., Haller, M., Peterson, E. J., Varma, P., Sebastian, P., Gao, R., Noto, T., Lara, A. H., Wallis, J. D., Knight, R. T., Shestyuk, A., & Voytek, B. (2020). Parameterizing neural power spectra into periodic and aperiodic components. Nat. Neurosci., 23, 1655–1665.

Dotson, N. M., Hoffman, S. J., Goodell, B., & Gray, C. M. (2018). Feature-Based visual Short-Term memory is widely distributed and hierarchically organized. Neuron, 99, 215–226.e4.

Duarte, R. & Morrison, A. (2019). Leveraging heterogeneity for neural computation with fading memory in layer 2/3 cortical microcircuits. PLoS Comput. Biol., 15, e1006781.

Duarte, R., Seeholzer, A., Zilles, K., & Morrison, A. (2017). Synaptic patterning and the timescales of cortical dynamics. Curr. Opin. Neurobiol., 43, 156–165.

Eyre, M. D., Renzi, M., Farrant, M., & Nusser, Z. (2012). Setting the time course of inhibitory synaptic currents by mixing multiple GABA(A) receptor α subunit isoforms. J. Neurosci., 32, 5853–5867.

Fagerberg, L., Hallström, B. M., Oksvold, P., Kampf, C., Djureinovic, D., Odeberg, J., Habuka, M., Tahmasebpoor, S., Danielsson, A., Edlund, K., Asplund, A., Sjöstedt, E., Lundberg, E., Szigyarto, C. A.-K., Skogs, M., Takanen, J. O., Berling, H., Tegel, H., Mulder, J., Nilsson, P., Schwenk, J. M., Lindskog, C., Danielsson, F., Mardinoglu, A., Sivertsson, A., von Feilitzen, K., Forsberg, M., Zwahlen, M., Olsson, I., Navani, S., Huss, M., Nielsen, J., Ponten, F., & Uhlén, M. (2014). Analysis of the human tissue-specific expression by genome-wide integration of transcriptomics and antibody-based proteomics. Mol. Cell. Proteomics, 13, 397–406.

Felleman, D. J. & Van Essen, D. C. (1991). Distributed hierarchical processing in the primate cerebral cortex. Cereb. Cortex, 1, 1–47.

Flint, A. C., Maisch, U. S., Weishaupt, J. H., Kriegstein, A. R., & Monyer, H. (1997). NR2A subunit expression shortens NMDA receptor synaptic currents in developing neocortex. J. Neurosci., 17, 2469–2476.

Fornito, A., Arnatkevičiūtė, A., & Fulcher, B. D. (2019). Bridging the gap between connectome and transcriptome. Trends Cogn. Sci., 23, 34–50.

Frauscher, B., von Ellenrieder, N., Zelmann, R., Doležalová, I., Minotti, L., Olivier, A., Hall, J., Hoffmann, D., Nguyen, D. K., Kahane, P., Dubeau, F., & Gotman, J. (2018a). Atlas of the normal intracranial electroencephalogram: neurophysiological awake activity in different cortical areas. Brain, 141, 1130–1144.

Frauscher, B., von Ellenrieder, N., Zelmann, R., Rogers, C., Nguyen, D. K., Kahane, P., Dubeau, F., & Gotman, J. (2018b). High-Frequency oscillations in the normal human brain. Ann. Neurol., 84, 374–385.

Freeman, W. J. (2000). Mesoscopic neurodynamics: from neuron to brain. J. Physiol. Paris, 94, 303–322.

Freeman, W. J. & Erwin, H. (2008). Freeman k-set. Scholarpedia J., 3, 3238.

Ganupuru, P., Goldring, A. B., Harun, R., & Hanks, T. D. (2019). Flexibility of timescales of evidence evaluation for decision making. Curr. Biol., 29, 2091–2097.e4.

Gao, R., Peterson, E. J., & Voytek, B. (2017). Inferring synaptic excitation/inhibition balance from field potentials. Neuroimage, 158, 70–78.

Genovese, G., Fromer, M., Stahl, E. A., Ruderfer, D. M., Chambert, K., Landén, M., Moran, J. L., Purcell, S. M., Sklar, P., Sullivan, P. F., Hultman, C. M., & McCarroll, S. A. (2016). Increased burden of ultra-rare protein-altering variants among 4,877 individuals with schizophrenia. Nat. Neurosci., 19, 1433–1441.

Gjorgjieva, J., Drion, G., & Marder, E. (2016). Computational implications of biophysical diversity and multiple timescales in neurons and synapses for circuit performance. Curr. Opin. Neurobiol., 37, 44–52.

Glasser, M. F., Coalson, T. S., Robinson, E. C., Hacker, C. D., Harwell, J., Yacoub, E., Ugurbil, K., Andersson, J., Beckmann, C. F., Jenkinson, M., Smith, S. M., & Van Essen, D. C. (2016). A multi-modal parcellation of human cerebral cortex. Nature, 536, 171–178.

Glasser, M. F. & Van Essen, D. C. (2011). Mapping human cortical areas in vivo based on myelin content as revealed by T1- and t2-weighted MRI. J. Neurosci., 31, 11597–11616.

Gold, J. I. & Shadlen, M. N. (2007). The neural basis of decision making. Annu. Rev. Neurosci., 30, 535–574.

Goulas, A., Changeux, J.-P., Wagstyl, K., Amunts, K., Palomero-Gallagher, N., & Hilgetag, C. C. (2020). The natural axis of transmitter receptor distribution in the human cerebral cortex.

Gryglewski, G., Seiger, R., James, G. M., Godbersen, G. M., Komorowski, A., Unterholzner, J., Michenthaler, P., Hahn, A., Wadsak, W., Mitterhauser, M., Kasper, S., & Lanzenberger, R. (2018). Spatial analysis and high resolution mapping of the human whole-brain transcriptome for integrative analysis in neuroimaging. Neuroimage, 176, 259–267.

Hawrylycz, M., Miller, J. A., Menon, V., Feng, D., Dolbeare, T., Guillozet-Bongaarts, A. L., Jegga, A. G., Aronow, B. J., Lee, C.-K., Bernard, A., Glasser, M. F., Dierker, D. L., Menche, J., Szafer, A., Collman, F., Grange, P., Berman, K. A., Mihalas, S., Yao, Z., Stewart, L., Barabási, A.-L., Schulkin, J., Phillips, J., Ng, L., Dang, C., Haynor, D. R., Jones, A., Van Essen, D. C., Koch, C., & Lein, E. (2015). Canonical genetic signatures of the adult human brain. Nat. Neurosci., 18, 1832–1844.

Hawrylycz, M. J., Lein, E. S., Guillozet-Bongaarts, A. L., Shen, E. H., Ng, L., Miller, J. A., van de Lagemaat, L. N., Smith, K. A., Ebbert, A., Riley, Z. L., Abajian, C., Beckmann, C. F., Bernard, A., Bertagnolli, D., Boe, A. F., Cartagena, P. M., Chakravarty, M. M., Chapin, M., Chong, J., Dalley, R. A., David Daly, B., Dang, C., Datta, S., Dee, N., Dolbeare, T. A., Faber, V., Feng, D., Fowler, D. R., Goldy, J., Gregor, B. W., Haradon, Z., Haynor, D. R., Hohmann, J. G., Horvath, S., Howard, R. E., Jeromin, A., Jochim, J. M., Kinnunen, M., Lau, C., Lazarz, E. T., Lee, C., Lemon, T. A., Li, L., Li, Y., Morris, J. A., Overly, C. C., Parker, P. D., Parry, S. E., Reding, M., Royall, J. J., Schulkin, J., Sequeira, P. A., Slaughterbeck, C. R., Smith, S. C., Sodt, A. J., Sunkin, S. M., Swanson, B. E., Vawter, M. P., Williams, D., Wohnoutka, P., Zielke, H. R., Geschwind, D. H., Hof, P. R., Smith, S. M., Koch, C., Grant, S. G. N., & Jones, A. R. (2012). An anatomically comprehensive atlas of the adult human brain transcriptome. Nature, 489, 391–399.

He, B. J., Zempel, J. M., Snyder, A. Z., & Raichle, M. E. (2010). The temporal structures and functional significance of scale-free brain activity. Neuron, 66, 353–369.

Hilgetag, C. C. & Goulas, A. (2020). 'hierarchy' in the organization of brain networks. Philos. Trans. R. Soc. Lond. B Biol. Sci., 375, 20190319.

Honey, C. J., Thesen, T., Donner, T. H., Silbert, L. J., Carlson, C. E., Devinsky, O., Doyle, W. K., Rubin, N., Heeger, D. J., & Hasson, U. (2012). Slow cortical dynamics and the accumulation of information over long timescales. Neuron, 76, 423–434.

Huang, C. & Doiron, B. (2017). Once upon a (slow) time in the land of recurrent neuronal networks…. Curr. Opin. Neurobiol., 46, 31–38.

Huntenburg, J. M., Bazin, P.-L., & Margulies, D. S. (2018). Large-Scale gradients in human cortical organization. Trends Cogn. Sci., 22, 21–31.

Izhikevich, L., Gao, R., Peterson, E., & Voytek, B. (2018). Measuring the average power of neural oscillations.

Johnson, E. (2018). Intracranial EEG recordings of medial temporal, lateral frontal, and orbitofrontal regions in 10 human adults performing a visuospatial working memory task.

Johnson, E. (2019). Intracranial EEG recordings of lateral frontal and parietal regions in 7 human adults performing a visuospatial working memory task.

Johnson, E. L., Adams, J. N., Solbakk, A.-K., Endestad, T., Larsson, P. G., Ivanovic, J., Meling, T. R., Lin, J. J., & Knight, R. T. (2018a). Dynamic frontotemporal systems process space and time in working memory. PLoS Biol., 16, e2004274.

Johnson, E. L., King-Stephens, D., Weber, P. B., Laxer, K. D., Lin, J. J., & Knight, R. T. (2018b). Spectral imprints of working memory for everyday associations in the frontoparietal network. Front. Syst. Neurosci., 12, 65.

Khintchine, A. (1934). Korrelationstheorie der stationären stochastischen prozesse. Math. Ann., 109, 604–615.

Kiebel, S. J., Daunizeau, J., & Friston, K. J. (2008). A hierarchy of time-scales and the brain. PLoS Comput. Biol., 4, e1000209.

Klopfenstein, D. V., Zhang, L., Pedersen, B. S., Ramírez, F., Warwick Vesztrocy, A., Naldi, A., Mungall, C. J., Yunes, J. M., Botvinnik, O., Weigel, M., Dampier, W., Dessimoz, C., Flick, P., & Tang, H. (2018). GOATOOLS: A python library for gene ontology analyses. Sci. Rep., 8, 10872.

Koch, C., Rapp, M., & Segev, I. (1996). A brief history of time (constants). Cereb. Cortex, 6, 93–101.

Lein, E. S., Hawrylycz, M. J., Ao, N., Ayres, M., Bensinger, A., Bernard, A., Boe, A. F., Boguski, M. S., Brockway, K. S., Byrnes, E. J., Chen, L., Chen, L., Chen, T.-M., Chin, M. C., Chong, J., Crook, B. E., Czaplinska, A., Dang, C. N., Datta, S., Dee, N. R., Desaki, A. L., Desta, T., Diep, E., Dolbeare, T. A., Donelan, M. J., Dong, H.-W., Dougherty, J. G., Duncan, B. J., Ebbert, A. J., Eichele, G., Estin, L. K., Faber, C., Facer, B. A., Fields, R., Fischer, S. R., Fliss, T. P., Frensley, C., Gates, S. N., Glattfelder, K. J., Halverson, K. R., Hart, M. R., Hohmann, J. G., Howell, M. P., Jeung, D. P., Johnson, R. A., Karr, P. T., Kawal, R., Kidney, J. M., Knapik, R. H., Kuan, C. L., Lake, J. H., Laramee, A. R., Larsen, K. D., Lau, C., Lemon, T. A., Liang, A. J., Liu, Y., Luong, L. T., Michaels, J., Morgan, J. J., Morgan, R. J., Mortrud, M. T., Mosqueda, N. F., Ng, L. L., Ng, R., Orta, G. J., Overly, C. C., Pak, T. H., Parry, S. E., Pathak, S. D., Pearson, O. C., Puchalski, R. B., Riley, Z. L., Rockett, H. R., Rowland, S. A., Royall, J. J., Ruiz, M. J., Sarno, N. R., Schaffnit, K., Shapovalova, N. V., Sivisay, T., Slaughterbeck, C. R., Smith, S. C., Smith, K. A., Smith, B. I., Sodt, A. J., Stewart, N. N., Stumpf, K.-R., Sunkin, S. M., Sutram, M., Tam, A., Teemer, C. D., Thaller, C., Thompson, C. L., Varnam, L. R., Visel, A., Whitlock, R. M., Wohnoutka, P. E., Wolkey, C. K., Wong, V. Y., Wood, M., Yaylaoglu, M. B., Young, R. C., Youngstrom, B. L., Yuan, X. F., Zhang, B., Zwingman, T. A., & Jones, A. R. (2007). Genome-wide atlas of gene expression in the adult mouse brain. Nature, 445, 168–176.

Lerner, Y., Honey, C. J., Silbert, L. J., & Hasson, U. (2011). Topographic mapping of a hierarchy of temporal receptive windows using a narrated story. J. Neurosci., 31, 2906–2915.

Liu, Y., Beyer, A., & Aebersold, R. (2016). On the dependency of cellular protein levels on mRNA abundance. Cell, 165, 535–550.

Mahjoory, K., Schoffelen, J.-M., Keitel, A., & Gross, J. (2020). The frequency gradient of human resting-state brain oscillations follows cortical hierarchies. Elife, 9.

Margulies, D. S., Ghosh, S. S., Goulas, A., Falkiewicz, M., Huntenburg, J. M., Langs, G., Bezgin, G., Eickhoff, S. B., Castellanos, F. X., Petrides, M., Jefferies, E., & Smallwood, J. (2016). Situating the default-mode network along a principal gradient of macroscale cortical organization. Proc. Natl. Acad. Sci. U. S. A., 113, 12574–12579.

Miller, K. J., Sorensen, L. B., Ojemann, J. G., & den Nijs, M. (2009). Power-law scaling in the brain surface electric potential. PLoS Comput. Biol., 5, e1000609.

Monyer, H., Burnashev, N., Laurie, D. J., Sakmann, B., & Seeburg, P. H. (1994). Developmental and regional expression in the rat brain and functional properties of four NMDA receptors. Neuron, 12, 529–540.

Mukamel, R., Gelbard, H., Arieli, A., Hasson, U., Fried, I., & Malach, R. (2005). Coupling between neuronal firing, field potentials, and FMRI in human auditory cortex. Science, 309, 951–954.

Murray, J. D., Bernacchia, A., Freedman, D. J., Romo, R., Wallis, J. D., Cai, X., Padoa-Schioppa, C., Pasternak, T., Seo, H., Lee, D., & Wang, X.-J. (2014). A hierarchy of intrinsic timescales across primate cortex. Nat. Neurosci., 17, 1661–1663.

Nagasaka, Y., Shimoda, K., & Fujii, N. (2011). Multidimensional recording (MDR) and data sharing: an ecological open research and educational platform for neuroscience. PLoS One, 6, e22561.

Ogawa, T. & Komatsu, H. (2010). Differential temporal storage capacity in the baseline activity of neurons in macaque frontal eye field and area V4. J. Neurophysiol., 103, 2433–2445.

Ossmy, O., Moran, R., Pfeffer, T., Tsetsos, K., Usher, M., & Donner, T. H. (2013). The timescale of perceptual evidence integration can be adapted to the environment. Curr. Biol., 23, 981–986.

Pedregosa, F. (2011). Scikit-learn: Machine learning in python. J. Mach. Learn. Res., 12, 2825–2830.

Pegasiou, C. M., Zolnourian, A., Gomez-Nicola, D., Deinhardt, K., Nicoll, J. A. R., Ahmed, A. I., Vajramani, G., Grundy, P., Verhoog, M. B., Mansvelder, H. D., Perry, V. H., Bulters, D., & Vargas-Caballero, M. (2020). Age-Dependent changes in synaptic NMDA receptor composition in adult human cortical neurons. Cereb. Cortex.

Pinto, L., Rajan, K., DePasquale, B., Thiberge, S. Y., Tank, D. W., & Brody, C. D. (2019). Task-Dependent changes in the Large-Scale dynamics and necessity of cortical regions. Neuron, 104, 810–824.e9.

Podvalny, E., Noy, N., Harel, M., Bickel, S., Chechik, G., Schroeder, C. E., Mehta, A. D., Tsodyks, M., & Malach, R. (2015). A unifying principle underlying the extracellular field potential spectral responses in the human cortex. J. Neurophysiol., 114, 505–519.

Runyan, C. A., Piasini, E., Panzeri, S., & Harvey, C. D. (2017). Distinct timescales of population coding across cortex. Nature, 548, 92–96.

Sarafyazd, M. & Jazayeri, M. (2019). Hierarchical reasoning by neural circuits in the frontal cortex. Science, 364.

Savaskan, N. E., Bräuer, A. U., & Nitsch, R. (2004). Molecular cloning and expression regulation of PRG-3, a new member of the plasticity-related gene family. Eur. J. Neurosci., 19, 212–220.

Shine, J. M., Breakspear, M., Bell, P. T., Ehgoetz Martens, K., Shine, R., Koyejo, O., Sporns, O., & Poldrack, R. A. (2019). Human cognition involves the dynamic integration of neural activity and neuromodulatory systems. Nat. Neurosci., 22, 289–296.

Telenczuk, B., Dehghani, N., Le Van Quyen, M., Cash, S. S., Halgren, E., Hatsopoulos, N. G., & Destexhe, A. (2017). Local field potentials primarily reflect inhibitory neuron activity in human and monkey cortex. Sci. Rep., 7.

Tripathy, S. J., Toker, L., Li, B., Crichlow, C.-L., Tebaykin, D., Mancarci, B. O., & Pavlidis, P. (2017). Transcriptomic correlates of neuron electrophysiological diversity. PLoS Comput. Biol., 13, e1005814.

van Vugt, B., van Kerkoerle, T., Vartak, D., & Roelfsema, P. R. (2020). The contribution of AMPA and NMDA receptors to persistent firing in the dorsolateral prefrontal cortex in working memory. J. Neurosci., 40, 2458–2470.

Vértes, P. E., Rittman, T., Whitaker, K. J., Romero-Garcia, R., Váša, F., Kitzbichler, M. G., Wagstyl, K., Fonagy, P., Dolan, R. J., Jones, P. B., Goodyer, I. M., NSPN Consortium, & Bullmore, E. T. (2016). Gene transcription profiles associated with inter-modular hubs and connection distance in human functional magnetic resonance imaging networks. Philos. Trans. R. Soc. Lond. B Biol. Sci., 371.

Vezoli, J., Magrou, L., Wang, X.-J., Knoblauch, K., Vinck, M., & Kennedy, H. (2020). Cortical hierarchy and the dual counterstream architecture.

Virtanen, P., Gommers, R., Oliphant, T. E., Haberland, M., Reddy, T., Cournapeau, D., Burovski, E., Peterson, P., Weckesser, W., Bright, J., van der Walt, S. J., Brett, M., Wilson, J., Millman, K. J., Mayorov, N., Nelson, A. R. J., Jones, E., Kern, R., Larson, E., Carey, C. J., Polat, İ., Feng, Y., Moore, E. W., VanderPlas, J., Laxalde, D., Perktold, J., Cimrman, R., Henriksen, I., Quintero, E. A., Harris, C. R., Archibald, A. M., Ribeiro, A. H., Pedregosa, F., van Mulbregt, P., & SciPy 1.0 Contributors (2020). SciPy 1.0: fundamental algorithms for scientific computing in python. Nat. Methods, 17, 261–272.

Vos de Wael, R., Benkarim, O., Paquola, C., Lariviere, S., Royer, J., Tavakol, S., Xu, T., Hong, S.-J., Langs, G., Valk, S., Misic, B., Milham, M., Margulies, D., Smallwood, J., & Bernhardt, B. C. (2020). BrainSpace: a toolbox for the analysis of macroscale gradients in neuroimaging and connectomics datasets. Commun Biol, 3, 103.

Voytek, B., Kayser, A. S., Badre, D., Fegen, D., Chang, E. F., Crone, N. E., Parvizi, J., Knight, R. T., & D'Esposito, M. (2015a). Oscillatory dynamics coordinating human frontal networks in support of goal maintenance. Nat. Neurosci., 18, 1318–1324.

Voytek, B. & Knight, R. T. (2015). Dynamic network communication as a unifying neural basis for cognition, development, aging, and disease. Biol. Psychiatry, 77, 1089–1097.

Voytek, B., Kramer, M. A., Case, J., Lepage, K. Q., Tempesta, Z. R., Knight, R. T., & Gazzaley, A. (2015b). Age-Related changes in 1/f neural electrophysiological noise. J. Neurosci., 35, 13257–13265.

Vyas, S., Golub, M. D., Sussillo, D., & Shenoy, K. V. (2020). Computation through neural population dynamics. Annu. Rev. Neurosci., 43, 249–275.

Wagner, H. H. & Dray, S. (2015). Generating spatially constrained null models for irregularly spaced data using M oran spectral randomization methods. Methods Ecol. Evol., 6, 1169–1178.

Wang, M., Gamo, N. J., Yang, Y., Jin, L. E., Wang, X.-J., Laubach, M., Mazer, J. A., Lee, D., & Arnsten, A. F. T. (2011). Neuronal basis of age-related working memory decline. Nature, 476, 210–213.

Wang, M., Yang, Y., Wang, C.-J., Gamo, N. J., Jin, L. E., Mazer, J. A., Morrison, J. H., Wang, X.-J., & Arnsten, A. F. T. (2013). NMDA receptors subserve persistent neuronal firing during working memory in dorsolateral prefrontal cortex. Neuron, 77, 736–749.

Wang, X. J. (1999). Synaptic basis of cortical persistent activity: the importance of NMDA receptors to working memory. J. Neurosci., 19, 9587–9603.

Wang, X.-J. (2002). Probabilistic decision making by slow reverberation in cortical circuits. Neuron, 36, 955–968.

Wang, X.-J. (2008). Decision making in recurrent neuronal circuits. Neuron, 60, 215–234.

Wang, X.-J. (2020). Macroscopic gradients of synaptic excitation and inhibition in the neocortex. Nat. Rev. Neurosci.

Wasmuht, D. F., Spaak, E., Buschman, T. J., Miller, E. K., & Stokes, M. G. (2018). Intrinsic neuronal dynamics predict distinct functional roles during working memory. Nat. Commun., 9, 3499.

Watanabe, T., Rees, G., & Masuda, N. (2019). Atypical intrinsic neural timescale in autism. Elife, 8.

Whitaker, K. J., Vértes, P. E., Romero-Garcia, R., Váša, F., Moutoussis, M., Prabhu, G., Weiskopf, N., Callaghan, M. F., Wagstyl, K., Rittman, T., Tait, R., Ooi, C., Suckling, J., Inkster, B., Fonagy, P., Dolan, R. J., Jones, P. B., Goodyer, I. M., NSPN Consortium, & Bullmore, E. T. (2016). Adolescence is associated with genomically patterned consolidation of the hubs of the human brain connectome. Proc. Natl. Acad. Sci. U. S. A., 113, 9105–9110.

Wimmer, K., Nykamp, D. Q., Constantinidis, C., & Compte, A. (2014). Bump attractor dynamics in prefrontal cortex explains behavioral precision in spatial working memory. Nat. Neurosci., 17, 431–439.

Yanagawa, T., Chao, Z. C., Hasegawa, N., & Fujii, N. (2013). Large-scale information flow in conscious and unconscious states: an ECoG study in monkeys. PLoS One, 8, e80845.

Zeraati, R., Engel, T. A., & Levina, A. (2020). Estimation of autocorrelation timescales with approximate bayesian computations.

Zylberberg, J. & Strowbridge, B. W. (2017). Mechanisms of persistent activity in cortical circuits: Possible neural substrates for working memory. Annu. Rev. Neurosci., 40, 603–627.

Chapter 4

Conclusion

This dissertation combines computational frameworks for simulating brain signals and analysis of data across species and modalities to decipher large-scale brain dynamics, specifically rhythmic and asynchronous (or aperiodic) neural activity recorded in ECoG and LFP, in terms of their underlying spiking, synaptic, and other physiological contributions. By doing so, these signal modalities, which are routinely mined for neural correlates of cognition, can then be used to infer low-level and otherwise inaccessible biological variables to enable a mechanistic investigation of human cognition. As I have already built the case for in the introduction, animal cognition can often be used as a stand-in for shared subsets or prerequisites of the computations involved in human cognition, but not as a replacement. Therefore, it would be extremely beneficial for human cognitive and clinical neuroscience to link complex cognitive functions, as well as neurological and psychiatric disorders, to their underlying biological mechanisms, and this dissertation represents a preliminary effort towards that goal. I will conclude here by voicing a limitation of the data-driven approach shared by the included works, as well as how more sophisticated simulation and analysis frameworks can address the aforementioned limitation.

By and large, science is in the business of finding insightful co-variations between often high-dimensional measurements—which includes finding meaningful measurements in the first place—and explaining those covariations with simpler descriptions of the underlying latent processes. The first establishes correlation, the latter converges on mechanism. When considering data across scales or modalities, such as the cortex-wide variation of gene expression and neuronal timescale presented in Chapter 3, a common criticism is that "it's only a correlation". This is a valid criticism since, strictly speaking, the analyses presented only support the conclusion that there is a (linear) correlation between, for example, potassium ion channel gene expression and neuronal timescale. The data does not prove a definitive and causal relationship between the amount of potassium channels and the intrinsic timescale of a brain region, nor does it elucidate how exactly the former shapes the latter, though the implication is that more functional potassium ion channels in the cell membrane shortens the time constants of the corresponding ionic currents. The same can be said for the suggestive relationship between cellular variables and network dynamics in the organoids throughout their maturation, presented in Chapter 1. As such, although the present data-driven analysis framework is valuable for identifying potential relationships between cellular variables and large-scale dynamics in the human brain, it does not dissect the step-by-step process behind their interaction, which requires further detailed perturbation experiments to introduce controlled variations.

However, nevermind the fact that such perturbation experiments cannot be performed in the human brain, even if one was to perform these experiments in-vitro or in animal models, the sheer number of variables concerned and the nonlinearity of their interactions in such a complex system renders these efforts all but futile. This is because perturbation experiments typically hinge on the assumption of "all else being equal", meaning that we can identify the mechanistic contribution of one variable at a time while all other relevant variables can be controlled and held constant. But this is rarely a safe assumption in the biological brain full of natural variations and feedback interactions across scales, and the problem is further exacerbated by the brain's total disregard of the linearity principle. Thus, it's difficult to say a priori which (combinations of) relationships will linearly generalize and within what range of values, so it would require an incredibly large sample size and the ability to simultaneously measure all variables of interest in order to have some confidence in the relationships we discover.

Is the search for mechanistic principles for how biology gives rise to human cognition hopeless then? I don't believe so. Instead of performing controlled in-vivo experiments in thousands or millions of mice, we can perform these experiments in-silico using computational models of neural circuits, in which one can hold any and all variables constant. The model presented in Chapter 2 is a simple example of this: artificial manipulation of synaptic excitation or inhibition while holding the other constant is difficult to do in-vivo, but can be easily achieved to measure the hypothetical effect on the exponent of simulated power spectra in the model. As stated in the Discussion section of Chapter 2, this model is clearly limited in that it ignores many other variables that are important for the frequency characteristics of field potentials, such as recurrent interactions between populations and other types of synaptic currents. However, the idea remains. Moving forward, I believe that we need to build more sophisticated mechanistic models of neural circuits that are consistent with the underlying biology, reproduce the observed brain dynamics, and perform the hypothesized computations—ideally, through an automated framework. Within this framework, analysis of real brain data serves a different purpose: instead of looking for descriptive features that correlate with or differentiate between cognitive and disease states, brain data is used to constrain the space of possible mechanistic models, forming a cyclic process of model design (synthesis) and discovery (analysis). In the context of large-scale simulations, this process is called data assimilation or simulation-based inference, which is now routinely applied in fields employing high-dimensional model systems, such as weather prediction. Inversion (or inference) of such models with large parameter spaces—as would be the case for models of neural circuits—presents significant technical difficulties, but I believe that it would ultimately prove to be a productive path forward, thereby combining computational modeling with analysis of "big data" in neuroscience to link neurobiology and human cognition.